UNIVERSITÀ
DI TORINO

Università degli Studi di Torino

PhD Programme in Biological Sciences
and Applied Biotechnologies

Epidermal stem cells acquire the memory of an injury that predisposes to skin cancer

Tutor:
Giacomo Donati

Candidate:
Chiara Levra Levron

XXXVI° Cycle: 2020 /2023

The following chapters are adapted from a peer-reviewed article:

Chiara Levra Levron[1,2,*], Mika Watanabe[1,2,*], Valentina Proserpio[1,2,3,*], Gabriele Piacenti[1,2,], Andrea Lauria[1,2,3], Stefan Kaltenbach[4], Annalaura Tamburrini[1,2,3], Takuma Nohara[5], Francesca Anselmi[1,2], Carlotta Duval[1,2], Luca Elettrico[1,2], Daniela Donna[1,2], Laura Conti[2,6], Denis Baev[3], Ken Natsuga[5], Tzachi Hagai[4], Salvatore Oliviero[1,2,3], Giacomo Donati[1,2, $], *Tissue memory relies on stem cell priming in distal undamaged areas.* **Nat Cell Biol** 25, 740–753 (2023). https://doi.org/10.1038/s41556-023-01120-0.

[1] Department of Life sciences and Systems Biology, University of Turin, Torino, Italy

[2] Molecular Biotechnology Center "Guido Tarone", University of Turin, Torino, Italy

[3] Italian Institute for Genomic Medicine, Candiolo (TO), Italy

[4] Shmunis School of Biomedicine and Cancer Research, George S Wise Faculty of Life Sciences, Tel Aviv University, Tel Aviv 69978, Israel

[5] Department of Dermatology, Faculty of Medicine and Graduate School of Medicine, Hokkaido University, Sapporo, Japan

[6] Department of Molecular Biotechnology and Health Sciences, University of Turin, Turin, Italy

* Co-first authorship

[$] Last authorship

TABLE OF CONTENTS

Abstract i
Acknowledgments ii
List of Figures .....iii-v

CHAPTER 1 Page 1-12

Introduction 1
1.1 The skin 1-2
1.2 The interfollicular epidermis and its appendages 2-5
1.3 The epidermal lineages 5-7
1.4 Epidermal cells' dynamics during wound healing.....7-9
1.5 Epidermal cells' adaptation to tissue injuries 9-10
1.6 The epigenetic field cancerization 11-12

CHAPTER 2 Page 13-22

RESULTS I, *Injury trains epidermal stem cells with a wide spatial range* 13
2.1 Lrig1 progeny distally located from the damage adapts its behaviour to the injury..13-19
2.2 Distal memory Lrig1 GL cells display enhanced migratory abilities 19-22

CHAPTER 3 Page 23-33

RESULTS II, *Transcriptional profiling of memory cells identifies priming as the opted adaptive mechanism* 23
3.1 Priming occurs in Lrig1 stem cell progeny from distal hair follicles 23-26
3.2 Transcriptional basis of Lrig1 GL cells' priming 26-31
3.3 Lineage specificity of epidermal cells' priming 31-33

CHAPTER 4 Page 34-41

RESULTS III, *Wide epigenetic rearrangements support the transcriptional priming of memory cells* 34-41

4.1 Chromatin profiling of memory cells 34-35

4.2 Long-range priming relies on the downregulation of H2AK119ub repressive mark ..36-41

CHAPTER 5 Page 42-50

RESULTS IV, *Injury-directed priming predisposes to tumorigenesis* 42-50

5.1 Memory is long-term maintained 42-44

5.2 Epithelial priming promotes tumour onset with a spatial gradient 44-50

CHAPTER 6 Page 51-54

Discussion.....51-50

6.1 Trained memory versus priming in epithelial cells 51

6.2 Wide distribution of wound priming in undamaged areas 51-52

6.3 Transcriptional de-repression and cell state of wound-primed progenitors 52-53

6.4 Long-term priming lays the foundation for field cancerization 53-54

CHAPTER 7 Page 55-33

Material and Methods 55-67

7.1 Mouse procedures 55
7.1.1 Mouse strains 55
7.1.2 Lineage tracing of hair follicle lineages 55
7.1.3 Full-thickness skin wound 55

7.2 Immunostaining and image processing.....55-58
7.2.1 Epidermal and dermal whole-mount 55-56
7.2.2 MitoTracker staining 56
7.2.3 Immunostaining of skin sections 56-57
7.2.4 Immunostaining of ex vivo cell cultures 57
7.2.5 Images acquisition 57-58
7.2.6 Images quantification using ImageJ 58

7.3 *In vitro* and *ex vivo* assays 58-59

7.3.1 Isolation and in vitro culture of Lrig1 GL cells 58
7.3.2 In vitro time lapse migration assay 59
7.3.3 Ex vivo migration assay 59

7.4 Flow cytometry 59-60
7.4.1 Fluorescence-activated cell sorting (FACS) 59-60
7.4.2 Glut1 quantification 60
7.4.3 Quantification of immune infiltrate 60

7.5 Screening of epigenetic drugs 61

7.6 *In vivo* tumorigenesis 61-62

7.6.1 UV irradiation and tumorigenesis protocol 61-62
7.6.2 Tumour analysis 62

7.7 Human squamous cell carcinoma samples (SCC) 62

7.8 Transcriptomics 62-65

7.8.1 Mini-bulk RNA-seq and analysis 62-63
7.8.2 scRNA-seq and analysis 63-64
7.8.3 Differential expression analysis and feature extraction 64
7.8.4 Seurat integration 65
7.8.5 Pseudotime analysis 65
7.8.6 GO enrichment analysis 65
7.8.7 GSEA analysis 65

7.9 ATAC-seq and analysis 66

7.10 Quantification and statistical analysis 67

7.11 Data availability 67

CHAPTER 9 Page 68-74

Bibliography 68-75

CHAPTER 10 Page 76

Publications 76

Abstract

It is believed epithelial cells that have participated in a wound repair elicit a more efficient but locally restricted response to future injuries. However, here we show that the cell adaptation resulting from a localised tissue damage has a wide spatial impact at a scale previously unrecognised. We demonstrate that as a consequence of a first healed injury a specific epithelial stem cell population gives rise to long term wound-memory progenitors residing distal to the site of injury. Notably, these wound-distal progenitors, although not directly engaged in the initial wound healing, undergo pre-activation through a *priming* mechanism. This adaptive process diverges from the classical features of *trained immunity* previously shown to be opted by other epithelial stem cells. Our newly identified wound-distal memory cells display an intrinsic pre-activated state, persisting at both chromatin and transcriptional levels. This pre-activation confers an augmented capacity for wound repair, a phenomenon that can be partially replicated through an epigenetic perturbation even in the absence of an injury. Importantly, the deleterious consequences of wound repair, such as exacerbated tumorigenesis, occur within these primed cells and follow their spatial distribution. Overall, our study elucidates that the sub-organ scale adaptation to injury relies on spatially organised and memory-dedicated progenitors characterised by a chromatin-actionable cellular state. This state establishes an epigenetic field cancerization, thereby predisposing the tissue to the onset of tumorigenesis.

Acknowledgements

I would like to express my deepest gratitude to:

My mentor, Professor *Giacomo Donati*, for the opportunity to join his research group, the support and the guidance over these three years of doctoral research.

Special thanks to my colleagues and all the past and present members of the Donati lab: *Mika Watanabe*, *Gabriele Piacenti*, *Carlotta Duval*, *Luca Elettrico*, *Alessandro Croce*, *Dilay Yilmaz*, *Osamu Ansai* and *Camilla Mallardi* for their constant support, the advises, the stimulating discussions and for creating a funny, pleasant, and intellectually stimulating environment.

Professor *Valentina Proserpio*, for the constructive discussion and for introducing me to the single cell world, and all the members of her research team.

Professor *Salvatore Oliviero* and all the members of his research group, in particular: *Andrea Lauria*, *Annalaura Tamburrini* and *Francesca Anselmi* that contributed to this work.

Professor *Enzo Calautti*, that introduced me to the world of the scientific research.

Finally, I would like to acknowledge all the collaborators, my family, and my friends.

List of Figures

CHAPTER 1

Figure 1.1. The architecture of mammalian skin 1

Figure 1.2. The epidermis, the pilosebaceous unit and the sweat gland 3

Figure 1.3. The hair follicle cycle 5

Figure 1.4. The interfollicular epidermis and the pilosebaceous unit are heterogenous, hosting multiple cellular lineages 6

Figure 1.5. Sequential phases of wound repair 7

Figure 1.6. The interfollicular epidermal cells and the hair follicle cells repair the wound 8

Figure 1.7. Lineage-specific contribution to wound healing 9

Figure 1.8. Epidermal stem cells establish a memory that resembles trained immunity 10

Figure 1.9. The field cancerization theory 11-12

CHAPTER 2

2.1 Lrig1 progeny distally located from the damage adapts its behaviour to the injury

.....13-18

Figure 2.1. The two consecutive injury model 14-15

Figure 2.2. The second injury repairs faster than the first one 15

Figure 2.3. Wound memory in hair follicle lineages and its spatial extension 16-17

Figure 2.4. Memory is also established distally from the injury 18

2.2 Distal memory Lrig1 GL cells display enhanced migratory abilities

.....19-22

Figure 3.1. Lrig1 progeny displays enhanced fitness after wound experience 20-21

Figure 3.2. Transcriptome analysis of Lrig1 GL cells suggests a new primed subpopulation arising after wound resolution 21-22

CHAPTER 3

3.1 Priming occurs in Lrig1 stem cell progeny from distal hair follicles 23-26

Figure 4.1. Single cell analysis assigns known epidermal niches to cell clusters 23-24

Figure 4.2. Analysis of the pseudotime trajectories 24-25

Figure 4.3. Deep analysis of the *Transition cluster* 26

3.2 Transcriptional basis of Lrig1 GL cells' priming 26-31

Figure 5.1. Transcriptional characterization of priming cell state 27-28

Figure 5.2. Cell priming relies on enhanced metabolism 29-30

Figure 5.3. Spatially resolved single cell RNA-seq confirms distal priming 30-31

3.3 Lineage specificity of epidermal cells' priming 31-33

Figure 6. Comparison between single cell profiling of Lgr5 and Lrig1 lineages 32-33

CHAPTER 4

4.1 Chromatin profiling of memory cells 34-35

Figure 7. Chromatin remodelling in distal priming 35

4.2 Long-range priming relies on the downregulation of H2AK119ub repressive mark

.....36-41

Figure 8.1. The reduction of H2AK119Ub is physiological after wound in distal memory areas 36-37

Figure 8.2. PRT4165 treatment transcriptionally mimics memory in Lrig1 epidermal lineage 38

Figure 8.3. PRC1 inhibition induces the chromatin state of wound priming 39

Figure 8.4. PRT4165 treatment reproduces memory-associated phenotypes specifically in Lrig1 GL cells ..40-41

CHAPTER 5

5.1 Memory is long-term maintained 42-44

Figure 9.1. Priming-associated cell state is long-term maintained in infundibular Lrig1 GL progeny 42-43

Figure 9.2 Transcriptional priming is preserved in ageing 43-44

5.2 Epithelial priming promotes tumour onset with a spatial gradient 44-50

Figure 10.1. Healed wound in tail skin predisposes to pre-tumoral lesions 45-46

Figure 10.2. Wound priming initiates field cancerization 47

Figure 10.3. Pre-injured back skin is prone to SCCs onset 48-49

Figure 10.4. Glut1 overexpression and H2AK119Ub reduction are characteristics of wound-derived SCCs in humans 50

CHAPTER 1

Introduction

1.1 The skin

With 15% of the adult body weight, the skin is the biggest organ in the body. It carries out a multitude of essential functions, such as preventing the body water loss, aiding in thermoregulation, and protecting against external physical, chemical, and microbial insults. The mammalian skin is composed of three layers: the *epidermis*, the *dermis*, and *hypodermis* (**Figure 1.1**)[1].

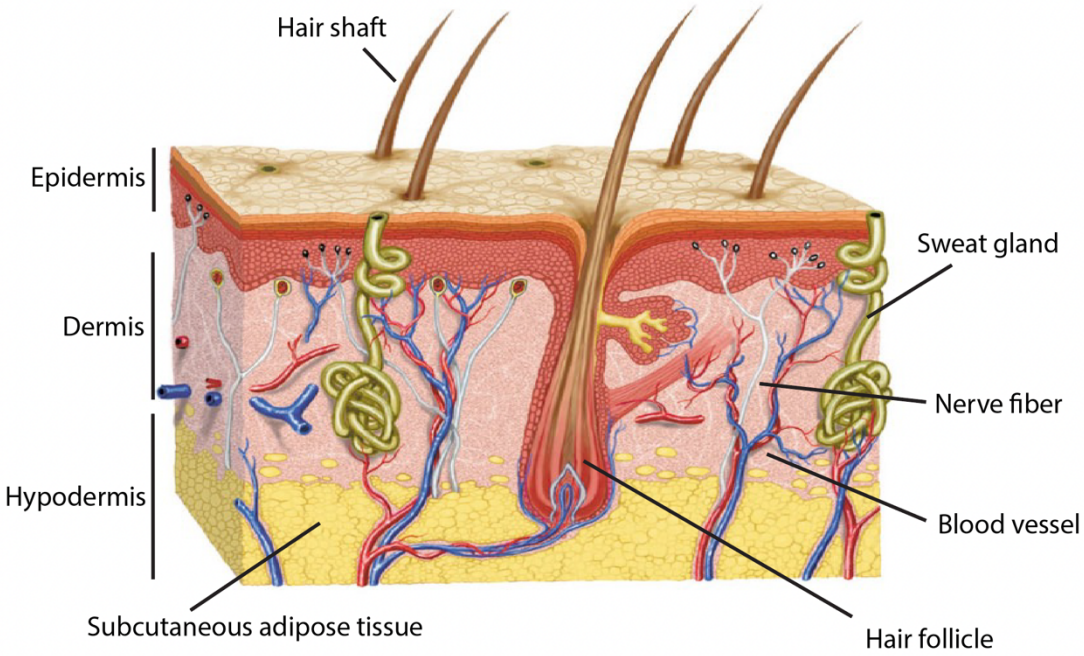

Figure 1.1. The architecture of mammalian skin. The skin comprises three primary layers: the outer epidermis and the underlying dermis and hypodermis. The epidermis is stratified, with the outermost layer composed of periodically shedding dead cells, gradually replaced by cells originating from the basal layer. The dermis links the epidermis to the hypodermis, supplying strength and elasticity through collagen and elastin fibres. Situated beneath the dermis, the hypodermis functions as connective tissue, linking the dermis to underlying structures, and serves as a repository for adipose tissue, contributing to fat storage and protection[1].

The hypodermis, or subcutaneous fascia, constitutes the inner layer of subcutaneous white adipose tissue and serves metabolic and endocrine functions, with a variable thickness depending on the

geographic location on the anatomy of the body. The lobules comprising fat cells, or lipocytes, are delineated by a fibrous septa composed of collagen and large blood and lymphatic vessels[1].

The other two layers, the dermis and the epidermis, are separated by a thin, dense layer of extracellular matrix (ECM), known as the basement membrane[2].

The dermis lies immediately above the hypodermis, and it provides pliability, elasticity, and tensile strength to skin, safeguarding the body from mechanical injury, supporting thermal regulation, and hosting sensory receptors. It is composed by a complex network of fibrous, filamentous, and amorphous connective tissue, in which many cell types are intersperse; fibroblasts, macrophages, and mast cells, as well as sensory neurons and vessels cells are the main host of dermis. Additionally, it accommodates two epidermal appendages: the pilosebaceous unit, composed by the hair follicle and the sebaceous gland, and the sweat gland[1].

The outermost layer of the skin is the epidermis, a stratified, squamous epithelium layer composed of keratinocytes, its most abundant cell component, and other cell populations, such as melanocytes, Langerhans dendritic cells, and Merkel cells that represent type I mechanoreceptors[1].

1.2 The interfollicular epidermis and its appendages

The epidermis, or interfollicular epidermis (IFE), is divided into four layers according to keratinocyte morphology and relative position. The basal layer (stratum germinativum) is made up of column-shaped progenitor cells that adhere to one another through desmosomal junctions and directly lay on the basement membrane. These mitotically active cells stratify to give rise to differentiated cells of the spinous, granular and cornified layers; the migration of a basal cell from the basal layer to the cornified layer in humans takes at least 14 days, and the transit toward the more superficial cornified layer requires another 14 days. Although epidermal stem cells (SCs) are slow cycling cells, several conditions, such as wounding, can accelerate their division rate to enable the repair. The squamous layer (stratum spinosum) is composed of a variety of cells that differ in shape, structure, and subcellular properties depending on their relative location. Indeed, suprabasal spinous cells are polyhedral in shape and have a rounded nucleus, while the cells of the upper spinous layers are generally larger and flatter, and contain lamellar granules[1].

The granular layer (stratum granulosum) is the outermost layer of the epidermis housing living cells, and consists of flattened cells containing keratohyalin granules in their cytoplasm. These cells play a crucial role in the ongoing synthesis and modification of proteins essential for the process of keratinization. Finally, the cornified or horny cell layer (stratum corneum) provides a mechanical barrier for the underlying epidermis while preventing water loss and invasion by foreign substances[3] (**Figure 1.2**).

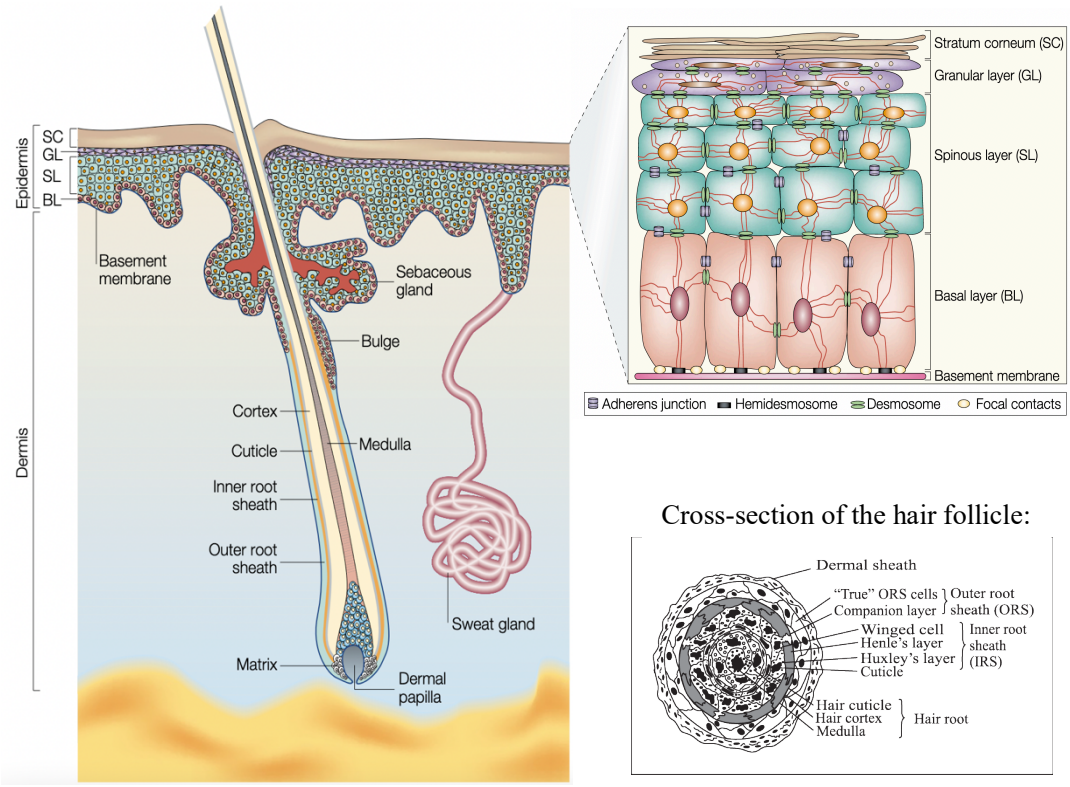

Figure 1.2. The epidermis, the pilosebaceous unit and the sweat gland. The epidermis, separated from the dermis through the basement membrane, is a stratified squamous epithelium with multiple cell layers. The basal layer (BL), located on the basement membrane, comprises proliferating transit-amplifying cells. This basal layer undergoes stratification, giving rise to the spinous layer (SL), granular layer (GL), and the stratum corneum (SC). The outer root sheath is contiguous with the basal epidermal layer. The hair bulb, formed by proliferating matrix cells, is located at the follicle's base. Matrix cells, in turn, terminally differentiate to generate diverse hair follicle cell types. The bulge, part of the outer root sheath, houses epidermal stem cells. The dermal component of the hair follicle is the dermal papilla, specialised mesenchymal cells that surround hair matrix cells[2]. A cross-section of the HF depicts the seven inner layers that are generated by matrix progenitor cells.

The mammalian epidermis produces an array of appendages that includes the sweat gland, the nails, and and the pilosebaceous unit (PSU), composed by the hair follicle (HF) and the sebaceous gland (SG) and the arrector pili muscle. All these appendages originate as downgrowths from the epidermis during development[1,4].

Separated from the PSU, each sweat gland is deeply coiled in the dermis and has its own duct from which the sweat protrudes toward the surface. Its function is to cool the body and the production by each gland is adjusted through sensory nerve stimuli[4].

In the SGs, the sebocyte progenitors are located at the junction between the HF and the gland and undergo differentiation while following an inward movement. Upon terminal differentiation, these cells ultimately degenerate, releasing sebum into the lumen. The expelled sebum exits through the same orifice as the hair, serving as an oily lubricant for the skin surface and hairs[4].

The HF comprises several concentric structures. The medulla, the cortex and the cuticle form the hair shaft, which is enveloped by two epithelial sheaths, known as the inner root sheath (IRS) and the outer root sheath (ORS), that is contiguous with the basement membrane. The matrix, also called hair germ, is located at the proximal end of the HF, the bulge, and forms the germinal centre for HF growth, surrounded by the mesenchymal cells of the dermal papilla (**Figure 1.2**)[5,6].

Indeed, unlike the hair itself, which is composed of dead cells, HFs undergo a process of regeneration that controls the production of the hair shaft[7].

The hair bulge supports successive regenerative cycling, a process finely tuned by the interplay between dermal cells and epidermal keratinocytes in the lower PSU. Three distinct phases characterise the HF cycle: anagen, catagen and telogen. Depending on geographical body location, in mice, the initial phase of PSU morphogenesis ceases at postnatal day (P) 14-18[6]. At this point, the hair cycling is initiated by the catagen phase, in which the bottom of the hair follicle undergoes rapid apoptosis. Here, the proximal end of the HF involutes and the DP returns in close proximity to the follicle bulge. After a short resting phase of 3-4 days, named the telogen, the hair growth restarts. Upon anagen phase, SCs resident in the bulge proliferate to generate transit amplifying cells that then differentiate to form the new hair shaft, as anagen progresses (**Figure 1.3**)[7]. In mice, this first regenerative cycle is synchronised, and it ends, after the anagen, with another catagen phase and a long telogen phase at ~P42-49, which lasts 2-3 weeks. Subsequent hair cycles are asynchronous. and continue throughout life[6].

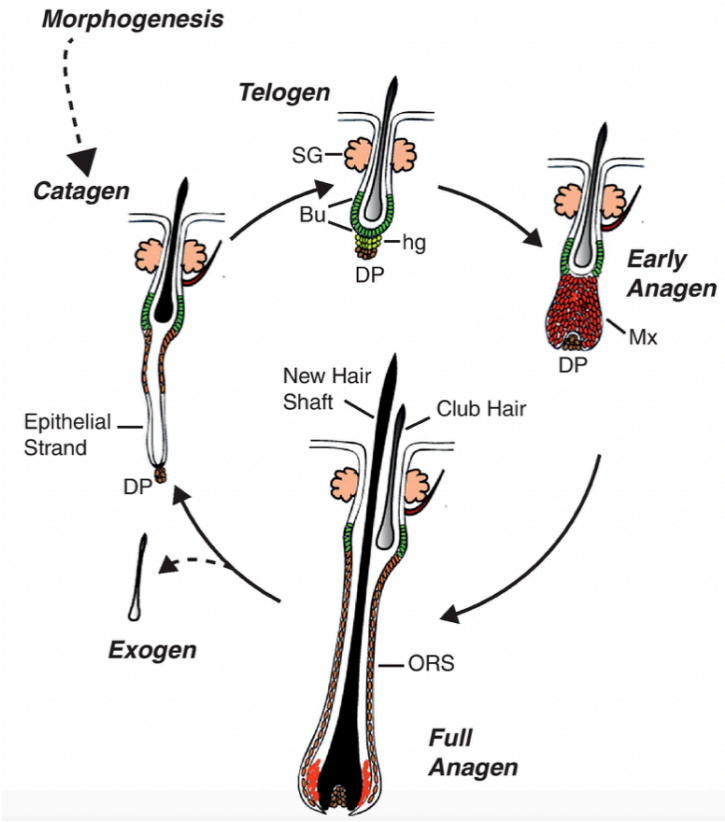

Figure 1.3. The hair follicle cycle. The illustration sums up the HF cycle clock, consisting of anagen, catagen and telogen. Bulge (Bu); Matrix (Mx); hair germ (hg)[7].

1.3 The epidermal lineages

The primary component of the epidermis is the IFE, while the PSU is a significant structure closely associated with it. These two units cooperate to maintain the homeostatic integrity of the epidermis itself, through a continuous turnover ensured by SCs[4,8]. In recent years, the use of lineage tracing, that involves the labelling of cells to track their subsequent behaviour and fate, combined with high resolution 3D imaging, has transformed our understanding of epithelial SCs, pointing out the existence of several epidermal lineages of SCs, that differentiate into distinct cell populations[9]. Indeed, we now know that epithelia, such as epidermis, are not obligatorily maintained by a single, homogeneous stem cell population of SCs, stem cell compartmentalization. Rather, several SCs pools exist, characterised by differences in the molecular markers where they express and their context-dependent functions[8]. Importantly, these different lineages are not randomly interspersed within the

tissue, but accurately compartmentalised in specific specialised microenvironments, named *niches*, that comprises specific ECM, growth factors, cell–cell interactions, and other signals[8–10]. In this context, the PSU is compartmentalised in several spatial and functional units, that are maintained autonomously by their own SC's pool (**Figure 1.4**).

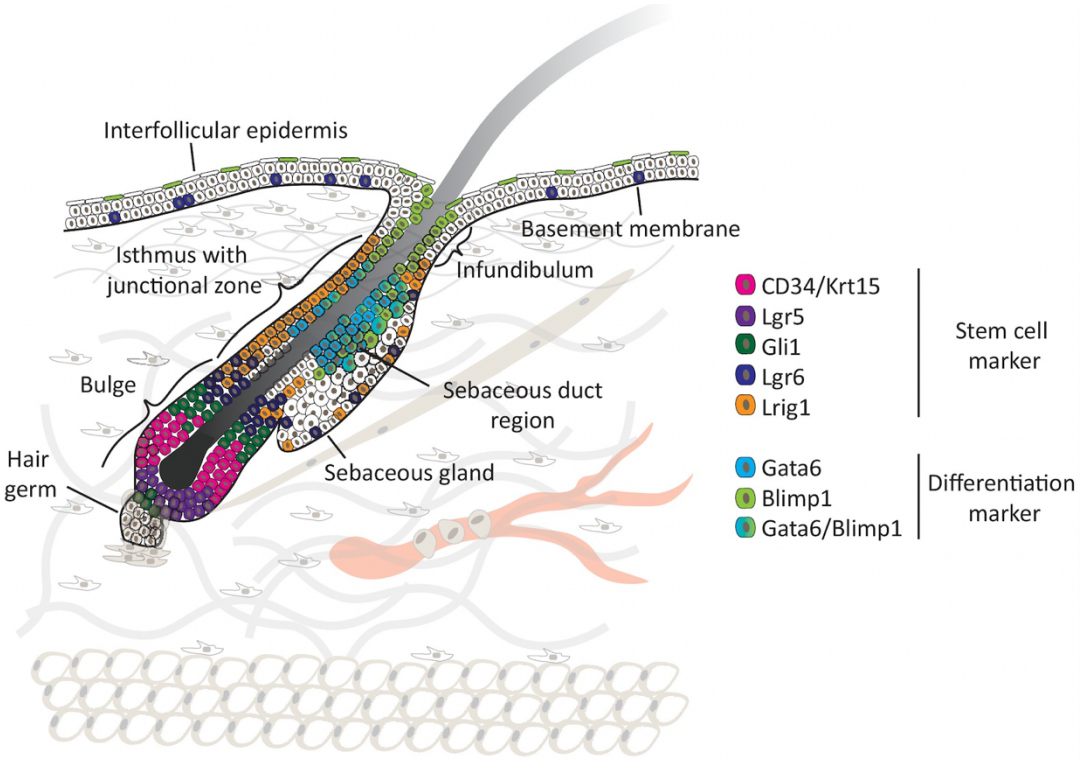

Figure 1.4. The interfollicular epidermis and the pilosebaceous unit are heterogenous, hosting multiple cellular lineages. Schematic representation of the SCs and other differentiating cell populations in the IFE and in the HF. Distinct molecular markers, indicated with different colours, map the spatial distribution of distinct SC and differentiated cell populations in the IFE and in all the HF compartments, bulge, isthmus, infundibulum and sebaceous gland[10].

The bulge represents the lower, permanent region of the HF. It harbours the SCs populations responsible for the HF growth cycle, that divide infrequently and is characterised by the expression of a variety of different markers including Lgr5, CD34 and Krt15. In particular, lineage tracing analysis revealed that the proportion of Lgr5$^+$ stem cells populating the bulge remained constant over time, maintaining the lower follicle through successive hair cycles[11]. The isthmus localises in the middle of the HF and is subdivided in lower isthmus, populated by Gli$^+$ and Lgr6$^+$ SCs, and upper isthmus, or junctional zone (JZ). The junctional zone (JZ) is the region that lies at the junction between the infundibulum (INFU), the bulge and the SG and hosts several Lrig1$^+$ and Plet1$^+$ SCs populations. Specifically, proliferating Lrig1-expressing SCs located in the JZ rapidly replenish the sebocytes,

sebaceous ducts and the infundibulum, without contributing to the IFE, suggesting that this compartment is maintained as an autonomous unit from the IFE[12,13]. Beyond SCs population, the HF accommodates several differentiating lineages. Among them, Gata6^{+} cells are a committed-to-differentiation population from the sebaceous ducts (**Figure 1.4**)[14,15].

1.4 Epidermal cells' dynamics during wound healing

Upon tissue damage, prompt skin repair is crucial to prevent excessive blood loss and infections. Wound healing involves sequential phases: haemostasis, inflammation, proliferation, and remodelling. Haemostasis, occurring immediately after tissue damage, forms a blood clot to halt bleeding, recruiting immune cells like neutrophils, macrophages, and lymphocytes to prevent infection and enhance the inflammatory response. The proliferation phase coordinates epidermal re-epithelialization and dermal repair. Finally, the remodelling phase eliminates unnecessary cells and induces extracellular matrix (ECM) remodelling (**Figure 1.5**)[16].

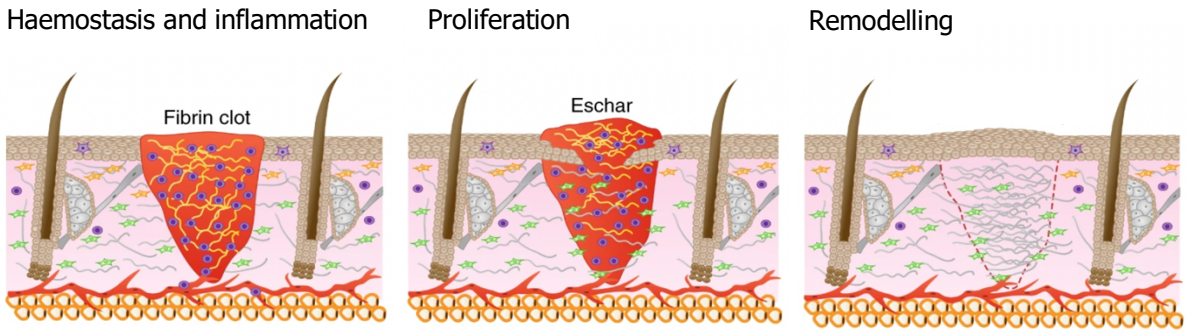

Figure 1.5. Sequential phases of wound repair. Haemostasis and inflammation start immediately after wounding. The fibrin clot prevents further blood loss and provides a scaffold for the migration of immune, dermal and epidermal cells. Follows the proliferation phase in which keratinocytes, fibroblasts and endothelial cells proliferate and migrate to the wound site. Finally, during the remodelling phase, the collagen in the dermis is remodelled and cells from earlier stages are removed[16].

When tissue damage occurs, the well-defined niche boundaries can be lost and each epithelial lineage resident nearby the injury acquires cell plasticity that allows it to migrate towards the wound site, thus contributing to the re-epithelialization (**Figure 1.6**)[13,14,16–21].

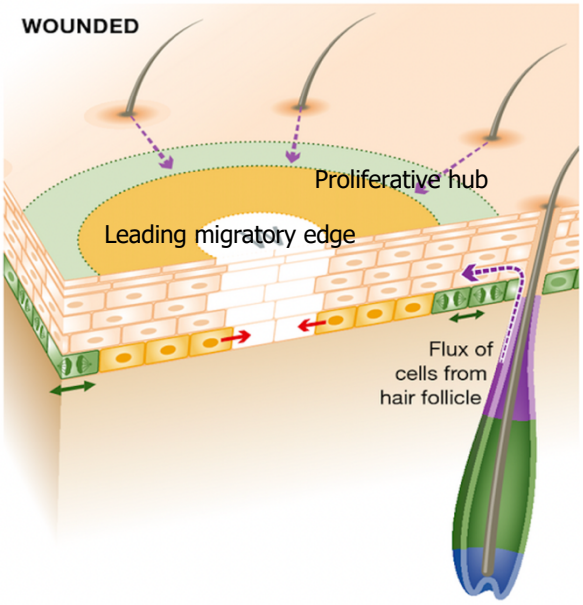

Figure 1.6. The interfollicular epidermal cells and the hair follicle cells repair the wound. Wound repair is supported by a flux of cells into the damaged area from all the compartments of the epidermis, including the HFs and the SGs (purple arrows) and, in tail skin, mobilisation of quiescent reserve cells in the epidermis. Two main zones can be distinguished based on repairing cell behaviour: (1) a leading migratory edge and (2) a proliferative hub. A mixed behaviour zone exists in between those two[21].

However, the way of exiting their niche, the overall contribution and the long-term occupancy of the wounded region are dependent on the lineage of origin of the repairing cells (**Figure 1.7**)[16]. While cell lineages of the bulge, the JZ, the infundibulum, and the IFE enter more as a cohesive cell population, sebaceous duct cells migrate to the wound site suprabasally as individual cells[10].

Clonal analysis of Krt14$^+$ IFE stem cells (IFESCs) and involucrin Inv$^+$-committed progenitor cells following injury of mouse tail skin showed that IFESCs are recruited to the newly formed epidermis, where they persist up to 35 days. By contrast, committed progenitors are initially recruited, but their progeny does not remain long-term in the IFE, since they are lost by differentiation.

Lineage tracing targeting bulge SCs (i.e Lgr5$^+$, Krt19$^+$ and Krt15$^+$ SCs) showed that lower HF cells rapidly migrate from the bulge to the wound, contributing to the repair. A small proportion of bulge stem cells that have been recruited to the IFE during healing can remain long term as IFESCs[20].

Similarly to bulge cells, Lrig1-expressing and Lgr6-expressing SCs from the upper isthmus and the infundibulum are mobilised following wounding and activated even more rapidly than bulge SCs. Although the proportion of Lrig1-derived cells located in the epidermis drops dramatically 3 weeks after an injury, remaining cells can persist up to 1 year thereafter[13]. Also differentiating cells participate in wound healing. Gata6-expressing sebaceous gland duct cells are recruited to the IFE and migrate suprabasally. A small proportion of them can then dedifferentiate and are re-established as IFESCs in the long term newly formed epidermis (**Figure 1.7**)[16].

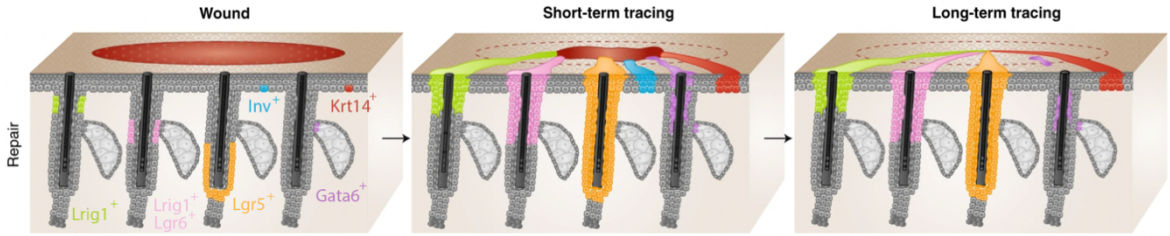

Figure 1.7. Lineage-specific contribution to wound healing. SCs and differentiating cells take part in wound healing, with different contribution and long-term persistence, based on the lineage of origin[16].

1.5 Epidermal cells' adaptation to tissue injuries

Innate immune cells opt exceptionally diverse adaptive programs that depend on the magnitude and duration of stimulation. Several such memories have been described, including differentiation, priming, tolerance and trained immunity[22]. Upon exposure to particular stimuli, innate immune cells mount a faster and greater response against a secondary challenge. This *trained immunity* occurs through the persistence of epigenetic alterations even after the stimulus ceasses[22]; during *priming*, instead, the initial stimulus induces a change in the functional state of the cells. In sharp contrast to trained immunity-like adaptation, the active gene transcription levels of primed cells do not return to naïve levels when the stimulus ceases[22]; additional adaptive mechanisms are *tolerance*, wherein the cell does not perform its functions following restimulation, and *differentiation*, that refers to the change of an immature cell into its mature counterpart, defined by a long-term change in the functional program of the cell[22]. In the last 5 years it emerged that epithelial cells adapt to a local stressful event, such as inflammation, infections or wounds, though the establishment of a chromatin memory to respond faster to an eventual similar challenge (**Figure 1.8a**)[23,24]. In particular, it has been demonstrated that, in parallel to the immune system, epithelial cells too exhibit *trained wound-memory* of an injury. After a wound event, these cells on the damaged area can establish chromatin memory that, following re-set of homeostasis, is kept transcriptionally dormant. However, this chromatin state allows a quick reactivation in the event of an eventual lesion[23–26].

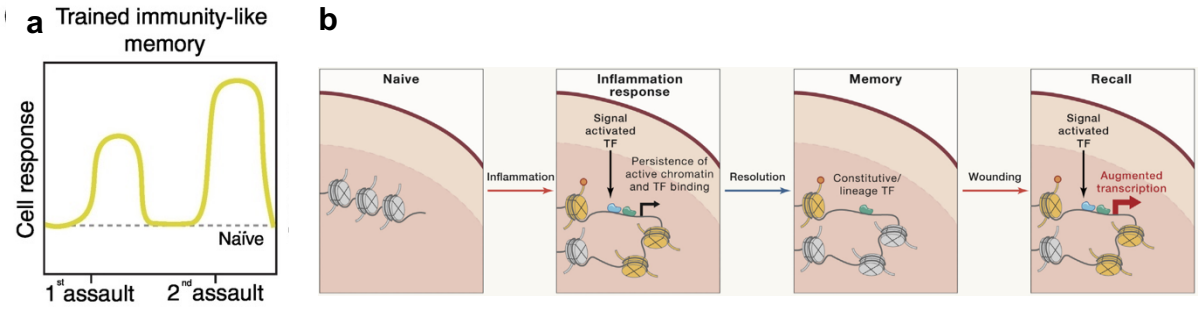

Figure 1.8. Epidermal stem cells establish a memory that resembles trained immunity. a, Trained immunity-like memory in epidermal cells confers to the cells enhanced repair ability in case of second injury[26]. **b**, During exposure to inflammation, epidermal cells experience the transient activity of signal-activated transcription factors such as STAT3. Following resolution of the inflammatory state, these homeostatic chromatin marks could then leave behind a durable epigenetic memory of inflammation, that exists through a poised accessible chromatin state of genes that are kept in a transcriptionally dormant state. These genes that maintain an easier accessibility to inflammation-activated transcription factors are rapidly reactivated in case of a re-challenge[23,27].

Trained immunity of immune cells is well characterised, both in terms of establishment and maintenance. Well-known and characterised epigenetic regulators of this memory are the acquisition of H3K27 acetylation on gene enhancers and the increase of H3K4 mono-methylation (H3K4me1) at the promoters of stimulated genes[28]. On the other hand, few molecular mechanisms controlling the memory of inflammatory events in epidermis have been revealed. As immune cells, epithelial cells establish a memory that is kept at epigenetic level, involving changes in chromatin accessibility and epigenetic pattern, such as the one described in **Figure 1.8b**[23,27]. In epidermis, an inflammatory assault induces histone modifications, such as H3K27ac and H3K4me1 deposition, as in the immune system[23]. The epigenetic changes are accompanied by the binding of a stimulus-activated transcription factor, for example STAT3, and a broad stress factor such as AP-1 (**Figure 1.8b**)[23]. Overall, epigenetic reprogramming confers higher plasticity to the memory cells, thus enhancing their ability to adapt to environmental stress and increasing their fitness in case of similar damages[27]. However, although the long-term accumulation of such memory-related modifications, that is skin has been observed until 180 days after wound[24], is beneficial in terms of tissue fitness, it may concurrently be maladaptive and lead to the development of pathological conditions such as cancer[29].

1.6 The epigenetic field cancerization

Cancer is an intricate and multifaceted disease involving both genomic and epigenomic factors. The epigenetic landscape of cells of origin and the pre-malignant niche significantly influences tumour initiation, progression, and phenotype[30–32]. Accumulated genetic, epigenetic, and tissue alterations in epithelial regions may enhance susceptibility to tumour growth, a phenomenon known as field cancerization, also referred as field change or field effect (**Figure 1.9**)[33]. First documented in a seminal study on oral carcinoma in 1953, field cancerization refers to the preconditioning of an epithelial area, making it more prone to carcinogenesis without apparent morphological abnormalities[34]. Over decades of cancer biology research, a deeper understanding has emerged regarding the cellular and molecular characteristics defining a cancerized field.

Epithelial tissues accumulate genetic, epigenetic and microenvironmental changes that positively select mutated clones, facilitating their expansion into potentially malignant cell patches[33,35]. While genetic lesions play a prominent role in forming cancerized fields, the significance of epigenetic field effects has gained increased attention. This influence is evident in various human cancers, including those affecting the vulva, head and neck, cervix, breast, colon, skin, bladder, lung, esophagus, stomach, and prostate[36]. Tumours associated with chronic inflammation often exhibit aberrations in DNA methylation levels as crucial molecular defects. Genome-wide DNA methylation alterations, for instance, have been implicated in urothelial and gastric carcinogenesis. Moreover, common epimutations in DNA repair genes have been found to be shared with related field defects[37,38]. However, the precise epigenetic molecular mechanisms guiding normal cells toward field cancerization remain largely unclear.

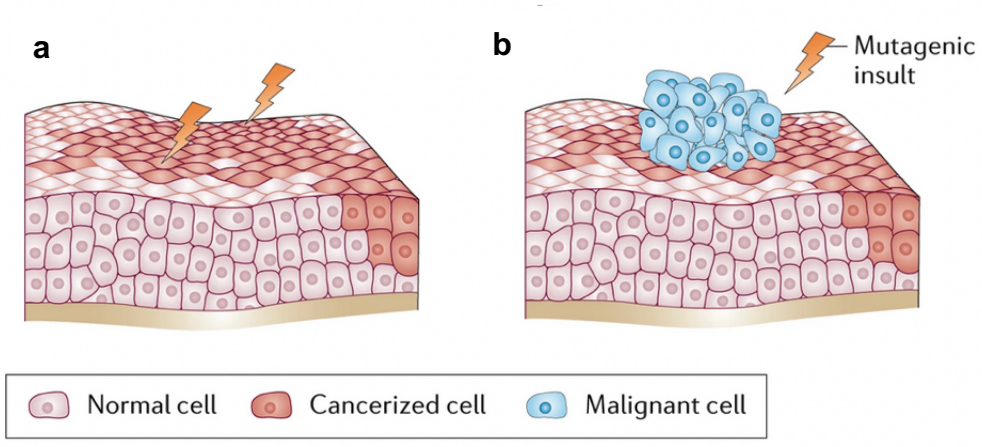

Figure 1.9. The field cancerization theory. a, A cancerized field may be initiated by cells following a multiplicity of different mutagenic insults. The insult may provide cells with advantageous phenotypes, for example as a consequence of UV exposure-associated DNA damage or due to an enabling microenvironment, such as the one induced by cigarette smoke. These initiated cells, which occur in varying numbers, will clonally expand to create a patch of cancer-primed cells. The cells within the cancerized field will look morphologically normal. **b**, The accumulation of additional mutations, due to following mutagenic insults, might start a tumour. This tumor began from a malignant cell that initially shared mutations and the concomitant altered phenotype with the surrounding cancerized tissue, but, within the field, the malignancy evolved because of additional mutations (and/or phenotypic change)[33].

CHAPTER 2

Injury trains epidermal stem cells with a wide spatial range

Results I

2.1 Lrig1 progeny distally located from the damage adapts its behaviour to the injury

HF cells are recruited during wound healing and the actual contribution to epidermal repair is specific for each cell lineage[16]. Recently, the existence of an epigenetic wound memory has been assessed for hair follicle stem cells (HFSCs)[25], but the precise lineage identity, the spatial distribution and the spectrum of adaptation programs acquired by the memory cells are still unknown (Figure 2.1a).

We focused on three well-characterised compartmentalised cell populations of the HF: Lrig1$^+$ SCs mainly localised in the HF junctional zone (JZ), and are involved in the maintenance of the sebocytes, sebaceous ducts and the infundibulum (INFU); Gata6$^+$ cells are are committed-to-differentiation and differentiated duct cells of the upper PSU; and Lgr5$^+$ SCs that are confined in the lower HF and are responsible for its cyclical growth[11,13,14].

To understand if their progenies elicited a wound-induced memory, we genetically labelled (GL) Lrig1$^+$, Lgr5$^+$, and Gata6$^+$ HF cells (Figure 2.1b,c) in adult mice, using a Cre-ER tamoxifen-driven driven lineage tracing system. We established a two consecutive injury model to assess memory in tail skin. Briefly, at time 0w, when cells are GL, we performed a first full thickness wound and we waited 8 weeks. At this time (8w pw1) a new homeostasis is settled in the wound site and in the wound distal epidermis (Figure 2.1e). Indeed, the differentiation rate of the cells, evaluated through FABP5 differentiation marker expression, the dermal fibrosis (defined by the number of nuclei in the dermis) and the amount of CD45$^+$ immune cells infiltrate are comparable to the homeostatic state,

0w (Figure 2.1f- h). Here, we induced a second identical and overlapping injury. The two actively healing time points were collected respectively 1 week after the first wound (1w pw1) and 1 weeks after the second overlapping wound (1w pw2).

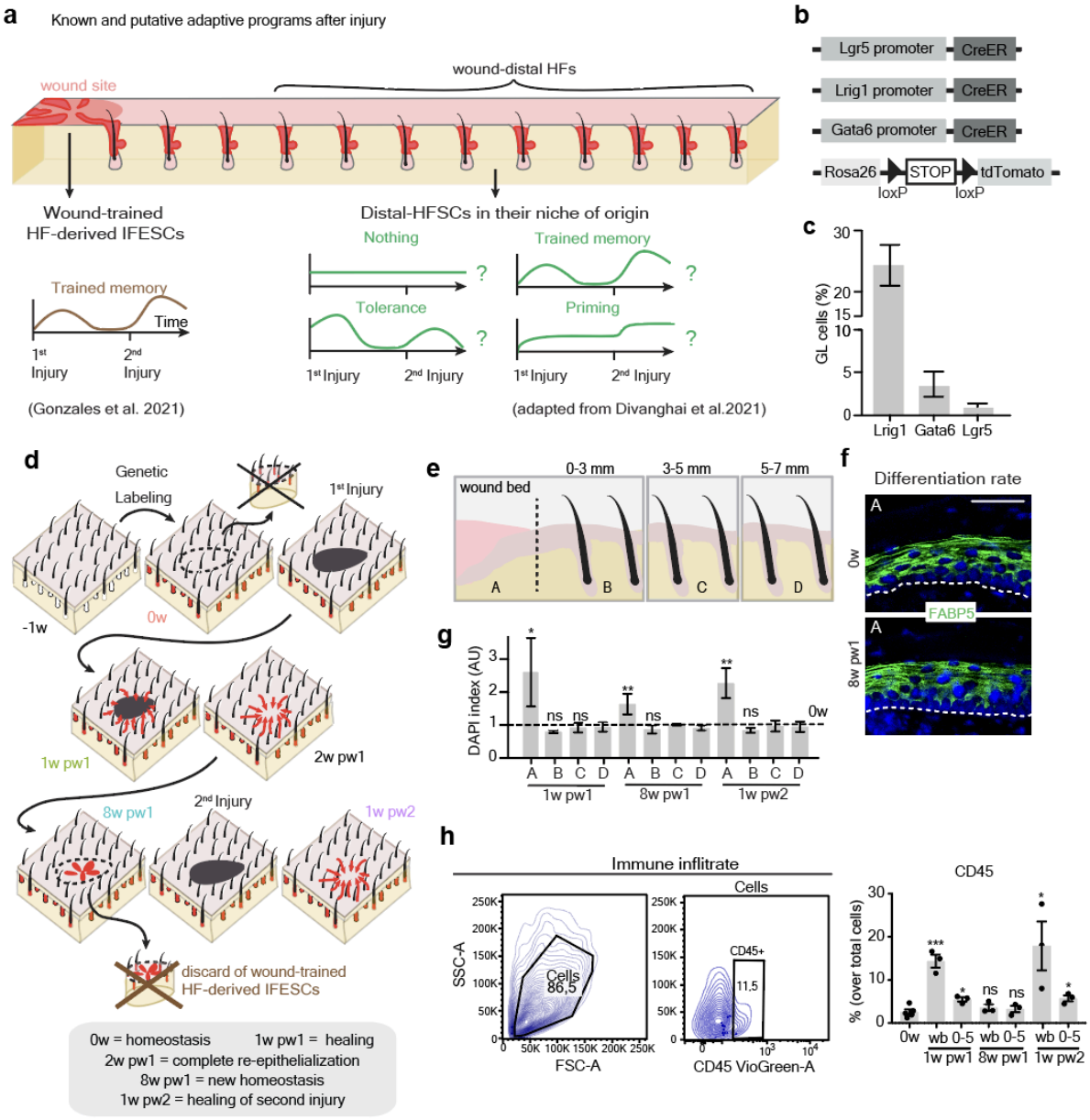

Figure 2.1. The two consecutive injury model. a, Schematic representation of the state of art and the study's objectives. On the left the repairing hair follicle (HFs) in proximity of the wound and the HF-derived newly formed epidermis, focus of Gonzales et al. study[25], are reported. On the right, cells in distal HFs and their adaptation program to wound will be the focus of this study. **b,** Scheme of murine genetic models: Cre-ER is expressed under Lrig1, Lgr5 or Gata6 promoters. Each strain is crossed with Rosa26-STOP-tdTomato mice to achieve genetic labelling upon Cre-ER activation by tamoxifen. **c**, Flow cytometry quantification of GL cells in the whole epidermis at 0w. n = 3-4 mice. **d**, Two consecutive skin injuries model: (-1w) genetical labelling (GL) through tamoxifen application; (0w) homeostasis; first injury; (1w pw1) healing phase, one week post first

wound; (2w pw1) complete re-epithelialization, two weeks post first wound; (8w pw1) new homeostasis, eight weeks post first wound, and second injury; (1w pw2) second healing phase, one week post second wound. **e**, Scheme of the sub-regions defined in injured skin. **f**, Immunolabeling of FABP5 differentiation marker at 0w and 8w pw1 (relative to zone A) showing that epidermal barrier is fully re-established at 8w pw1. Scale bar 50 µm. **g**, Dermal cell density as DAPI index (number of nuclei per mm^2). **h**, Gating strategy for the identification of $CD45^+$ immune infiltrate. Gates are set on negative controls (**left**). Flow cytometry quantification (%) of $CD45^+$ cells is shown for the wb and 0-5 regions at the indicated time points. n = 3-5 mice (**right**).

Here, in the absence of tissue contraction (Figure 2.2a,b), a main issue in the evaluation of back skin wound closure, the second injury heals faster than the first one (Figure 2.2c,d).

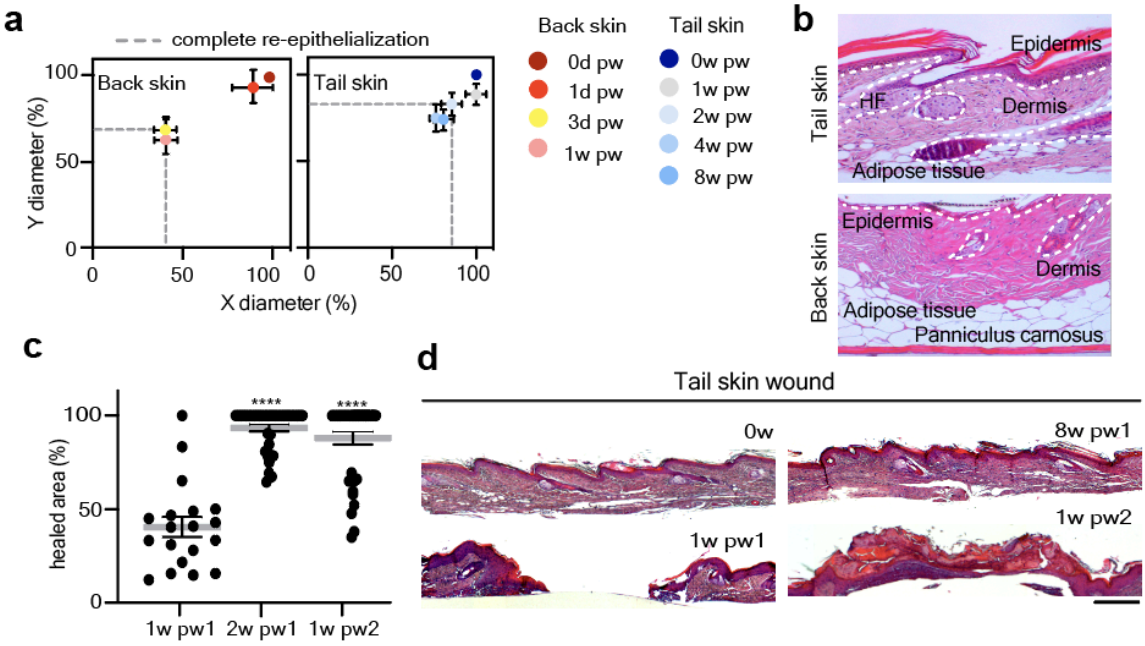

Figure 2.2. The second injury repairs faster than the first one. a, **b**, Tail skin wound model is selected to reduce the issue of tissue contraction. Comparison of wound margins contraction during wound healing between back and tail, n = 2-6 mice (**a**). Haematoxylin-Eosin (H&E) staining of tail and back skin show the absence of panniculus carnosus in tail skin. Dashed line indicates epidermis (**b**). **c**, Percentage of re-epithelialization area at 1w pw1, 2w pw1 and 1w pw2. n = 19-37 wounds. **d**, H&E staining of skin at indicated time points.

P-value (P): **** < 0.0001, ** 0.001 to 0.01, * 0.01 to 0.05, ns ≥ 0.05. Scale bars 300 µm (**b, d**).

It has been shown that when HFSCs leave their niches and take up residence within the repaired tissue, they display enhanced repair ability in case of a second assault through the establishment of epigenetic memory[25]. Importantly, in our experiments, the second wound overlaps the first one, allowing the removal of the HF-derived IFESCs. These cells, activated during the first wound and residing in the newly formed epidermis, were the focus of Gonzales et al., work[25]. Thanks to this strategy we investigated the memory of the HFSCs that remain localised in their original niche in the

HF, without contributing to the repair of the IFE.

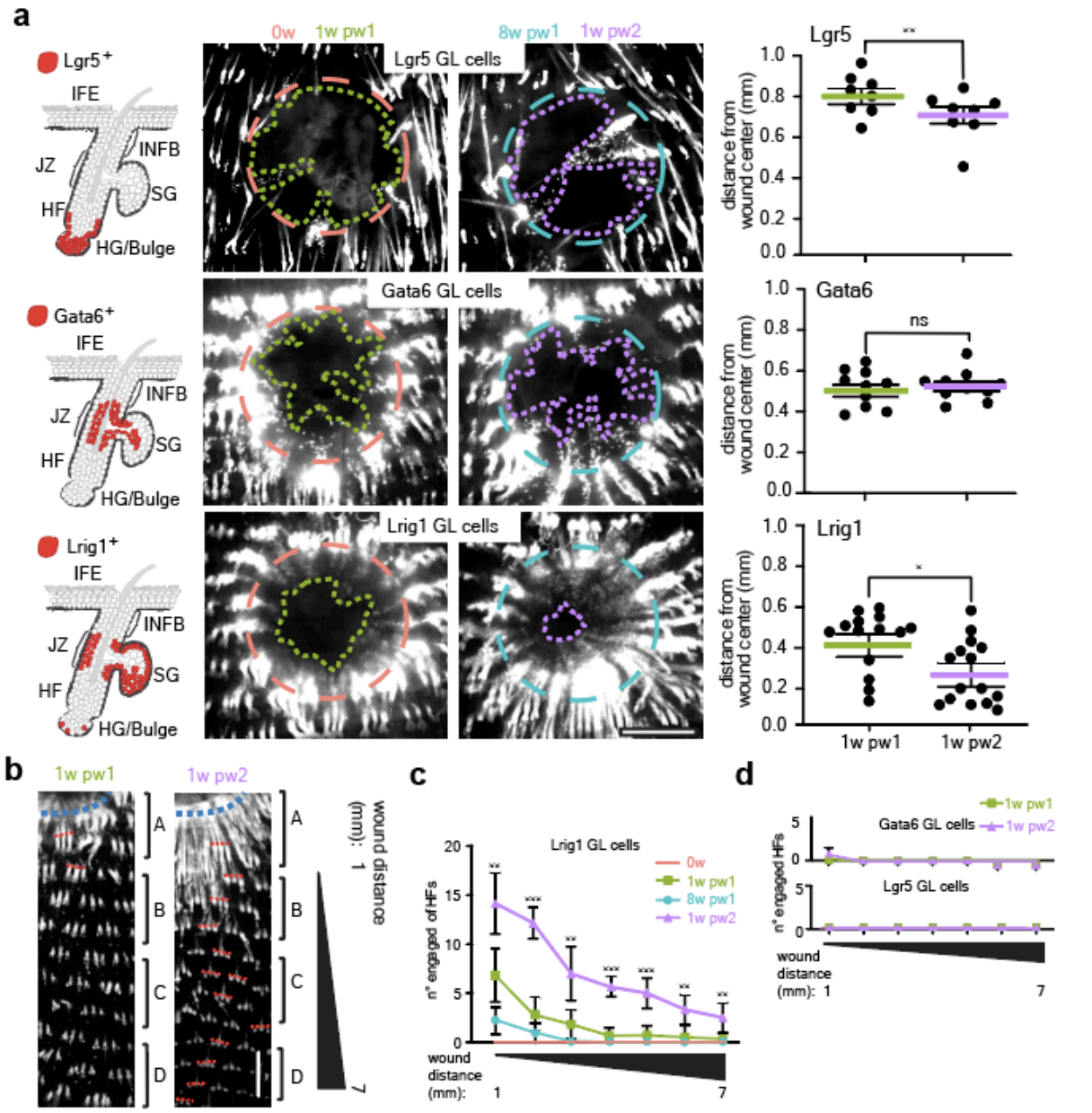

F**igure 2.3. Wound memory in hair follicle lineages and its spatial extension. a**, The localizations of Lrig1$^+$, Lgr5$^+$ and Gata6$^+$ cell populations in the HF are shown. Dashed circles indicate the original wound perimeter at time 8w pw1 (light blue) or 0w (orange) while the lines underline the migration front of the labelled cells at 1w pw2 (purple) or 1w pw1 (green) (**left**). Whole-mount of epidermis (red channel) showing GL tdTomato$^+$ cells exiting from HFs (**centre**) is reported for each population. Quantification of first (1w pw1) and second (1w pw2) wound closure as distance from wound centre. n = 8-14 wounds (**right**). **b**, **c**, HF engagement, as the exit of Lrig1 GL cells from HFs into the interfollicular epidermis (IFE), is shown. Stereoscopic images (red channel) of engaged HFs at 1w pw1 and 1w pw2. Capital letters define the zones at different distances from wound bed: A is up to 1mm from wound bed, B in between 1 and 3 mm, C from 3 to 5 mm and D comprises a region from 5 to 7 mm. Dashed red lines highlight representative engaged HF triplets (**b**). Number of engaged HFs at different distances from wound site, up to 7 mm. n = 6-9 wounds (**c**). **d**, Number of engaged HFs in Gata6 and Lgr5 GL cells 1w pw1 and 1w pw2 up to 7 mm from wound edge. n = 10 wounds. **e**, Confocal representative picture of HF engagement in the 4 zones (A, B, C, D) at 1w pw1 and 1w pw2. Yellow arrows indicate the wound position **f**, Representative confocal pictures of the localization of Lrig1 GL cells (red) relative to zone D (5-7 mm away from wound bed) at the indicated time points. Asterisks represent Lrig1 GL fibroblasts in the dermis. White arrow indicates GL cells exiting into IFE. Yellow arrows indicate the wound position. P-value (P): *** 0.0001 to 0.001, ** 0.001 to 0.01, * 0.01 to 0.05, ns ≥ 0.05. Data are mean ± SD if not differently indicated. Scale bars 1 mm (**a**, **b**); scale bars 100 μm (**e**, **f**).

Despite the contribution of Lrig1 GL cells is quantitatively higher than Lgr5 GL cells, both progenies show enhanced re-epithelialization ability during the second healing (1w pw2) compared to the first one (1w pw1), while Gata6 GL cells do not (Figure 2.3a). These results indicate that differentiating HF cells (here represented by Gata6$^+$ population) do not show wound adaptation while HFSCs, independently of their epidermal lineage, do.

The spatial extent of the wound memory is unknown, although it has been recently shown that the cell contribution to skin full thickness wound repair is spatially restricted to less than 1 mm away from the injury[39], as well as the communication between damaged HFs[40]. Consistently with these observations, during the first healing (1w pw1), the wound-engaged HFs (defined as HF in which GL Tomato$^+$ cells move from their homeostatic HF niche into IFE) are mainly localised in the close surroundings of the injury (Figure 2.3a). However, at 1w pw2 this phenotype exists distally from wound up to 7 mm away from the injury site, exclusively for Lrig1 progeny, while Gata6 and Lgr5 GL cells do not (Figure 2.3b-e). Horizontal whole mount confirmed that Lrig1 GL cells in wound distal areas remain localised in upper HF after the first wound 1w pw1 until 8w pw1, while they exit into the IFE as both basal and suprabasal only at 1w pw2 (Figure 2.3f). This unexpected finding suggests that wound experience educates Lrig1 GL cells resident in distal HFs that did not directly contribute

to the IFE repair. To confirm this, we performed a second injury distant from the site of the previously healed area (zone B (Figure 2.3b) was removed by the second wound) in order to directly challenge distal HFs that haven't been engaged during the first healing. Strikingly, in this setting the distal second healing rate is enhanced, as well as the distal HFs engagement (Figure 2.4a-c), thus confirming that memory is acquired by follicular Lrig1 GL cells also at long distance from the first wound in undamaged areas.

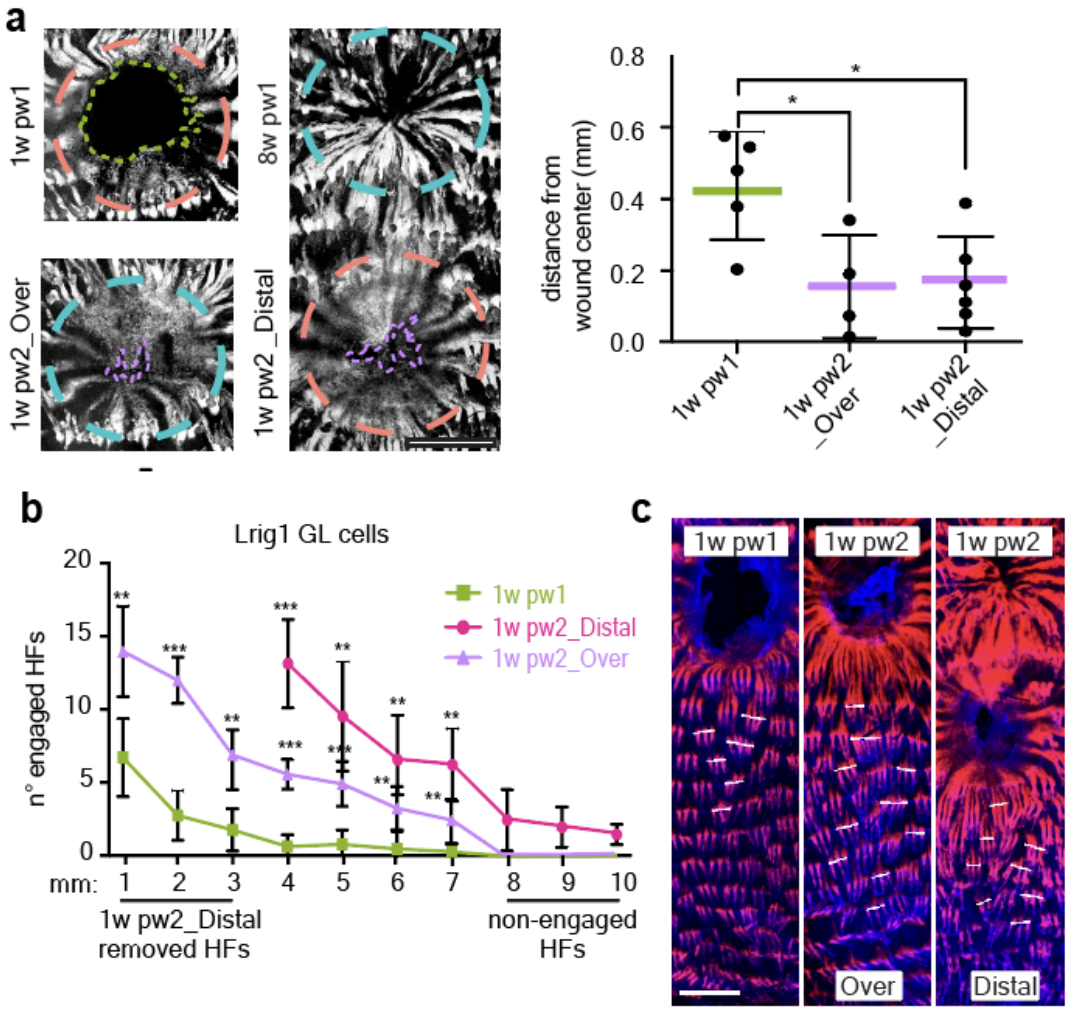

Figure 2.4. Memory is also established distally from the injury. a, Stereo-pictures of the closure of a second overlapping wound (1w pw2_Over) or an injury made distally to the first wound (1w pw2_Distal), in zone B (from 1 to 3 mm) at 1w after wound induction (**left**). Distance from the wound center is quantified in the indicated settings. n = 4-6 wounds (**right**). **b**, **c**, HF engagement is shown for 1w pw1 and 1w pw2, when the second wound is performed overlapped (1w pw2_Over) or distally (1w pw2_Distal) to the first one. Number of engaged HFs at different distances is reported. n = 3-6 wounds (**b**). Confocal images of engaged HFs showing Lrig1 GL cells (red). Dashed white lines highlight representative engaged HF triplets (**c**). P-value (P): *** 0.0001 to 0.001, ** 0.001 to 0.01, * 0.01 to 0.05.

Thus, we show that, as a consequence of a lesion, different SC lineages acquire a wound memory if located in close proximity of the injury. However, exclusively the Lrig1$^+$ SC progeny is wound-educated within the HFs that localise distally from injury, up to ~ 7 mm, to which we will refer as distal memory.

2.2 Distal memory Lrig1 GL cells display enhanced migratory abilities

Since only wound-distal Lrig1 GL cells, but not Lgr5 GL ones, establish distal memory after injury, we compared the expression profile of Lrgi1 and Lgr5 GL tdTomato$^+$ sorted cells to decipher their transcriptional mechanisms. Specifically, we analysed them in a longitudinal population-specific way by RNA-seq experiment. Consistently with their different adaptive phenotype, the analysis shows that the two HFSC lineages have specific wound-associated transcriptional programs (Figure 3.1a). We defined the memory genes as those genes deregulated during the first healing and whose deregulation was of greater magnitude after the second injury. Lrig1 GL cells have a higher abundance of memory genes (almost 50% of the total differentially expressed genes) with respect to Lgr5 GL cells (Figure 3.1b). Gene Ontology (GO) analysis of them suggests the enrichment of cell polarity-related GO terms (i.e. "Golgi stack', "Ruffle membrane" and" Filipodium"), a major cell phenotype in wound healing[39,41], as a feature of the wound-educated Lrig1 GL cells (Figure 3.1c). This corroborates previous histological data about the enhanced migration of Lrig1 GL cells during the second healing (Figure 2.3a), not robustly sustained by proliferation (Figure 3.1d).

To validate the enhanced migratory potential in wound-educated cells located distally from the wound, we collected skin biopsies at 8w pw1 from 2-5 mm far from the wound margins, where engaged HFs reside (Distal) or from control zones (Ctrl) (more than 2 cm far away from wound, where engaged HF are not detected) and we performed *ex vivo* and *in vitro* migration assay[24]. *Ex vivo* migration assay confirmed the higher migratory ability of distal memory Lrig1 GL cells (Distal) when compared to Lrig1 GL cells isolated from control (Ctrl) areas (Figure 3.1e-g) as well an increased cell-polarisation[42] (Figure 3.1h). To understand if the phenotypic advantages of distal memory are preserved in absence of the physiological *in vivo* niche stimuli, we performed *in vitro* assays. Sorted Distal Lrig1 GL cells display a higher migratory potential (Figure 3.1i), when compared

to Ctrl ones. In addition, RNA-seq of cultured Lrig1 GL cells confirms that the enhanced migratory feature of distal memory (in respect to Ctrl) is maintained at transcriptional level *in vitro* (Figure 3.1j,k). Taken together, these data indicate that Distal Lrig1 GL cells acquire enhanced repair capabilities after wound that, once established, are maintained *in vitro* in the absence of their *in vivo* physiological microenvironment.

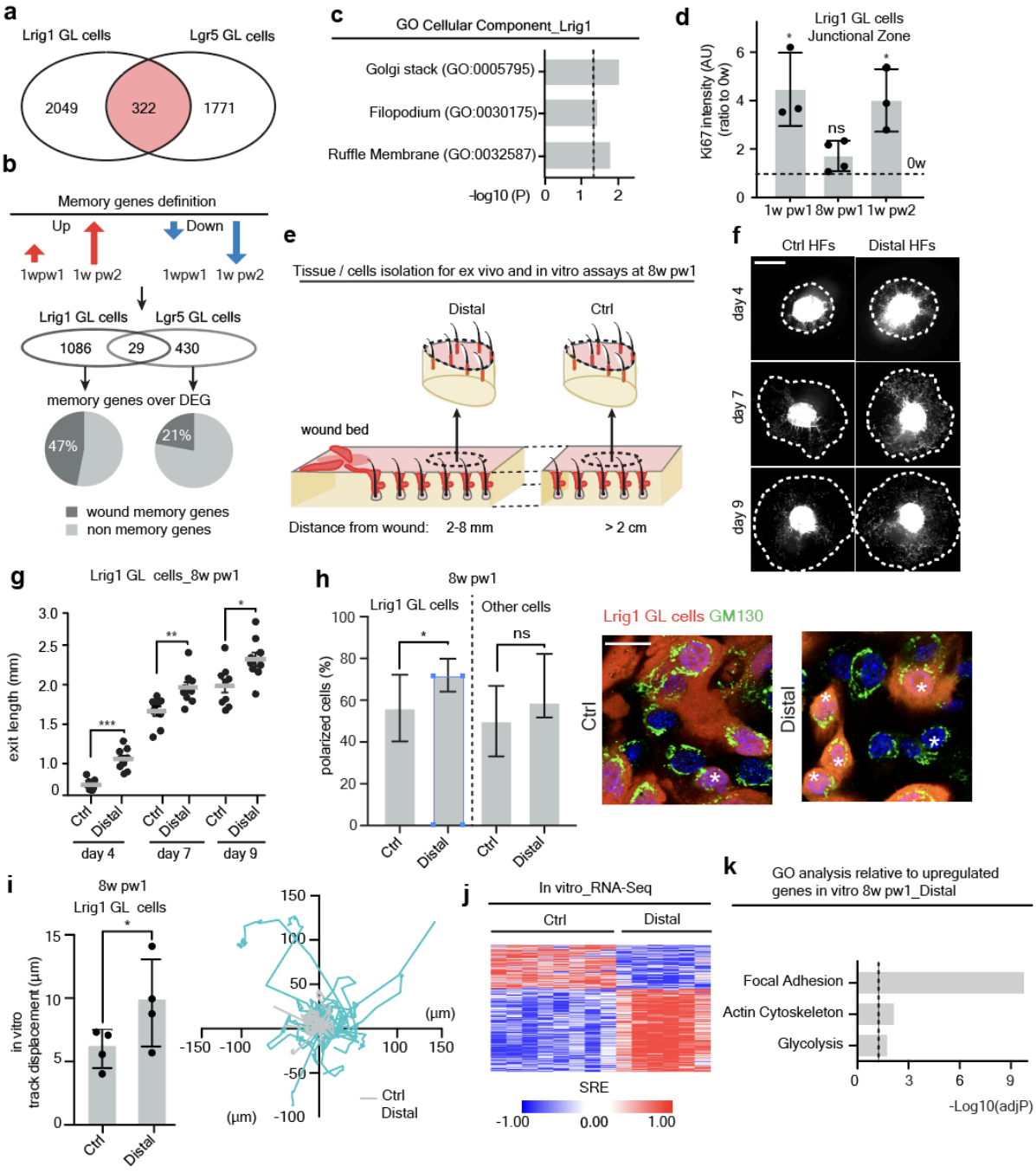

Figure 3.1. Lrig1 progeny displays enhanced fitness after wound experience. a, Venn diagram of unique and shared DEG across the time course between Lrig1 and Lgr5 GL cells identified by RNA-seq. **b**, Memory genes definition (logFC (1w pw2) > logFC (1w pw1)) and Venn diagram reporting the number and the

percentage of inferred memory genes over the total differentially expressed genes (DEG) across the time course in Lgr5 and Lrig1 GL cells. **c**, Enriched GO terms for memory genes in Lrig1 GL cells as -log10 of p-value. Dashed line indicates significance. **d**, Quantification of the Ki67 index in junctional zone (JZ) of Lrig1 GL cells at indicated time points, as ratio to 0w. Dashed line represents 0w mean. n = 3-4 wounds. **e-k**, *Ex vivo* and *in vitro* experimental settings at 8w pw1: Lrig1 GL skin biopsies from wound-educated distal area (Distal- 2 to 8 mm from wound bed) and from control area (Ctrl- > 2 cm from wound bed) are compared. For *in vitro* assays the biopsies were dissociated, and cells were plated in culture dishes. **f**, **g**, Images of *ex vivo* migration of Lrig1 GL cells (**f**) and quantification of the migration (exit length) (**g**). Dashed lines mark the migration front of epidermal cells. Scale bar: 2 mm. Data are mean ± SEM. n = 9 skin explants. **h**, Cis-Golgi (GM130) distribution in cells exiting from skin explant of Distal vs Ctrl. Percentage of polarised cells (marked by asterisk) in GL tdTomato^{+} and tdTomato^{-} cells (left) and representative pictures (right) are shown. Scale bar 20 µm. n = 8-10 explants. **i**, Time lapse migration assay *in vitro*. Track displacement (µm) (**left**) and representative normalized start position graph (**right**) in cultured Lrig1 GL cells over a 16 hours of time lapse. n = 4 mice. **j**, **k**, Lrig1 GL cells from wound-educated distal region (Distal- 3 to 7 mm from wound bed) and Ctrl (distance > 2 cm from wound bed) were analysed by RNA-seq after 1 week of culture. Heatmap of deregulated genes between Distal and Ctrl cells is shown (**j**). The GO analysis relative to upregulated genes in Distal-Lrig1 GL cells is reported, as -log10 of adjusted p-value (AdjP). Dashed line underlines significance (**k**). P-value (P): *** 0.0001 to 0.001, ** 0.001 to 0.01, * 0.01 to 0.05, ns ≥ 0.05. Data are mean ± SD, if not differently indicated.

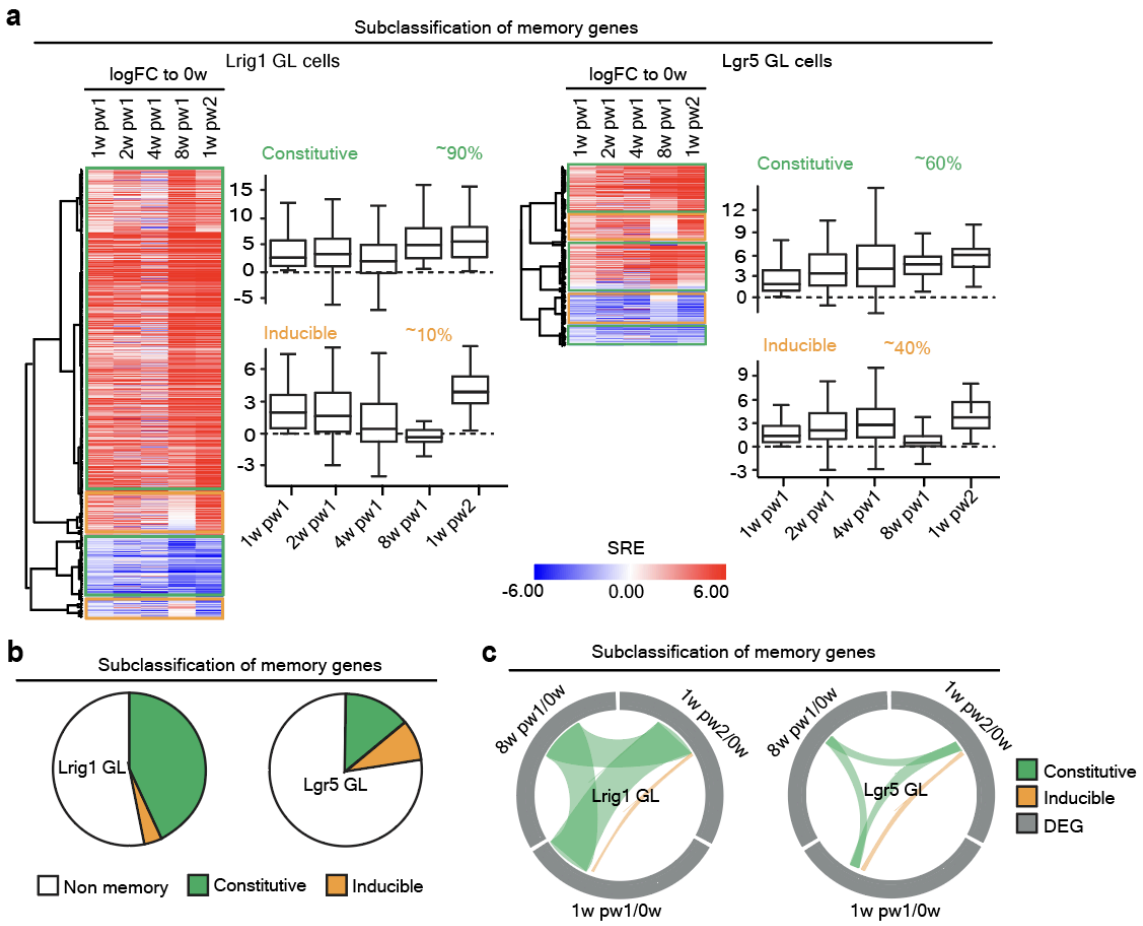

Figure 3.2. Transcriptome analysis of Lrig1 GL cells suggests a new primed subpopulation arising after wound resolution. a, Heatmap of the memory genes shows as logFC of each time point with respect to 0w. Memory genes can be divided into two subtypes, constitutive (green) and inducible (yellow), based on the expression at 8w pw1, related to Figure 3.1b. **b**, Pie chart illustrating the proportions of the memory genes subtypes from RNA-seq of Lrig1 and Lgr5 GL cells in vivo, related to Figure 3.1b. P-value (P): *** 0.0001 to 0.001, ** 0.001 to 0.01, * 0.01 to 0.05, ns ≥ 0.05. Data are mean ± SD, if not differently indicated. **c**, Circular ideogram plot (CIRCOS) of shared DEG (grey) between 1w pw1, 8w pw1 and 1w pw2 (green) or between 1w pw1 and 1w pw2 only (yellow), in Lgr5 and Lrig1 GL skins.

Focusing on the new homeostatic state (8w pw1) in Lrig1 and Lgr5 GL epidermis, the memory genes display two distinct expression patterns (Figure 3.2): (a) a constitutive pattern where the genes remain deregulated in between the two assaults; (b) an inducible trend where, after wound resolution, the original homeostatic expression is restored (0w). Interestingly, in Lrig1 GL cells almost 90% of the memory genes belong to the "a" type. Since 8w pw1 represent a newly established homeostasis (Figure 2.1e-h), we hypothesised that the constitutive and intermediate (in between the two actively healing states) transcriptional activation of memory genes evidenced at 8w pw1 (Figure 3.2) might be due to the existence of *wound priming* in a sub-population of Lrig1 SC progeny.

CHAPTER 3

Transcriptional profiling of memory cells identifies priming as the opted adaptive mechanism

Results II

3.1 Priming occurs in Lrig1 stem cell progeny from distal hair follicles

To better dissect the transcriptional basis of wound memory taking in account the heterogeneity of cells in HF niches[43] we performed single cell RNA-sequencing (scRNA-seq) by Smart-seq2 of ~700 Lrig1 GL cells at four time points: homeostasis (0w), 1 week post first wound (1w pw1), new homeostasis (8w pw1) and 1 week post second wound (1w pw2) (Figure 4.1a).

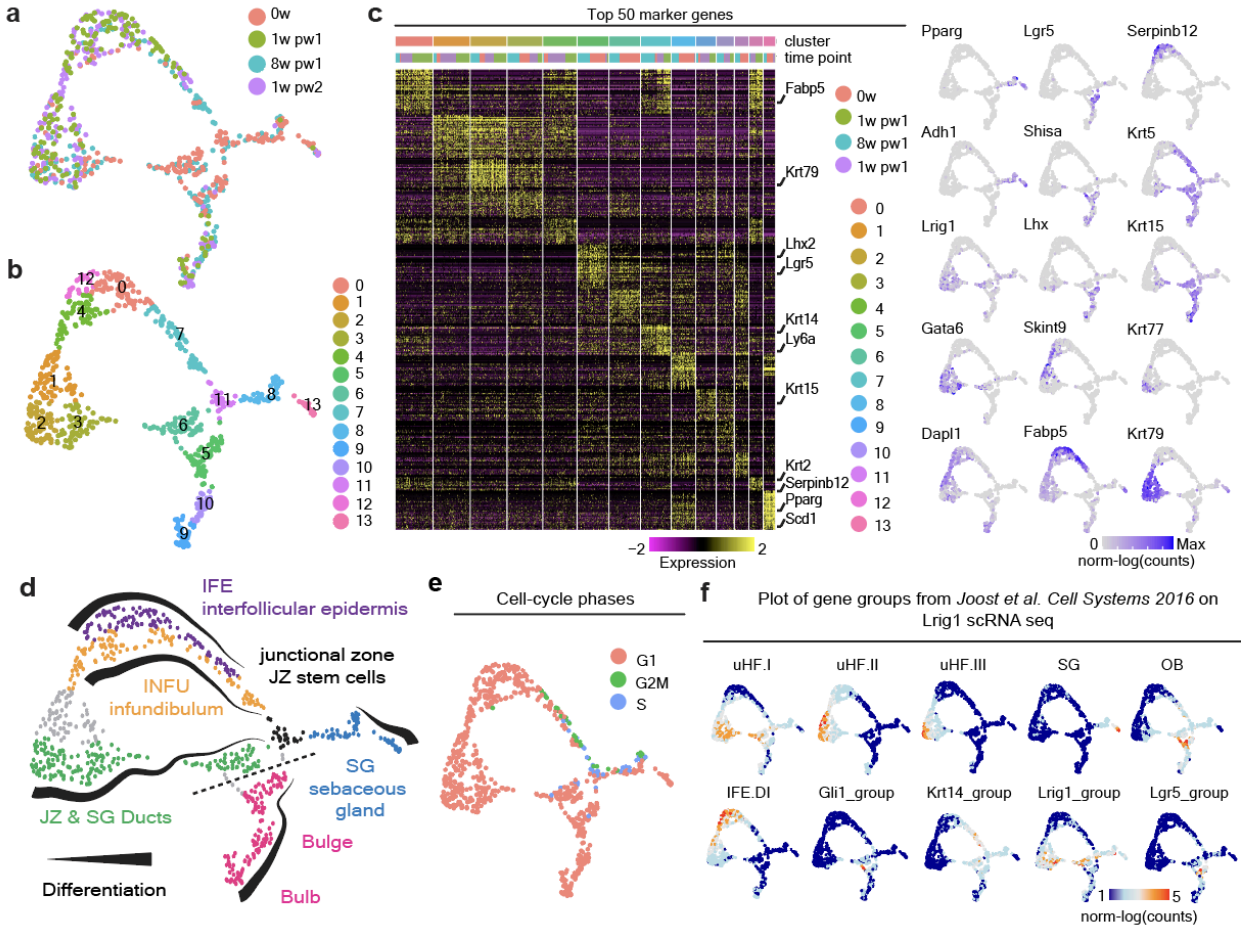

Figure 4.1. Single cell analysis assigns known epidermal niches to cell clusters. a, UMAP of scRNA-seq data of Lrig1 GL cells at 0w (red), 1w pw1(green), 8w pw (light blue) and 1w pw2 (purple). **b**, Unsupervised clustering of single-cell transcriptomic data. **c**, Heatmap representing the 50 top marker genes for each cluster (right) and UMAP of cells coloured by the expression of selected genes (left). Top bars indicate the clusters and the time points. **d,** Summary illustrating epidermal compartments and differentiation in Lrig1 GL single cell data. Cells are coloured according to the epidermal compartment they belong to. Dashed line identifies the homeostatic lineage boundary between upper and lower HF. **e**, UMAP of cells coloured by assigned cell-cycle phase. **f**, Plot of gene set expression from Joost et al. study[43].

Unsupervised clustering analysis (Figure 4.1b) and cluster marker identification (Figure 4.1c) distinguish cells according to spatial location and differentiation stage in known epidermal niches as summarised in Figure 4.1d. Cell-cycle phases classification highlights the proliferative clusters (Figure 4.1e). The integration of our data with scRNA-seq data from Joost et al.[43], that provided markers for cells of epidermal niches and differentiation status, confirms our predictions on the epidermal compartments and the differentiation direction of each cluster (Figure 4.1f). Pseudotime analysis over six trajectories as in Figure 4.2a followed by GO analysis of the upregulated genes at the end of each trajectory shows enrichment of differentiation-related GO terms (Figure 4.2b), corroborating the differentiation direction defined by the pseudotime (Figure 4.2a).

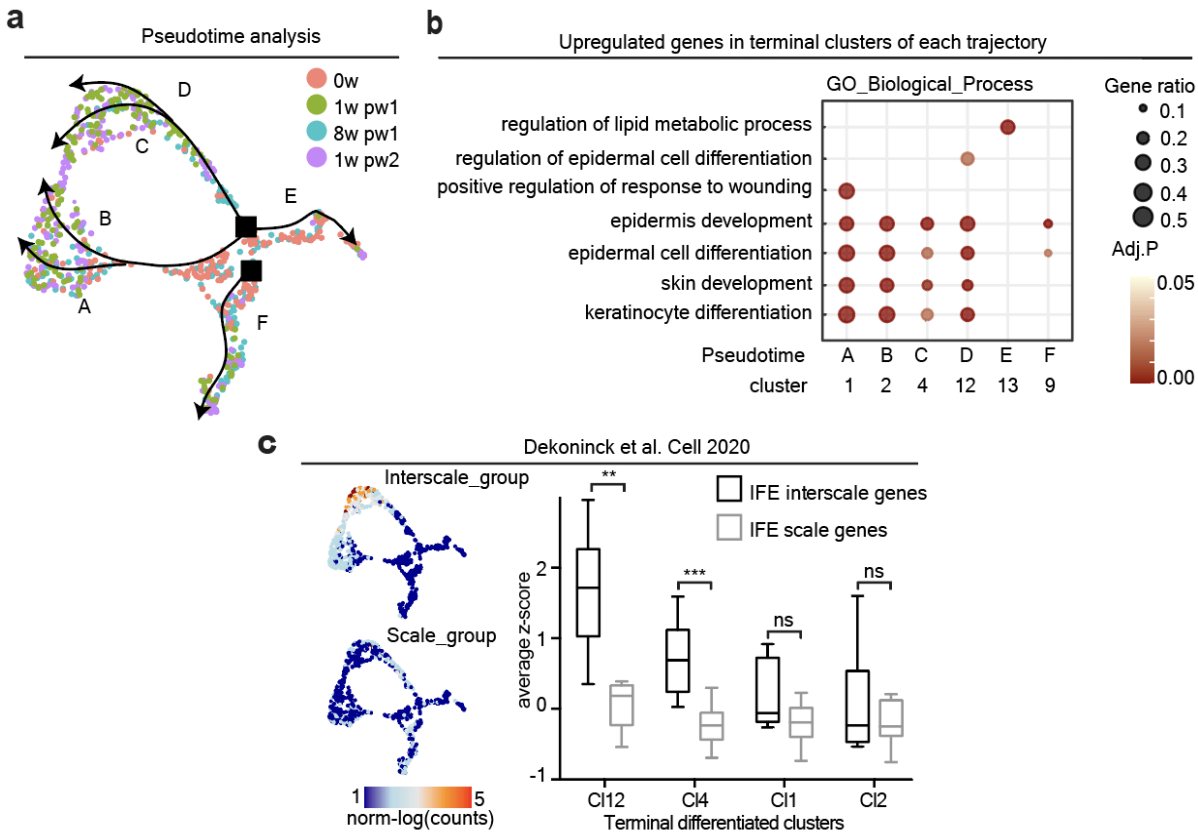

Figure 4.2. Analysis of the pseudotime trajectories. a, Trajectories identified by pseudotime analysis. The starting points (black square) are Cluster 11 (JZ) for the upper HF and Cluster 5 (bulge) for the lower HF. **b**, GO enriched for induced genes in the terminal clusters of each trajectory. Gene ratio (number of genes in the pseudotime/ number of genes in the GO term) and adj. p-value (adjP) are plotted. **c**, UMAP of cells coloured by interscale and scale gene signature (left) and whisker plot of average z-score for scale and interscale gene groups in the epidermal terminal differentiation clusters (1, 2, 4, 12) of each trajectory (right). Gene signatures from Dekoninck et al. study[44]. Data are median with 25th and 75th percentiles. P-value (P): *** 0.0001 to 0.001, ** 0.001 to 0.01, ns ≥ 0.05.

Therefore, the data indicate that: (i) cluster 9 represents differentiated keratinocytes of the lower HF, (ii) cluster 13 is made by sebocytes, (iii) cluster 2 is formed by sebaceous and junctional zone duct cells, (iv) cluster 4 represents the infundibular duct cells and (v) cluster 12 is composed by differentiated IFE cells.

As previously suggested[14], our scRNA-seq data integrated with data from Dekoninck et al.[44] confirm that Lrig1 GL cells can only contribute to the healing with only one of the two differentiated IFE lineages[45], namely the interscale differentiation, but not the scale one (Figure 4.2c).

Trajectory D is the most interesting in terms of wound-induced plasticity. Indeed, within this trajectory, Lrig1^{+} SCs and their progeny of GL cells acquire plasticity while leaving the *Niche of Origin-JZ Cluster* (cluster 11) and move along the trajectory into the *Transition Cluster* (cluster 7) towards the differentiated IFE (cluster 0), where they contribute to the repair (Figure 4.3a). *Transition Cluster* contains cells that reside in the infundibulum (INFU) at the starting point of the trajectory and then move towards IFE at the end of it, as suggested by the expression of the INFU marker Postn[43] (Figure 4.3b). Comparing the two homeostatic stages before the wound (0w) and after the wound (8w pw1), we notice an unexpected increase in the number of Lrig1 GL cells in the INFU at 8w pw1 (Figure 4.3c). Since the infundibular sub-cluster expresses at 8w pw1 intermediate levels of the cluster markers genes in-between homeostatic state 0w and healing conditions (1w pw1 and 1w pw2) and the second induction at 1w pw2 reached greater transcriptional levels in comparison to 1w pw1 (Figure 4.3d), we infer the existence of *priming* adaptive program, as already described as an adaptive program in immune cells[22]. This is also confirmed by GSEA ranking of "Cell activation" signature (Figure 4.3e), that is enriched at 8w pw1 when compared to 0w, and by the expression pattern of Krt6, a marker of wound-activated epidermal cells[46], that is one of the primed

transcripts (Figure 4.3f). Importantly, to confirm the spatial extent of wound memory, Krt6 overexpression is not limited to the wound region, but it is extended to distal HFs (Figure 4.3g). Overall, these results indicate that, consequently to an injury, Lrig1^{+} SC-derived cells occupy the INFU where they remain transcriptionally pre-activated even when the damage has been resolved and a new homeostasis has been reset. We show for the first-time the existence of *priming* as a memory of tissue repair in epithelial context, in sites significantly distant from the wound.

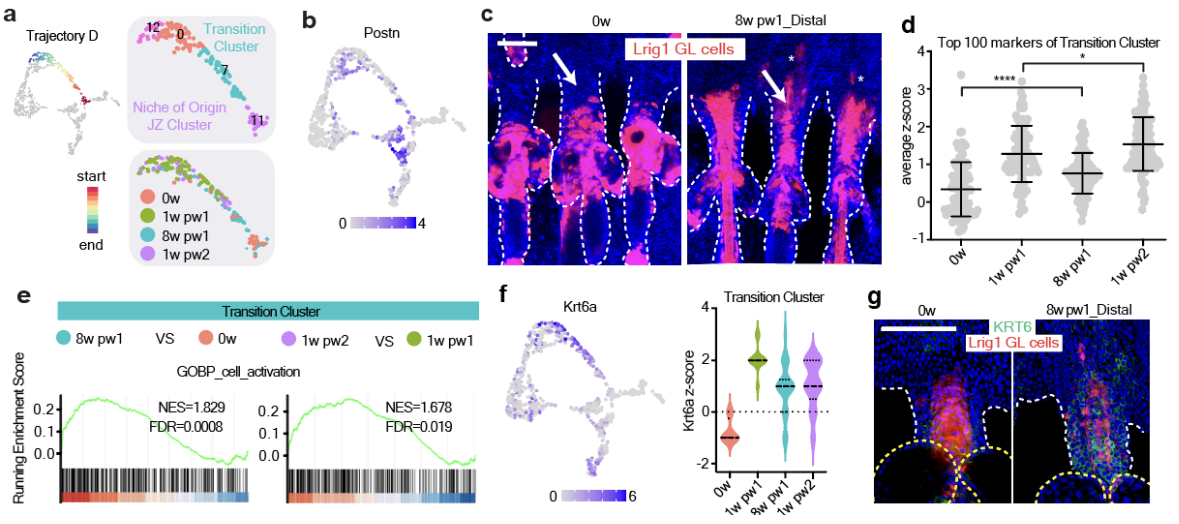

Figure 4.3. Deep analysis of the *Transition cluster*. a, Trajectory D is coloured by time points and clusters. **b**, Postn expression are plotted on the UMAP. Scale in log(counts). **c**, Epidermal whole-mount images of Lrig1 GL tdTomato^{+} cells occupancy of the infundibulum (INFU) at 0w or in the distal HFs at 8w pw1 (at 5 mm from wound site). Asterisks mark differentiated IFE cells. **d**, Plot of the average z-score of the top 100 markers of *Transition Cluster* (cluster 7) showing the intermediate transcriptional state at 8w pw1. **e**, GSEA ranking of the indicated gene signature using the differential gene expression estimates from the comparison 8w pw1 vs is 0w (left panel) and 1w pw2 vs 1w pw1 (right panel) in *Transition Cluster*. **f**, Violin plot of Krt6a expression in cells from *Transition Cluster* in each time point (**left**) and Krt6a expression are plotted on the UMAP. Scale in log(counts) (**right**). **g**, Whole-mount staining pictures at 0w and 8w pw1 (at 5 mm from wound site) are shown. P-value (P): **** < 0.0001, * 0.01 to 0.05.

3.2 Transcriptional basis of Lrig1 GL cells' priming

To dissect the transcriptional basis of *wound priming* in the second homeostasis (8w pw1), we characterised the expression profile of the cells in trajectory D (cluster 11, 7, 0 and 12), separating the first healing process (0w and 1w pw1) from the second one (8w pw1 and 1w pw2) (Figure 5.1a). The heatmap highlights the existence of cell plasticity genes, highlighted in the black square, that are specifically induced at higher levels during the second healing when compared to the first one,

in the *Transition Cluster* (Figure 5.1b). The GO analysis detects enrichment for Actin cytoskeleton, Epithelial-to-Mesenchymal Transition (EMT) and Focal adhesion terms and is consistent with the enhanced migratory abilities previously described (Figure 3.1), as well as Glycolysis, Hypoxia and mTORC1 Signalling related terms (Figure 5.1b and Figure 4.2f).

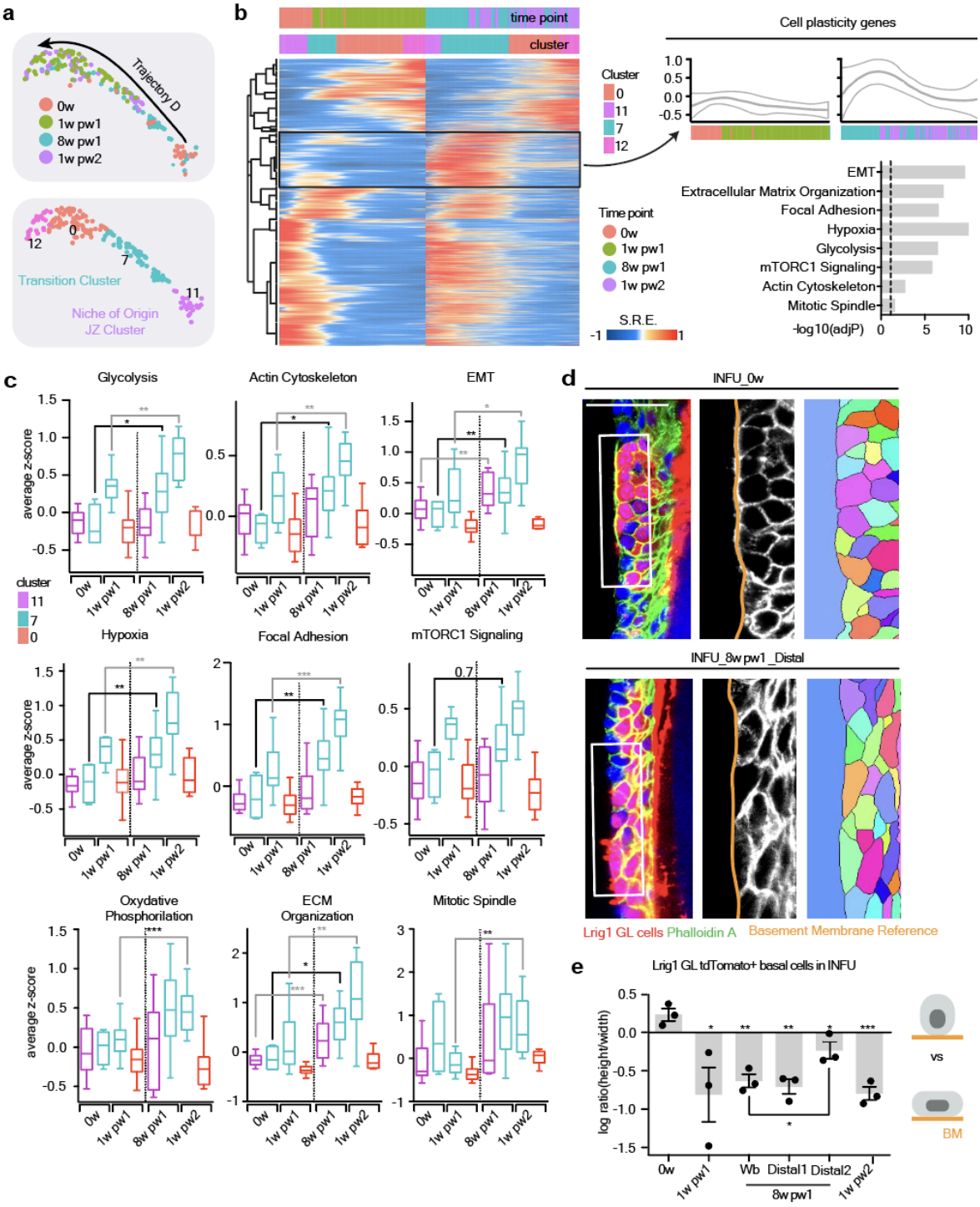

Figure 5.1. Transcriptional characterization of priming cell state. a, UMAP of trajectory D with time point (up) and clusters (down). **b**, Comparison of first and second healing. Left panel: Smoothed Relative

Expression (SRE) of deregulated genes in trajectory D. Clusters and time points are indicated above and transiently induced cell plasticity genes (Extended Data Table 3) are highlighted. Right panel: average z-score expression of cell plasticity genes (up) and GO analysis (down) as -log10 of the adjusted p-value (AdjP). Dashed line underlines significance. **c**, Cells in pseudotime trajectory D are divided by time points and clusters and the average z-score of the indicated GO term is plotted in the whisker plot. Data are median with 25th and 75th percentiles. **d**, Single stack of epidermal whole-mount stained with phalloidin A (green) and relative cell segmentation (right panel) at 0w and distal 8w pw1 at 5 mm from wound bed. Scale bars 50 µm. **e**, Quantification of cell shape as ratio between height and width in Lrig1 GL tdTomato^{+} cells in the infundibulum (INFU) at 0w, 1w pw1, 8w pw1 and 1w pw2. The 8w pw1 sample was analysed in wound bed (Wb) and Distal areas (Distal1- 3 to 5 mm and Distal2- 5 to 7 mm from wound bed). n = 3 mice. P-value (P): **** < 0.0001, *** 0.0001 to 0.001, ** 0.001 to 0.01, * 0.01 to 0.05. Data are mean ± SD, if not differently indicated.

After gathering the cells of the *Transition Cluster* based on time points and clusters, we confirm the intermediate transcriptional state of Lrig1 GL cells at 8w pw1 in-between 0w homeostasis and healing phases (1w pw1 and 1w pw2), relative to the expression of genes within each GO term. Specifically, the wound-primed cells are characterised by a cell state that mostly relies on enhanced metabolism and cell motility (Figure 5.1c). In addition, we find a similar trend for all the GO terms between cells at 8w pw1 and 0w resident in the *Niche of Origin-JZ Cluster* (Figure 5.1c), indicating that, beside the primed cells in INFU, some Lrig1^{+} SCs in JZ adapted to wound healing. Consistently with cell motility-related GO terms analysis, the infundibular Lrig1 GL cells display an elongated shape at 8w pw1, when compared to typical cuboidal-shape at 0w (Figure 5.1d).

Strikingly, this memory-associated cellular phenotype, once again, is not restricted to the HFs localised at wound proximity but it is also spatially organised in distal HFs with a gradient pattern (Figure 5.1e), as previously observed (Figure 4.3g).

Concerning the metabolic state, Hypoxia, Glycolysis and Oxidative phosphorylation GO terms are significantly enriched in the *Transition cluster* of second wound healing, suggesting an enhanced metabolic state. The glycolytic state is assessed evaluating the levels of Glut1 (Slc2a1), a marker of highly glycolytic cells[47], that is upregulated specifically in the *Transition Cluster* in actively repairing cells and strongly induced at 1w pw2 compared to 1w pw1 (Figure 5.2a,b). Flow cytometry quantification validates the Glut1 modulation in our two consecutive injuries model highlighting the increased number of Glut1-expressing Lrig1 GL cells at 8w pw1 when compared to time 0w (Figure 5.2c). From a spatial point of view, Glut1, as markers of primed cells at 8w pw1, display a gradient pattern with high signal closer to the wound and an intermediate signal in distal memory areas (up

to ~7 mm from wound) that became weaker further away, in non-memory areas (Figure 5.2d). This pattern matches the other observations on Krt6 and cell shape changes (Figure 4.3g and Figure 5.1d), corroborating the spatial extent of wound-elicited cell education.

MitoTracker is used to validate Oxidative Phosphorylation (Figure 5.2e) GO term and it confirms the scRNA-seq. These data support the enhanced metabolism scenario.

Finally, the enhanced migratory potential of isolated distal memory cells (Glut1^{+}TdTomato^{+}) relative to non-memory counterpart (Glut1^{-}TdTomato^{+}) represents clear evidence of the functional implications of distal priming on cell fitness (Figure 5.2f).

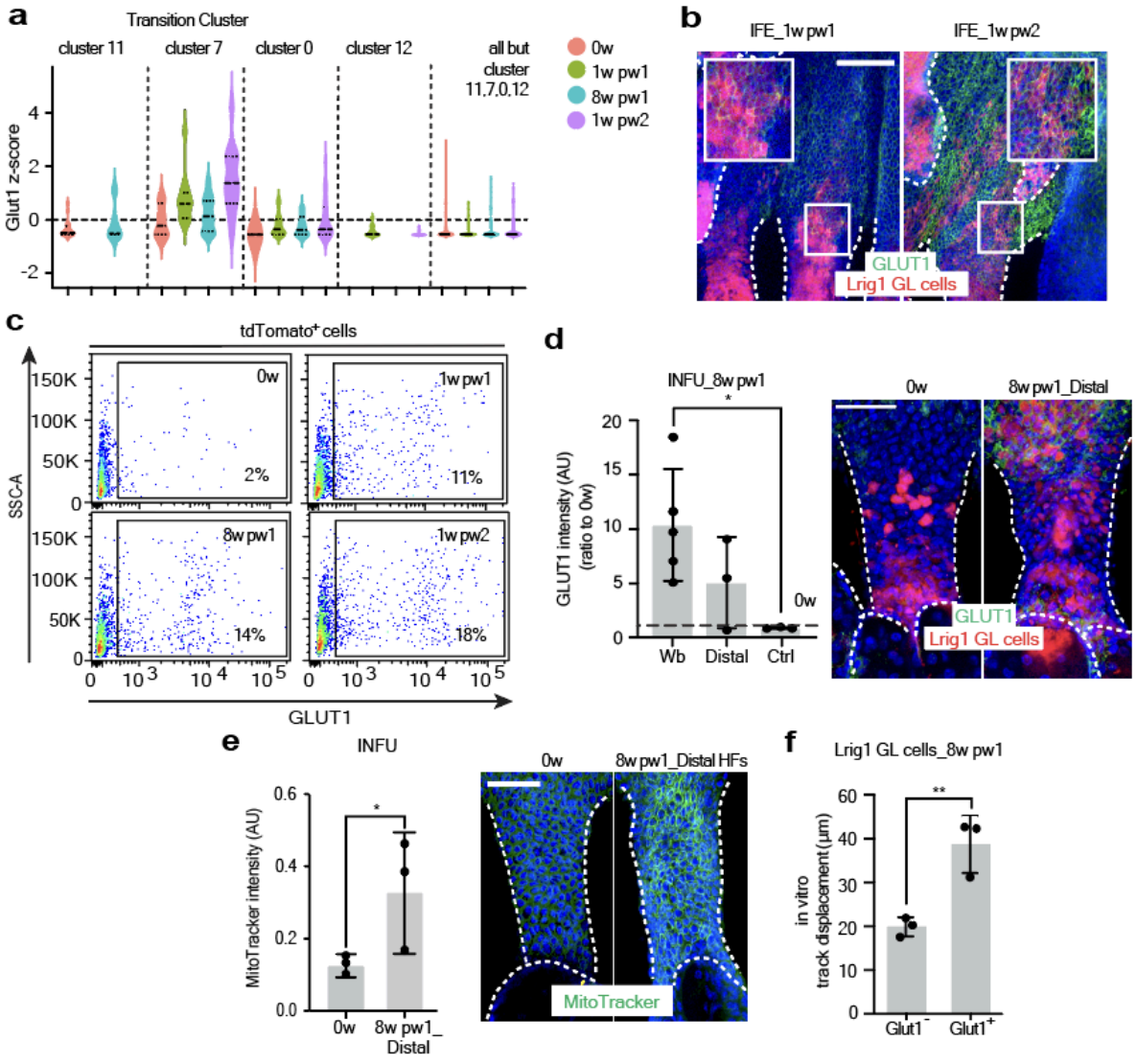

Figure 5.2. Cell priming relies on enhanced metabolism. **a**, Violin plot of Glut1 expression in cells from cluster 0, 7, 11, 12 and all the others. Cells are divided by time point. **b**, Whole-mount staining of GLUT1 in 1w pw1 and 1w pw2. **c**, Gating strategy of Glut1^{+} tdTomato^{+} cells and quantification at the indicated time points. Gates are set on negative controls. n = 4-6 wounds. **d**, Quantification of GLUT1 level in the INFU at 8w pw1, in

Wb, Distal and Ctrl (>2cm from Wb) (ratio to 0w) (left) and whole-mount staining pictures at 0w and 8w pw1 at 5 mm from wound site (right) are shown. n = 3-5 mice. **e**, Quantification of MitoTracker index in INFU (left) and HF images (right) at 0w and 8w pw1_Distal, 5 mm from wound site. n = 3 mice. **g**, Time lapse migration assay *in vitro*. Mean track displacement (µm) of cultured 8w pw1 Glut1^{+} vs Glut1^{-} Lrig1 GL tdTomato^{+} cells. n = 3 mice. P-value (P): ** 0.001 to 0.01, * 0.01 to 0.05. Data are mean ± SD, if not differently indicated. Scale bars 50 µm (**b**, **d**, **e**).

Overall, the integration of scRNA-seq with histological validations allows a deep characterization of wound-primed cells resident in distal HFs, that relies on high metabolism and enhanced migration rate. Strikingly, the transcriptional data together with the histological analysis of the molecular signature of *priming* shows a spatial distribution of pre-activated Lrig1^{+} GL cells in the INFU, corroborating the existence of an unexpected large spatial extent of *wound priming.*

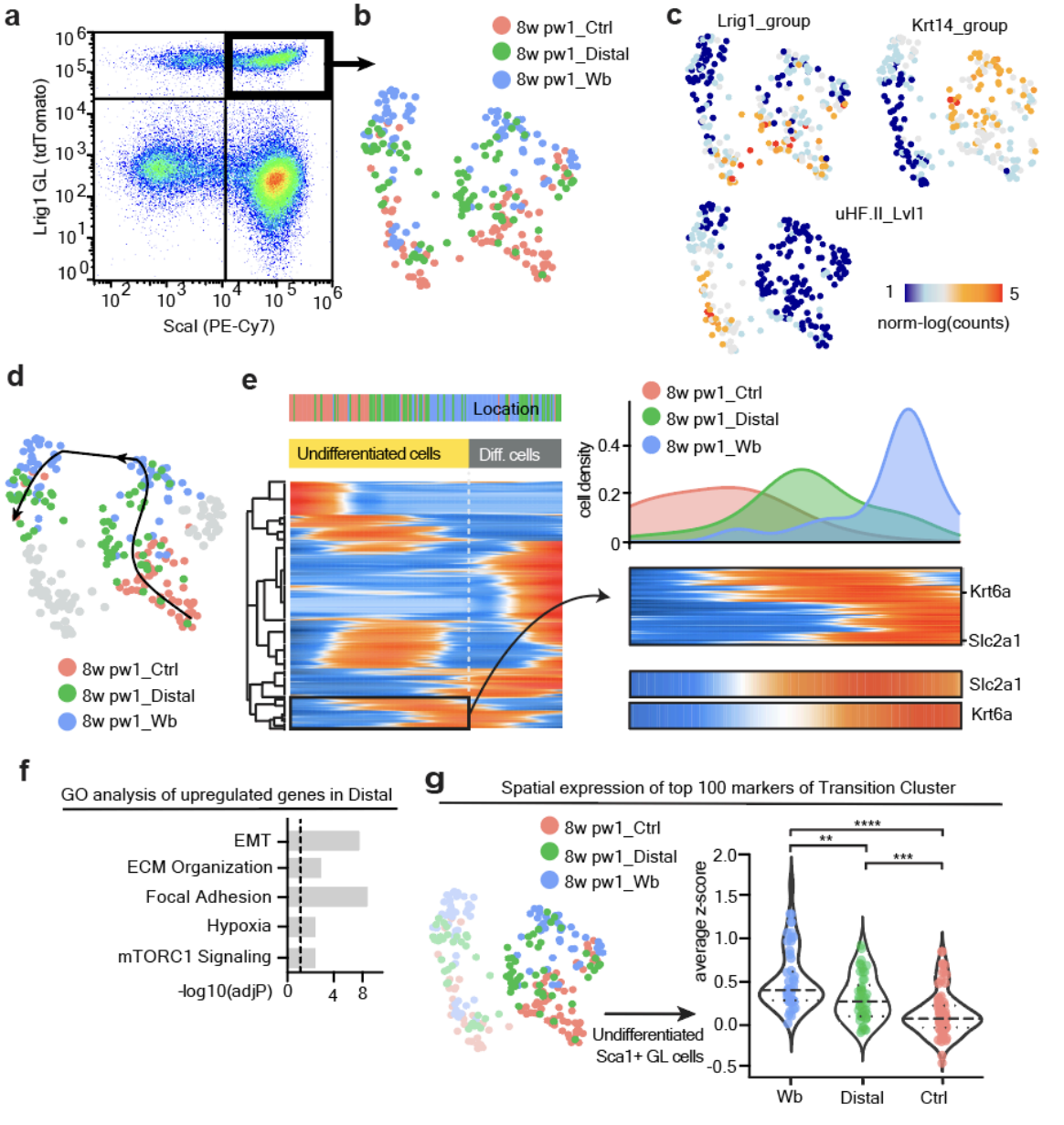

Figure 5.3. Spatially resolved single cell RNA-seq confirms distal priming. a-g, Spatially resolved scRNA-seq analysis of upper-HF Lrig1 GL cells from wound bed (Wb), distal memory region (Distal- 3 to 7 mm from Wb) and non-memory region (Ctrl- > 2 cm from Wb) was performed at 8w pw1 and analysed. **a**, Gating strategy for tdTomato-Sca1 double positive cells sorting. Negative controls are used to set the gate. **b**, UMAP of the spatially resolved scRNA-seq with cells coloured by location (Wb, Distal or Ctrl). **c**, Plot of gene group expression from Joost et al. study[43]. Normalised log(counts) is plotted. **d**, **e**, Pseudotime analysis from undifferentiated upper HF cells to differentiated upper HF cells is performed, as in the case of the Trajectory D in Fig.4a. **d**, Trajectory identified by pseudotime analysis. **e**, Smoothed Relative Expression (SRE) of deregulated genes along the pseudotime trajectory. Cell location respect to wound bed (as Ctrl in red, Distal in green and Wb in blue) is indicated above. The analysis of undifferentiated cells highlights the existence of a gene set expressed in Distal and Wb cells but not in Ctrl (black rectangle magnified in right panel). Importantly, Glut1 (Slc2a1) and Krt6 are included in the gene set (right). **f**, Enriched GO terms of the gene set expressed in Distal and Wb cells but not in Ctrl, identified in (**e**) are plotted as -log10 of the adjusted p-Value (AdjP). The dashed line underlines significance. **g**, Plot of average z-score expression of the 100 markers of the *Transition Cluster* identified in Fig.3g in the cells from each group. P-value (P): **** < 0.0001, *** 0.0001 to 0.001, ** 0.001 to 0.01.

To further confirm the gradient spatial distribution at molecular level, we performed an additional scRNA-seq of Lrig1 GL cells at 8w pw1, where we separately isolated and processed cells located in the wound bed area, in the distal memory area or far away (non-memory area) (Figure 5.3a-g).
To profile specifically the upper-HF memory cells, we sorted Ly6a/Sca-1^{+} Lrig1 GL[12] (Figure 5.3a) and we evaluated the expression of the *Transition Cluster* markers genes previously identified (Figure 4.3d) in Wb, Distal and Ctrl scRNA-seq data. Strikingly, these markers display the same spatial gradient as Krt6 (Figure 4.3g) and of other primed transcripts such as Glut1 (Figure 5.2d), and the same GO terms enrichment as the previous scRNA-seq (Figure 5.3e,f), proving the existence of transcriptionally primed cells distally from the wound bed (Figure 5.3g), definitely confirming the spatial gradient of Lrig1 GL cells' *priming*.

3.3 Lineage specificity of epidermal cells' priming

Bulge SCs have been shown to exhibit wound adaptation after becoming resident in the repaired niche[25]. Our bulk RNA-seq analysis on Lgr5 GL cells together with the histological data, confirm that Lgr5 progeny could be wound-trained even in its own niche, as Lrig1 GL cells do, but with its own individual transcriptional program. To dissect the adaptation program of Lgr5^{+} bulge SC progeny we performed longitudinal scRNA-seq on Lgr5 GL cells. Importantly, as evidenced by histology and

scRNA-seq data (Figure 6a-d), no Lgr5 GL cells occupy the INFU when homeostasis is re-established at 8w pw1, demonstrating that only activated Lrig1^{+} SCs give rise to the infundibular primed cells (Figure 6a). The *Transition Cluster* contains actively repairing Lgr5 GL cells (1w pw1 and 1w pw2) that are Glut1 and Krt6a positive (Figure 6d), as for Lrig1 lineage. Targeted analysis of the GO terms enriched in Lrig1 GL cells reveal that Lgr5 GL cells at 8w pw1 are transcriptionally comparable to cells at 0w (Figure 6e), suggesting the absence of a substantial cell priming.

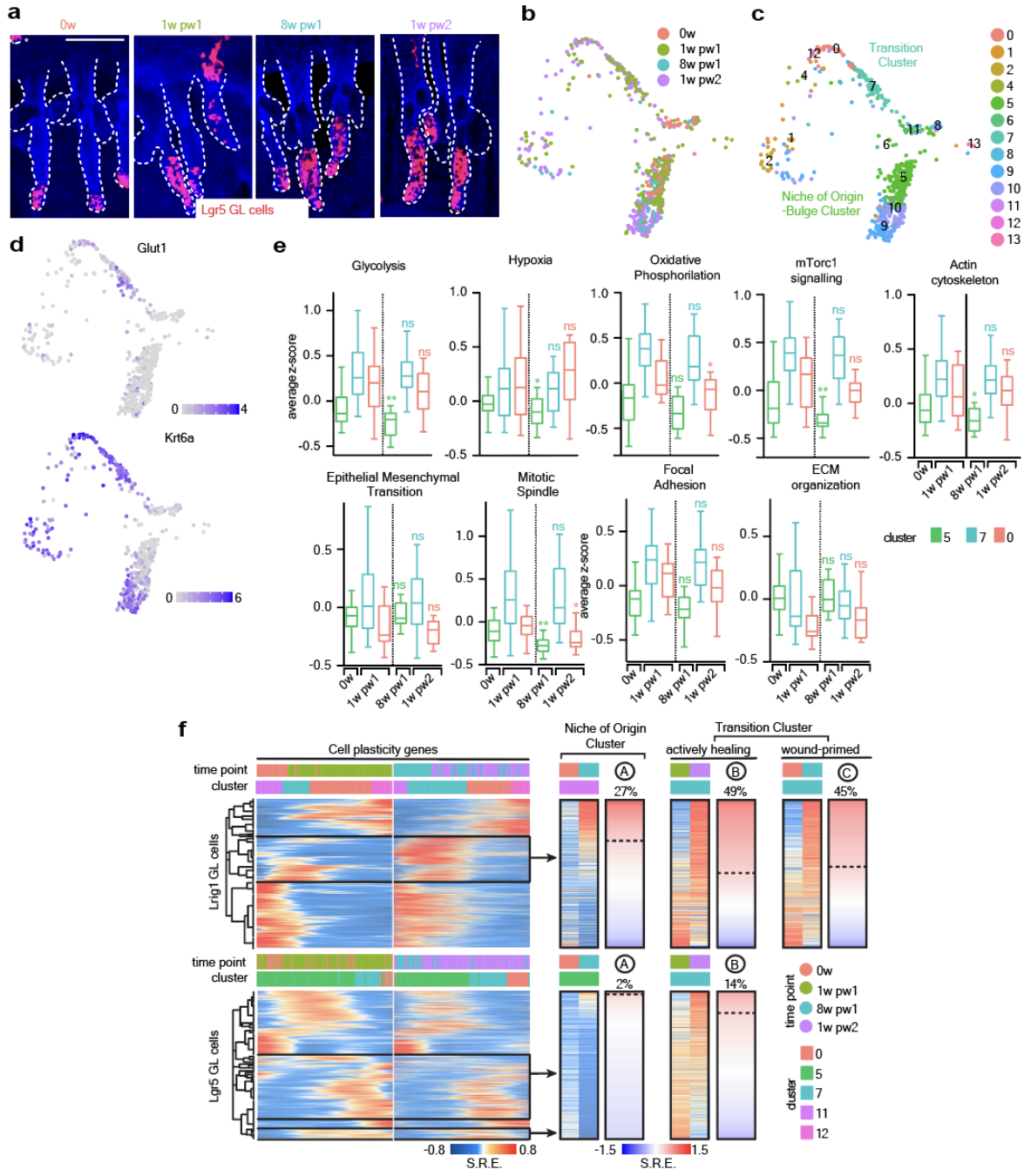

Figure 6. Comparison between single cell profiling of Lgr5 and Lrig1 lineages. a, Representative confocal pictures of Lgr5 GL HF triplets from tail skin at the indicated time points. Lgr5 GL cells exit from their

niche, but they disappear by 8w pw1 if out of the bulge. Scale bar: 150 µm. **b-f,** Single cell data from Lgr5 GL cells (0w, 1w pw1, 8w pw1 and 1w pw2). UMAP of cells coloured by time points (**b**), clusters (**c**). **d**, Glut1 and Krt6a expression levels are plotted on the UMAP. Scale in log(counts). **e**, Whisker plots of the average expression of each GO term enriched in Lrig1 GL single cells (Fig.4b). Data are median with 25th and 75th percentiles. For statistical analyses cells at 0w vs 8w pw1 or 1w pw1 vs 1w pw2 were compared within the same cluster. **f,** Left panel: Smoothed Relative Expression (SRE) of deregulated genes in the clusters 0, 7, 11 and 12 for Lrig1 GL cells (up) and 5, 7 and 0 for Lgr5 GL cells (down). Clusters and time points are indicated above, and transiently induced cell plasticity genes are highlighted (black rectangle), as in Fig.4b. Right panel: the pattern and the percentage of cell plasticity genes are shown for: "A" cells in the *Niche of Origin Cluster* (cluster 5 for Lgr5 GL and cluster 11 for Lrig1 GL cells); "B" actively healing cells at 1w pw1 and 1w pw2 in *Transition Cluster*; "C" wound-primed cells at 8w pw1 in *Transition Cluster* only exists in Lrig1 GL cells. P-value (P): ** 0.001 to 0.01, * 0.01 to 0.05, ns ≥ 0.05.

To directly compare the two lineages, we performed pseudotime analysis on Lgr5 GL cells where cluster 5 (the *Niche of Origin-Bulge Cluster*) is used as the starting point of the trajectory D (Figure 6f). Focusing on cell plasticity genes in the two D trajectories we notice that: (i) priming of Lgr5 SCs in their niche of origin is extremely limited compared to Lrig1$^+$ SCs (cell subset "A" in Extended Data Fig.8h), suggesting that the bulge-derived progeny adapt through a trained memory strategy as previously demonstrated[25]; (ii) activated Lgr5 GL cells at 1w pw2 has a smaller enhanced transcriptional activation in comparison with Lrig1 GL cells, consistently with their lower contribution to repair (Fig.1c and Extended Data Fig.3b) (cell subset "B" in Extended Data Fig.8h); (iii) only Lrig1 GL cells has a primed adaptive memory after first injury while establishing an INFU progeny, long after injury resolution and still constitutively express cell plasticity genes (cell subset "C" in Figure 6f). Thus, we conclude that, in the context of skin full-thickness wound, the Lgr5$^+$ SCs display a trained adaptation to wound, consistently to what was previously shown in the context of intermediate wound[25]. However, primed cells are peculiar to the Lrig1 SC progeny.

CHAPTER 4

Wide epigenetic rearrangements support the transcriptional priming of memory cells

Results III

4.1 Chromatin profiling of memory cells

To evaluate the consequences of wound adaptation at chromatin level we performed ATAC-seq of Lrig1 GL cells at 0w, 1w pw1, 8w pw1 and 1w pw2. To enrich the upper-HF memory cells, we sorted tdTomato^{+} Ly6a/Sca1^{+} epidermal cells, as in Figure 4.3a, from the distal memory area (wound bed and wound proximal 0-2mm area were excluded) (Figure 7a-e). We observe a global chromatin opening at 1w pw1 and 1w pw2 with respect to 0w and as well as to 8w pw1, although with fewer events when compared to the active healing phases (Figure 7a). The vast majority of chromatin opening events at 8w pw1 were shared by both 1w pw1 and 1w pw2 conditions, with 1665 common peaks at 1w pw1, 8w pw1 and 1w pw2, that we defined as wound memory peaks (Figure 7b-d). GO analysis of the genes associated to the memory peaks reveals an enrichment of the same GO terms (i.e. Glycolysis, Focal Adhesion, EMT and mTORC1 Signalling) (Figure 7e) as for distal priming transcriptional program, identified by scRNA-seq in Figure 5.1b. These data indicate that the transcriptional program of priming is overall maintained at 8w pw1 through the chromatin opening of wound-associated genomic loci, relative to metabolic and migratory genes.

We conclude that the transcriptional priming is supported by an increase in chromatin accessibility in genes associated to metabolism and migration, acquired after the first injury, and maintained ever since.

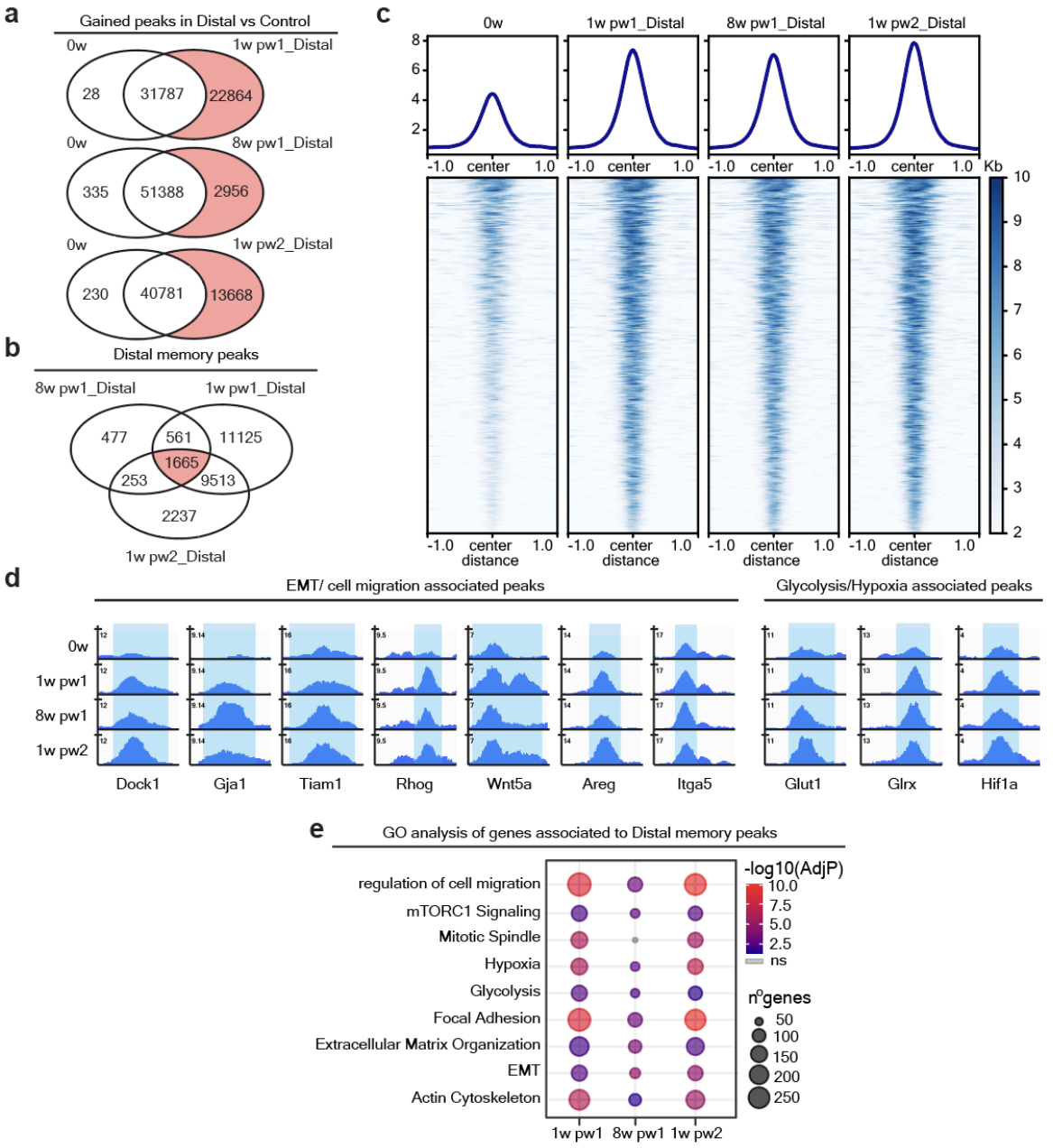

Figure 7. Chromatin remodelling in distal priming. a-e, ATAC-seq of sorted Lrig1 GL upper HF cells (Sca-1^{+}) at 0w and at 1w pw1, 8w pw1 and 1w pw2 from distal memory areas **(**Distal- from 3 mm to 7 mm from wound bed). **a**, Venn diagrams of ATAC-seq peaks (logFC > 0.5, P < 0.05) from distal memory area (Distal) at 1w pw1, 8w pw and 1w pw2 respect to 0w (numbers indicated on diagram). Gained peaks are highlighted in red. **b**, Venn diagram of the gained peaks at 1w pw1, 8w pw1 and 1w pw2 vs 0w show shared 1665 distal memory peaks (red). **c**, Density plots depict ATAC-seq signals ± 1 kb of distal memory peaks (up) and heatmap of the signal score of individual peaks (down) (**c**). **d**, Snapshots of genomic loci of representative distal memory peaks. **e**, GO analysis of genes associated with gained peaks at 1w pw1, 8w pw1 and 1w pw2 vs 0w. -Log10 of adjusted p-value (AdjP) is represented by colour scale and gene number by dot size.

4.2 Long-range priming relies on the downregulation of H2AK119ub repressive mark

Several transcription factors, key determinants in inflammatory memory[23], are likely to be functional also in wound memory. However, in both the wound adaptation programs acquired by epithelial cells, such as trained immunity-like[23,25] and priming (this manuscript), the epigenetic regulators are still completely unknown.

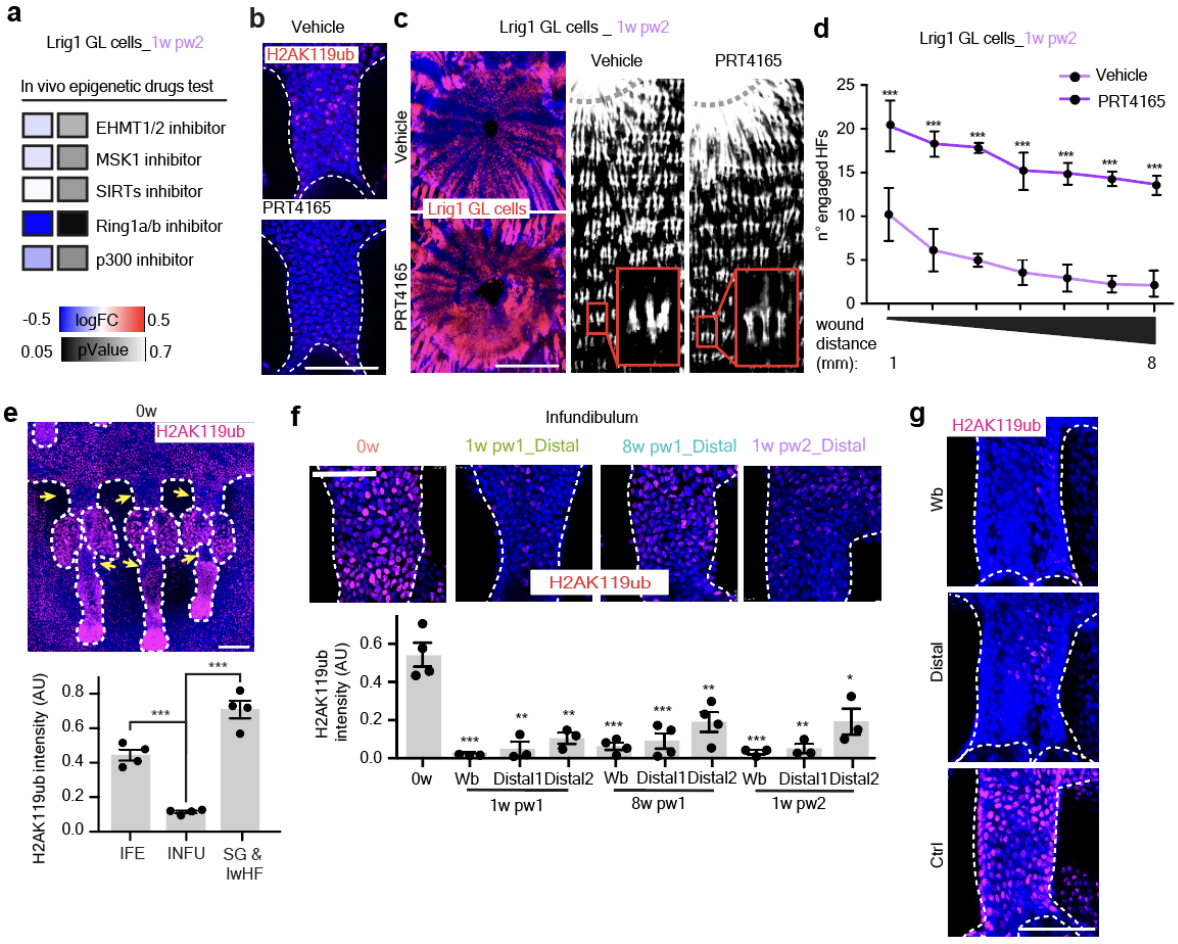

Figure 8.1. The reduction of H2AK119ub is physiological after wound in distal memory areas. a, Effect of 5 epigenetic drugs on wound closure at 1w pw2. 8w pw1 mice are treated 3 times with the reported inhibitors before wound induction. Wound closure rate (as the distance of cells from wound center at 1w pw2) is quantified and plotted as logFC to vehicle-treated mice. Only the Ring1a/b inhibitor (PRT4165) is significantly able to increase wound closure rate. n = 4-9 wounded mice. **b**, PRT4165 treatment reduces H2AK119ub in upper HF. **c,** Representative pictures of the effect of PRT4165 on wound closure (left) and distal HFs engagement in Lrig1 GL tdTomato^{+} mice at 1w pw2. Scale bar 1mm. **d**, Number of engaged HFs at 1w pw2 at different distances from wound after vehicle and PRT4165 treatment. n = 7-8 wounds. **e**, Homeostatic levels of H2AK119ub in HFs and relative quantification in interfollicular epidermis (IFE), infundibulum (INFU), sebaceous gland (SG) and lower HF (lwHF). INFU is the compartment with lower levels of H2AK119ub in homeostasis. n = 4 mice. **f**, Confocal pictures (**up**) and quantifications (**down**) of H2AK119ub in infundibulum (INFU) at 0w, 8w pw1, 1w pw1 and 1w pw2, relative to Fig.7a. Wound bed (Wb) and two different distal memory regions

(Distal1- 3 to 5 mm and Distal2- 5 to 7 mm apart from wound bed) are compared to 0w. n = 3-4 wounds. **g**, H2AK119ub levels at 40 weeks post wound (40w pw1) homeostasis in wound bed (Wb), distal memory region (Distal- 3 to 7 mm from wound bed) and control area (Ctrl- >2 cm from wound bed). P-value (P): *** 0.0001 to 0.001, ** 0.001 to 0.01, * 0.01 to 0.05. Data are mean ± SD, if not differently indicated. Scale bars 100 μm (**b**, **e**, **f**, **g**).

To this aim, we tested *in vivo* some epigenetic drugs in Lrig1 GL mice to target five transcriptionally relevant histone modifications, trying to modulate the memory of wound-primed cells at 8w pw1 (Figure 8.1a). PRT4165 inhibits the enzymatic activity of Ring1a/Ring1b, component of the Polycomb repressive complexes 1 (PRC1), responsible for the monoubiquitination of lysine 119 on histone H2A (H2AK119ub) (Figure 8.1b) [48–50]. Pre-treatment with PRT4165 does not only lead to a more efficient healing at 1w pw2 (Figure 8.1c) but also, more importantly, to an increased engagement of HFs located distally from the injury site (Figure 8.1c,d). To verify the physiological role of PRC1 in wound priming, we stained whole-mount epidermis for H2AK119ub at 0w, 1w pw1, 8w pw1 and 1w pw2. In homeostasis, the JZ and the INFU already express lower levels of this histone modification, when compared to other epidermal compartments (Figure 8.1e). When injury occurs and chromatin becomes more accessible[23], H2AK119ub repressive mark decreases in INFU during both wound healing time points (1w pw1 and 1w pw2), with a major effect at 1w pw2. When the new homeostasis is re-established (8w pw1), the H2AK119ub mark is not restored at the original 0w levels (Figure 8.1f), not even 40 weeks post-wound (aged new homeostasis) (Figure 8.1g). Importantly, the decrease in H2AK119ub is also evident in the INFU of wound-distal HFs (Figure 8.1f).

Since the reduction of H2AK119ub follows the spatial distribution of wound-primed cells, we hypothesised that H2AK119ub might be a key functional component in distal priming through a transcriptional de-repression mechanism. To verify it, after genetic labelling, we pretreated 0w epidermis with PRT4165 (PRC1i) and we induced an injury (Figure 8.2a). PRC1i indeed elicits an enhanced healing rate by Lrig1 GL progeny (Figure 8.2b,c). Strikingly, wound-distal HFs are also engaged (Figure 8.2d).

To assess whether PRC1i promotes features of wound memory even at transcriptional level through the de-repression of genes associated to *wound priming*, we performed a scRNA-seq on vehicle or PRC1i-treated Lrig1 GL mice (Figure 8.2e-g). Even in the absence of an injury, PRC1i activates several pathways previously identified in the physiological memory of primed cells, especially genes related

to GO terms such as Glycolysis, EMT and Actin cytoskeleton (Figure 8.2g,h) in Lrig1 GL cells in the *Niche of Origin-JZ Cluster*.

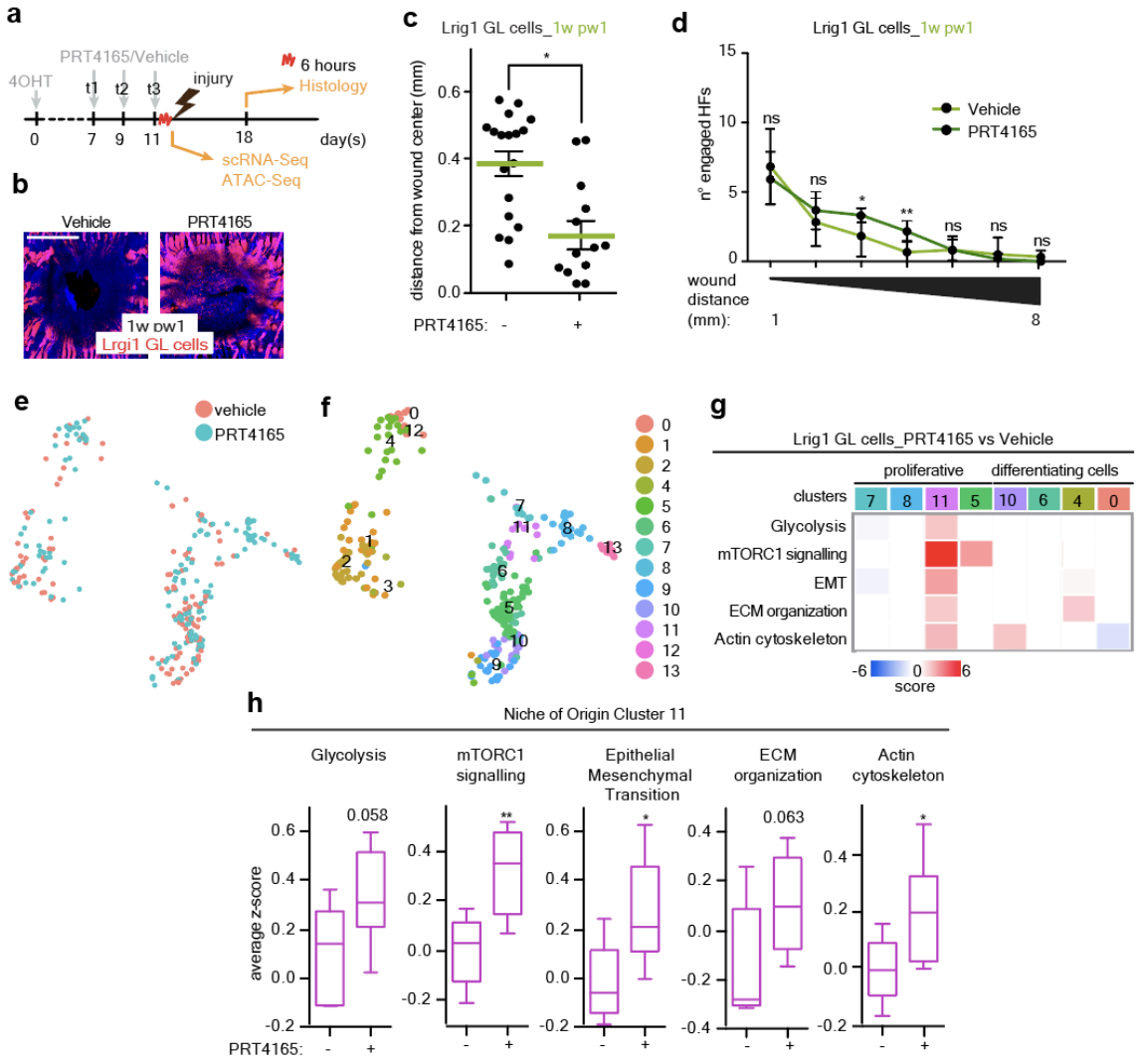

Figure 8.2. PRT4165 treatment transcriptionally mimics memory in Lrig1 epidermal lineage. a, Setting for PRT4165 treatment in Lrig1 GL mice: *day 0*, skin is genetically labelled; *day 7-9-11*, PRT4165/vehicle treatment every other day for 3 times; *day 11*, 6h after the last treatment we performed scRNA-seq, ATAC-seq or a full thickness injury; (day 14) at 1w pw1, histology. **b**, Epidermal whole-mount showing Lrig1 GL tdTomato^{+} cells at wound site in vehicle and PRT4165 treated samples at 1w pw1. Scale bar 1 mm. **c,** Quantification of distance from the wound center in vehicle vs PRT4165 treated skin at 1w pw1, relative to (**b**). Data are mean ± SEM. n = 13-18 wounds. **d**, Number of engaged HFs at 1w pw1 in different locations, up to 8 mm away from wound after vehicle/PRT4165 treatment. n = 6 wounds. **e**, **f**, scRNA-seq data from Lrig1 GL cells treated or not with PRT41645. UMAP of cells coloured by treatment (**e**) or cluster (**f**). **g**, Heatmap of GO terms specific to wound priming, taken from Figure 5.1c. Gene expression is shown per cluster as ratio between PRT4165 and vehicle treated cells. **h**, Whisker plots of the average expression for each GO term enriched in Lrig1 GL single cells. Data are median with 25th and 75th percentiles. P-value (P): ** 0.001 to 0.01, * 0.01 to 0.05, ns ≥ 0.05. Data are mean ± SD, if not differently indicated.

Physiological wound priming occurs through a chromatin opening in 1665 memory genomic loci (Figure 7b). To assess whether PRC1i can also trigger a similar chromatin remodelling to wound, we performed ATAC-seq analysis of PRC1i treated vs vehicle-treated (control) upper-HF Lrig1 GL sorted cells (Figure 8.3a-e). Strikingly, the genes associated with PRC1i-specific chromatin opening are significantly consistent with the ones associated with the 1665 memory peaks (Figure 8.3d) and they belong to the same GO categories (Figure 8.3e). Therefore, we conclude that the PRC1i was able to mimic wound effect not only at the transcriptional, but also at the chromatin level.

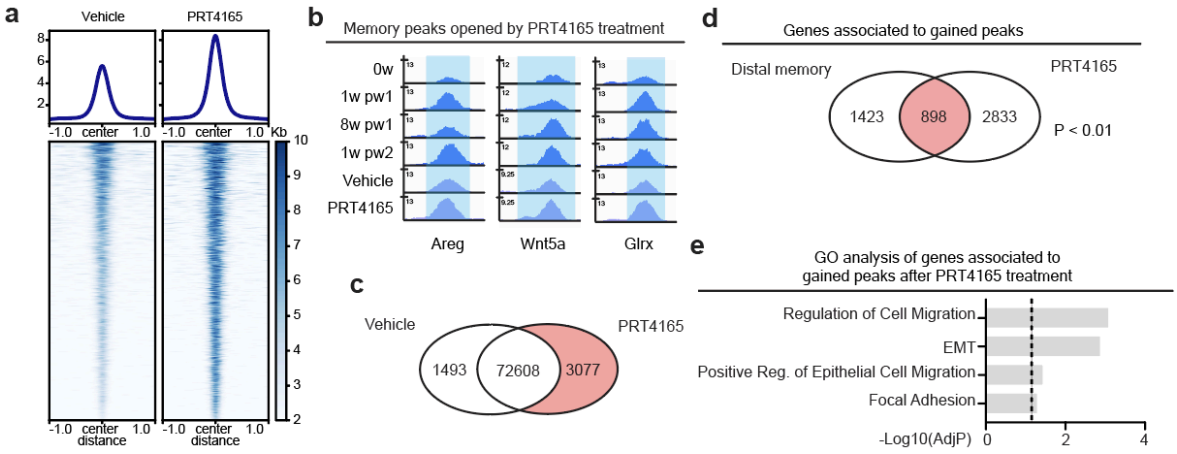

Figure 8.3. PRC1 inhibition induces the chromatin state of wound priming. a-e, ATAC-seq of sorted Lrig1 GL upper HF cells (Sca-1$^+$) from PRT4165 and vehicle treated skin. **a**, Density plots of ATAC-seq signals ± 1 kb of gained peaks (logFC > 0.5, P < 0.05) in PRT4165 vs vehicle-treated skins (up) and heatmap of the signal score of individual peaks. **b**, Snapshots of representative genomic loci gained after PRT4165 treatment and distal memory peaks. **c**, Venn diagram of ATAC-seq peaks in PRT4165-treated mice versus vehicle (numbers indicated on diagram) with gained peaks highlighted in red. **d**, Venn diagram showing the overlap between the genes associated with gained peaks in PRT4165-treated (to vehicle) and distal memory peaks identified in Fig.5b. Shared genes are in red and random permutation is calculated (p-Value (P) < 0,01). **e**, GO analysis of genes associated with gained peaks in PRT4165- vs vehicle-treated, plotted as -log10 of adjusted p-value (AdjP). Dashed line underlines significance.

Three days post treatment, these chromatin and transcriptional changes trigger Lrig1 SC progeny to move from the JZ niche into INFU toward IFE (Figure 8.4a,b), through a cell mechanism that involves enhanced migration (Figure 8.4c). Similarly to wound primed cells, PRC1i-treated Lrig1 GL cells reside, three days post treatment, in the INFU and they are more elongated (Figure 8.4d) and express more Glut1 (Figure 8.4e) with respect to vehicle-treated, even if, in the absence of a lesion, Krt6 activation signal is not present (Figure 8.4f).

Conversely to Lrig1 GL cells, PRC1i treatment to Lgr5 or Gata6 GL skin does not lead to either distal HFs engagement or enhanced wound closure compared to the untreated counterpart (Figure 8.4g,h). However, Lgr5 GL cells 3 days after the last PRC1i treatment only exit their niche of origin towards the upper bulge (Figure 8.4i), in accordance with previous observations[51].

In conclusion, H2AK119ub in the INFU decreases physiologically after the first injury and the original level is not re-established at 8w pw1 new homeostasis, following the distal spatial distribution of priming. The physiological reduction of H2AK119ub is functional to memory onset, mediating chromatin remodelling and leading to the de-repression of primed genes in distal memory cells derived from Lrig1^{+} SCs.

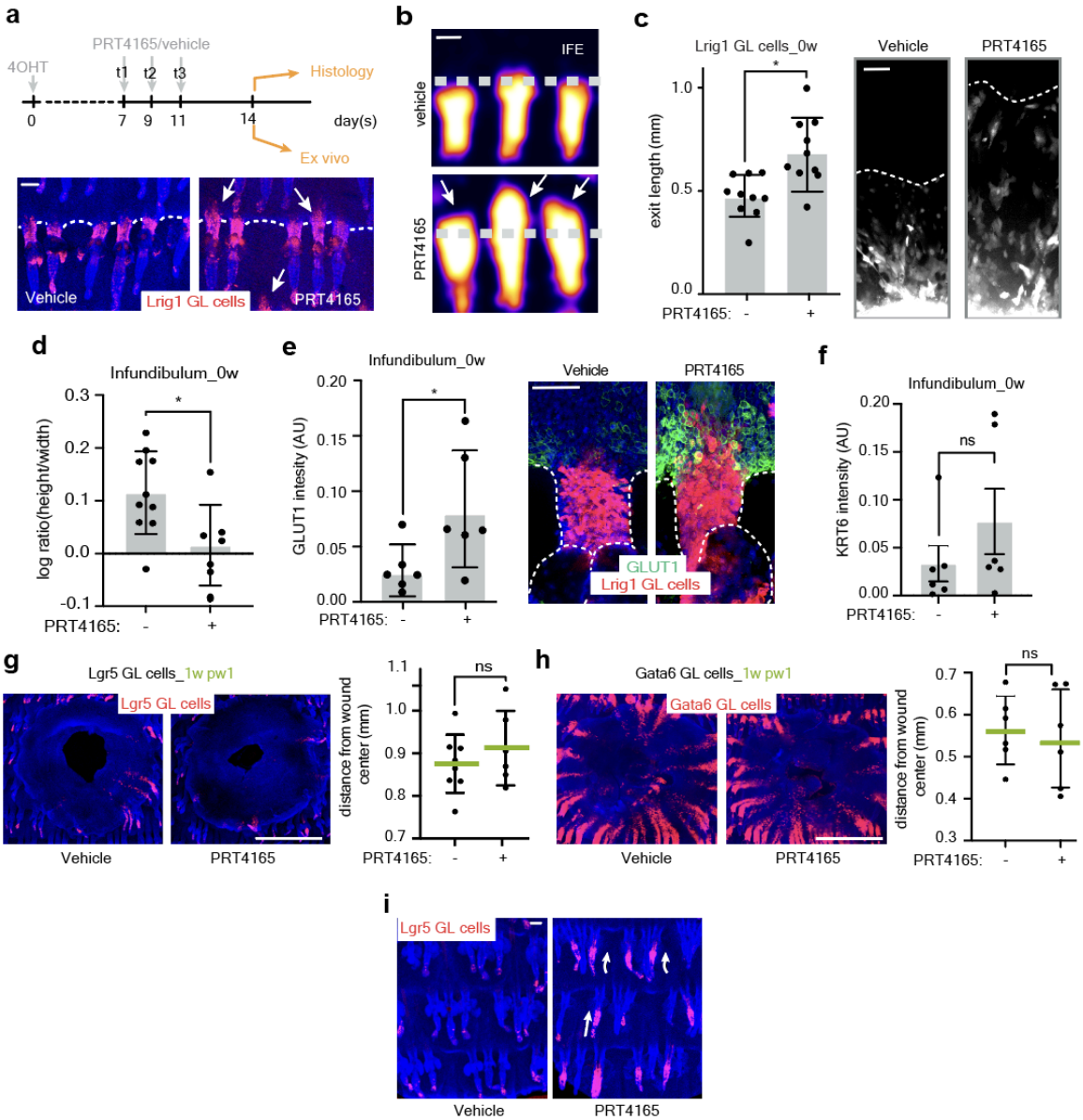

Figure 8.4. PRT4165 treatment reproduces memory-associated phenotypes specifically in Lrig1 GL cells. a, Upper panel: Setting for PRT4165 treatment in Lrig1 GL mice: *day 0*, skin is genetically labelled; *day 7-9-11*, PRT4165/vehicle treatment every other day for 3 times; *day 14*, tissue collection for histology or ex vivo assay. Lower panel: confocal pictures at day 14 of Lrig1 GL tdTomato$^+$ cells, showing Lrig1 GL HF exit upon PRT4165 topical application. **b**, 3D surface plot of Lrig1 GL cells with vehicle and PRT4165 treatment. Dashed line represents the IFE-HF boundary. **c**, Quantification (left) and representative pictures (right) of *ex vivo* migration assay on vehicle- and PRT4165-treated Lrig1 GL cells. n = 10 explants. **d**, Cell shape is reported as ratio between height and width. n = 7-10 wounds. **e**, GLUT1 is quantified (left) in INFU from whole-mount staining (right) of vehicle- and PRT4165-treated epidermis. n = 6 mice. **g**, **h**, Epidermal whole-mount showing GL tdTomato$^+$ cells at wound site (left) and quantification of distance from the wound centre (right) in vehicle vs PRT4165 treated skin at 1w pw1 in Lgr5 (**g**) or Gata6 (**h**) GL epidermis. n = 6-8 mice. **i**, Confocal images of epidermal whole-mount from Lgr5 or Gata6 GL skin treated with PRT4165 or vehicle. P-value (P): * 0.01 to 0.05, ns ≥ 0.05. Data are mean ± SD, if not differently indicated. Scale bars 50 μm **(a**, **b**, **c**, **e**, **i)**; 1 mm (**g**, **h**).

CHAPTER 5

Injury-directed priming predisposes to tumorigenesis

Results IV

5.1 Memory is long-term maintained

It has been shown that in epidermal cells wound memory can last up to 180 days[25]. To evaluate how long the wound-distal primed cells are preserved during ageing, we analysed the epidermis of 1.5-year-old Lrig1 GL mice, 10 months after the first injury is induced. The second healing process on the previously injured skin was compared to a first wound repair in age matched mice, following the scheme represented in Figure 9.1a. A closure advantage at 1w pw2(40) with respect to 1w pw1(40), is evident (Figure 9.1b,c). Importantly, even in the aged skin settings, wound distal Lrig1 GL cells show both the HF engagement phenotype (Figure 9.1d) and an *ex vivo* enhanced migratory ability when compared to the untrained counterpart (Figure 9.1e), suggesting that distal memory cells are maintained in long-term.

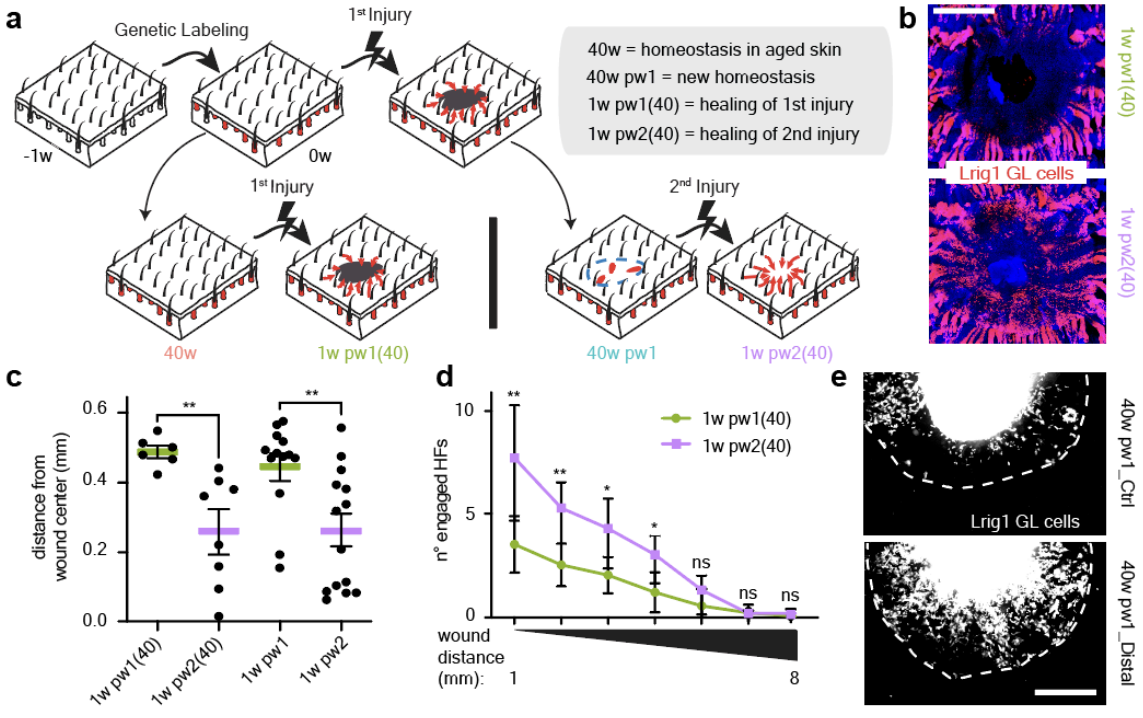

Figure 9.1. Priming-associated cell state is long-term maintained in infundibular Lrig1 GL progeny. **a**, Settings to evaluate long term priming in Lrig1 GL skin: (-1w) genetic labelling; (0w) wounded and unwounded mice; 40 weeks after labelling, full thickness biopsy on both unwounded (40w) and wounded (40w pw1) mice; 1 week after wound samples are collected, 1w pw1(40) or 1w pw2(40). **b**, **c**, Epidermal whole-mount showing Lrig1 GL tdTomato$^+$ cells at wound site at 1w pw1(40) and 1w pw2(40) time points (**b**) and quantification of distance from the wound center (**c**). Results are compared to young samples at the same time points. n = 6-14 wounds. **d**, Number of the engaged HFs at 1w pw1(40) and 1w pw2(40) from 1 to 8 mm from wound edge. n = 6-7 wounds. **e**, *Ex vivo* migration assay. Stereomicroscope images of Lrig1 GL tdTomato$^+$ cells migration from skin explants collected from Distal or in Ctrl HFs. P-value (P): ** 0.001 to 0.01, * 0.01 to 0.05, ns ≥ 0.05. Data are mean ± SD, if not differently indicated. Scale bars 1 mm **(b**, **e)**.

To confirm this, we performed scRNA-seq of homeostatic skin of old mice (40w) and we compared it to the new homeostasis at 40w pw1 (Figure 9.2a,b). Strikingly, ~1 year after injury (40w pw1) the infundibular primed cells are well maintained in the *Transition Cluster* (Figure 9.2a). Additionally, the GO terms enriched in the *Transition Cluster* in young 8w pw1 still follow an overexpression trend ~1 year after wound when compared to the aged match unwounded (Figure 9.2c). To validate the long-term maintenance of distal priming, we performed whole-mount histological analysis.

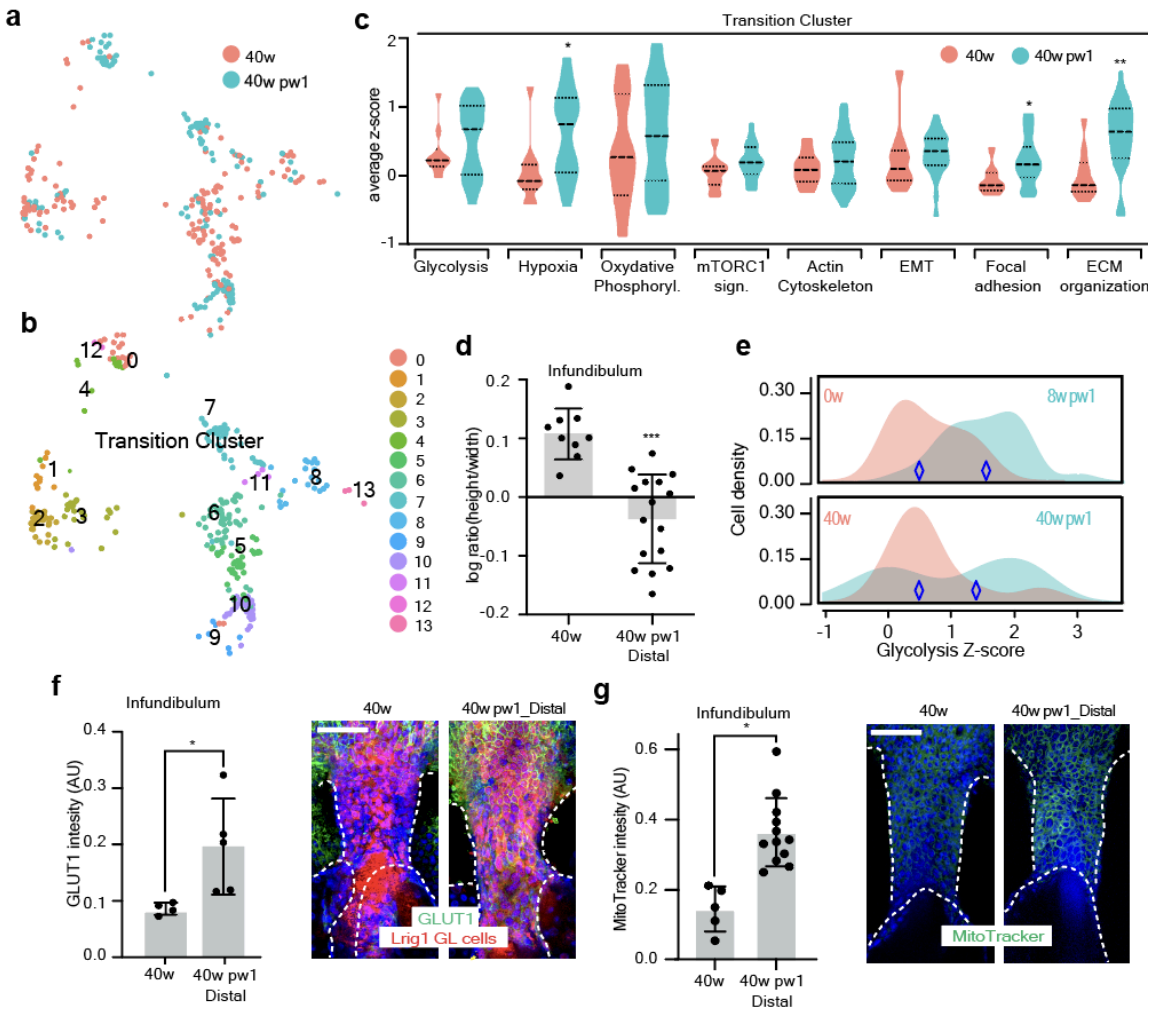

Figure 9.2 Transcriptional priming is preserved in ageing. a, b, s scRNA-seq of Lrig1 GL cells at the two aged homeostasis: 40w and 40w pw1 time points. UMAP of cells coloured by time points (**a**) or clusters (**b**). **c**, Violin plot of the average expression for each GO term enriched in young samples comparing 40w and 40w pw1. **d**, Quantification of cell shape in INFU from epidermal whole-mount staining at 40w and at 40w pw1 in distal memory areas (Distal- 3 to 7 mm from wound site) in Lrig1 GL cells. Cell shape is reported as ratio between height and width (n = 9-16 wounds). **l**, Density plot for glycolysis gene signature in Lrig1 GL cells from *Transition Cluster* comparing the two old (40w and 40w pw1) and two young (0w and 8w pw1) homeostasis. **m**, GLUT1 levels are quantified (left) in the INFU from epidermal whole-mount staining (right) at 40w and at 40w pw1 in distal memory areas. GLUT1 is stained in n = 4-5 wounds. **g**, MitoTracker levels in the INFU from epidermal whole-mount staining at 40w or 40w pw1_Distal (5 mm from wound site). n = 5-12 wounds. P-value (P): *** 0.0001 to 0.001, ** 0.001 to 0.01, * 0.01 to 0.05, ns ≥ 0.05. Data are mean ± SD, if not differently indicated. Scale bars 50 μm (**f**, **g**).

Comparing the homeostatic cells at 8w pw1 located millimetres away from the injury with the homeostatic INFU cells at 0w, we still observe cell elongation and increased Glut1 and Mitotraker (Figure 9.2d-g).

Thus, we demonstrate that the wound memory is largely stable, functional and maintained by wound-distal primed progenitors that are preserved in aged skin for a remarkably long-time frame.

5.2 Epithelial priming promotes tumour onset with a spatial gradient

Wound memory has a beneficial impact on long-term tissue fitness related to skin repair (Figure 9.1 and Figure 9.2). However, since wound healing and cancer share many hallmarks[52], and the epigenetic landscape of cell-of-origin can define epidermal tumour subtypes with differential EMT-features[37], we hypothesised that *wound priming* might impact on ageing associated diseases such as tumorigenesis, in line with recent observations in the context of pancreatic cancer[53,54]. In addition, as *wound priming* has a long-range spatial distribution, the detrimental effect might follow this spatial trend, building on the epigenetic field cancerization phenomenon that predisposes to tumour onset[33,35].

Importantly, while tissue thickening is a consequence of acute UVB-treatment in both 8w pw1 and 0w homeostatic conditions (Figure 10.1a,b), the engagement of Lrig1 GL cells in IFE is specific to UVB-treated cells at 8w pw1 (Figure 10.1c,d), suggesting that the memory of an antecedent lesion exacerbates the Lrig1 GL cells response to an oncogenic stimulus, potentially triggering cancer.

To verify these hypotheses, we induced carcinomas formation in mice through chronic UVB treatment (Tumorigenic Stimuli; TS), a physiological oncogenic stress for skin pathology[55] as in the scheme in Figure 10.1e. This protocol allowed us to bypass the papilloma formation step, typical of the chemical induced carcinogenesis in murine skin but absent in human skin tumorigenesis[56]. The comparison between wounded and treated (Wounded; Wd, Wd&TS) and treated-only mice (TS) during chronic UVB-treatment reveals the onset of epidermal dysplasia, typical of actinic keratosis or early Squamous Cell Carcinoma in situ (eSCC)[57] specifically in Wd&TS mice tail skin (Figure 10.1f-h). eSCCs derive mainly from Lrig1 GL primed cells (Extended Data Fig.12h). Strikingly, in clear parallelism with the spatial distribution of primed Lrig1 GL cells described in the above paragraphs, eSCCs are distributed following a long-range spatial gradient from wound edge (Figure 10.1f).

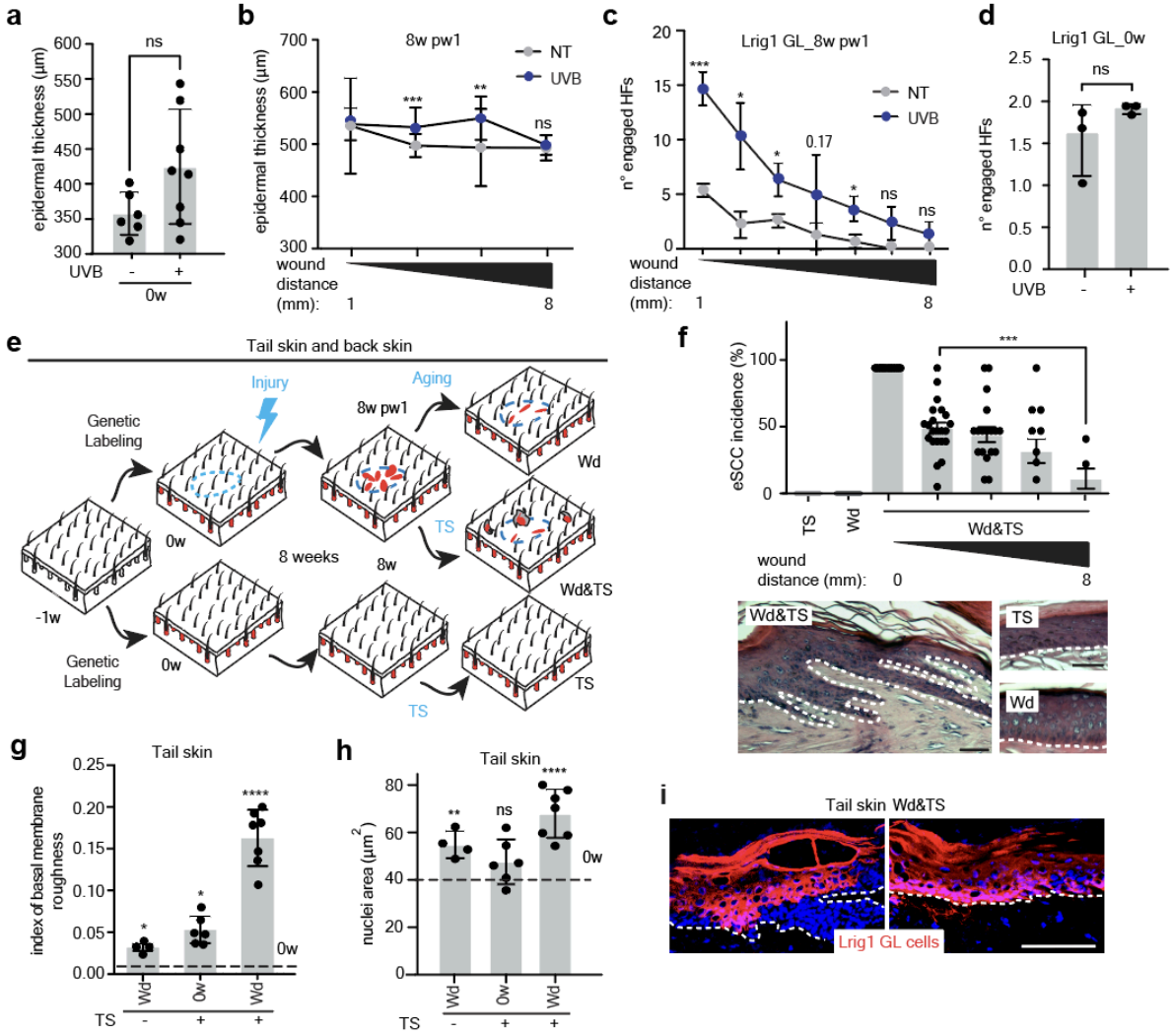

Figure 10.1. Healed wound in tail skin predisposes to pre-tumoral lesions. a, b, Effect of acute UVB irradiation on epidermal thickening at 0w (**a**) or 8w pw1 where different distances from wound site are

considered (**b**). NT= not treated. n = 4-11 mice. **c, d,** Effect of acute UVB irradiation on the number of engaged HF at 8w pw1, at different wound distances (**c**) or at 0w (**d**). n = 3 mice. **e,** Scheme of tumorigenesis protocol in Lrig1 GL mice: (-1w) genetic labelling; (0w) injury or not; (8w) 8w weeks after, tumorigenic stimuli (TS) started (tail or back skin). Samples are wounded only (Wd), wounded with TS (Wd&TS) or just treated with TS (TS). **f**, Early SCC (eSCC) onset in tail skin of UVB treated mice with a previously healed wound (Wd&TS) or unwounded (TS), used as control as in schematics in Extended Data Fig.12e. Incidence (**up**) and representative H&E (**down**) of eSCC is quantified in the indicated samples in a distance dependent manner from wound. Data are mean ± SEM. n = 5–22 mice. **g**, **h**, Characterization of early SCC phenotype in tail skin. Quantification of membrane roughness (**g**) or nuclei area (**h**) in Wd, TS and Wd&TS. n = 4 Wd, n = 6 TS, n = 4-9 Wd&TS. (**i**) eSCC from Wd&TS mice are mostly composed by Lrig1 GL cells. Scale bar 100 μm. P-value (P): **** < 0.0001, *** 0.0001 to 0.001, ** 0.001 to 0.01, * 0.01 to 0.05, ns ≥ 0.05. Data are mean ± SD, if not differently indicated.

In this precancerous context, we also observe a spatial distribution of the anti-correlation of H2AK119ub and γ-H2A.X, as a marker of DNA damage[58]. Indeed, the accumulation of DNA damage is found where H2AK119ub is reduced, including the distal memory area (Figure 10.2a). This scenario is reminiscent of a field cancerization (also termed as field change or cancer field effect) phenomenon in which wide areas of cells in a tissue are affected by carcinogenic alterations both genetic and epigenetic[33,35]. To gain more epigenetic insights, in particular to verify if the epigenetic field effect is linked to priming, we performed ATAC-seq of Lrig1 GL cells, upon chronic UVB irradiation, in presence or absence of wound-distal priming (Figure 10.2b-f). Consistently with the chromatin landscape of the physiological priming at 8w pw1 (Figure 7), the global chromatin opening of Lrig1 GL cells resident in wound distal in comparison to control areas (non-memory) is preserved even upon chronic irradiation (Figure 10.2b-d), as consequence of the loss of a repressive marker, such as H2AK119ub (Figure 8.1f,g and Figure 10.2a). Strikingly, genes associated to the gained peaks in UVB-treated distal memory areas are significantly consistent with the memory ones (associated to the 1665 memory peaks) and they belong to the same GO categories (Figure 10.2f). Overall, these data indicate the existence of an epigenetic field cancerization event that is established after wound in distal memory areas, consequently to H2AK119ub reduction and wound priming, and maintained during the pre-cancerous stages.

To further investigate on the link of the epigenetic field effect, founded by wound priming, and the formation of fully developed SCCs we addressed tumours formation in back skin, where more severe lesions were expected, as back skin is less resistant to tumorigenesis than tail skin[59].

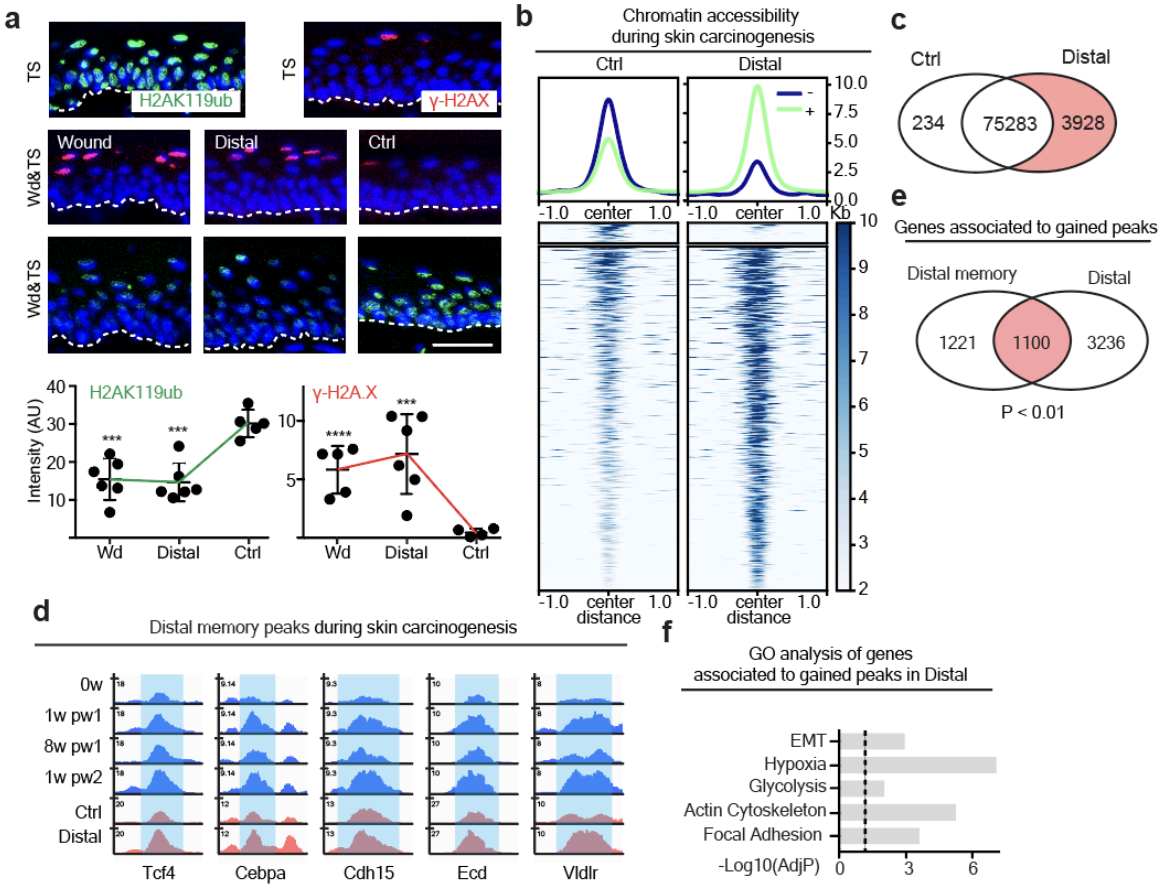

Figure 10.2. Wound priming initiates field cancerization. a, Images (**up**) and quantification (**down**) of H2AK119ub and γ-H2A.X (DNA damage marker[58]) gradients in wound bed (Wb), distal memory areas (Distal- 3 to 7 mm from Wb) and far control (Ctrl- > 2 cm from Wb) in Wd&TS mice. n= 4-6 Wd&TS. **b-f**, ATAC-seq of sorted Lrig1 GL upper HF cells (Sca-1$^+$), under chronic UVB treatment from distal memory area (Distal- 3 to 7 mm from Wb) and control (Ctrl- unwounded area) are shown. Scale bars 50 μm. **b**, Density plots depict ATAC-seq signals ± 1 kb of deregulated peaks (logFC > 0.5, P < 0.05) in Distal vs Ctrl (up) and heatmap of the signal score of individual peaks (down)**. c**, Venn diagram of peaks in Distal vs Ctrl (numbers indicated on diagram). Gained peaks are highlighted in red. **d**, Snapshots of genomic loci associated with primed genes that remain accessible in distal memory area**. e**, Venn diagram showing the overlap between the genes associated with gained peaks during skin carcinogenesis in Distal (respect to Ctrl) and Distal memory peaks from Fig.5b. Shared genes are highlighted in red and random permutation is calculated (p-Value (P) < 0,01). **f**, GO analysis of genes associated with gained peaks in Distal vs Ctrl, measured as -log10 of p-Value (P). Dashed line underlines significance. P-value (P): **** < 0.0001, *** 0.0001 to 0.001. Data are mean ± SD, if not differently indicated.

Consistently with eSCC incidence in tail, Wd&TS back skins show a greater number of cutaneous SCCs compared to TS controls (Figure 10.3a,b) with an increased number of metastatic tumours (Figure 10.3c). In addition, the severity grade of the lesions (Figure 10.3d-f), as well as the

percentage of Lrig1 lineage-derived cells within the tumour mass (Figure 10.3h) are increased in Wd&TS. Remarkably, all these phenotypes have a gradient spatial distribution that overlaps with the location of wound-distal primed cells and H2AK119ub loss (Figure 10.3i).

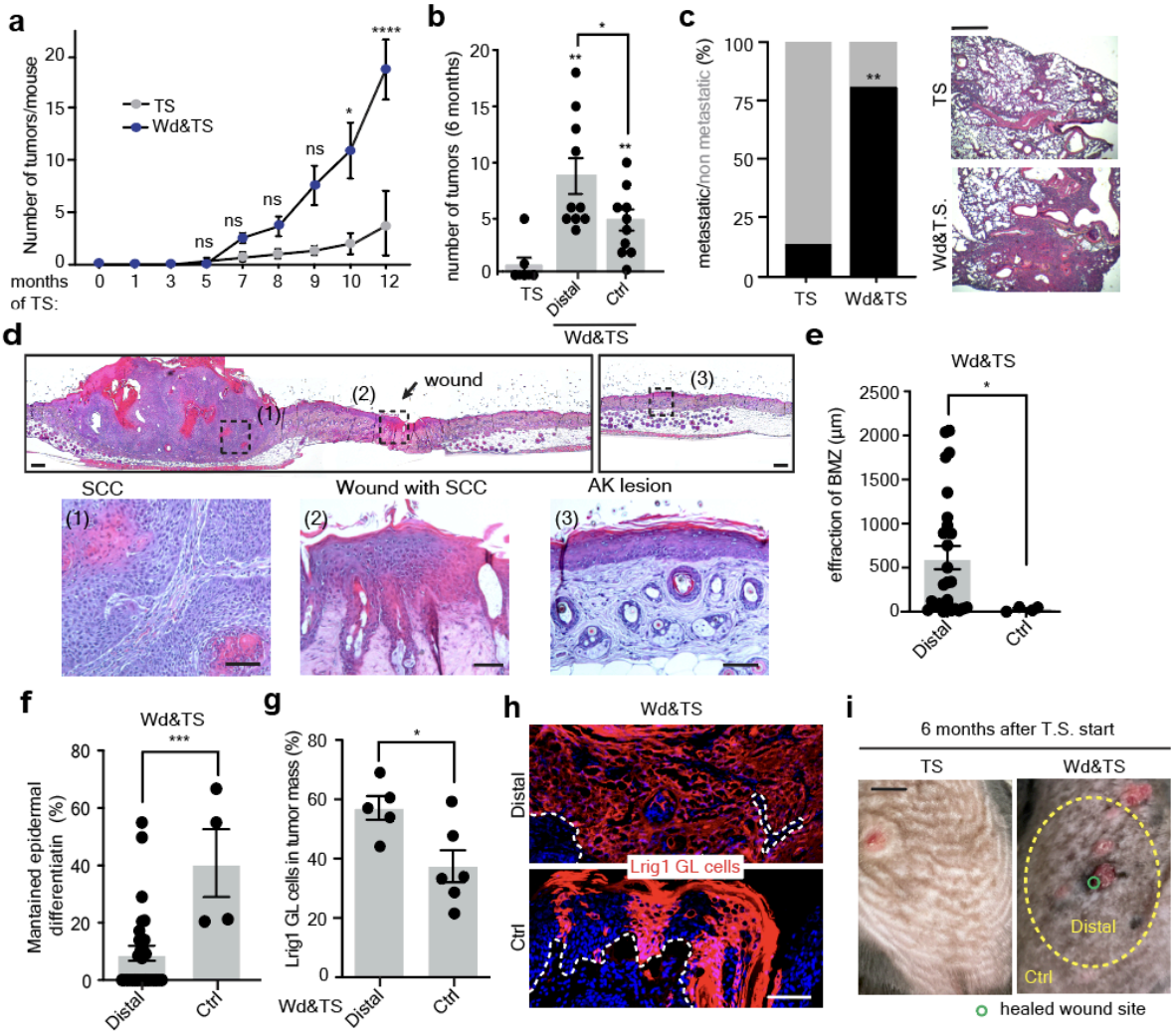

Figure 10.3. Pre-injured back skin is prone to SCCs onset. a, Number of newly formed tumours in the back skin of UVB treated mice with a previously healed wound (Wd&TS) or unwounded (TS, used as controls), shown as a time course. n = 3 TS, n = 9 Wd&TS. Statistics: 2-way ANOVA. **b**, Number of tumours at 6 months after tumour stimuli induction in the indicated conditions as in Extended Data Fig.12e. n = 7 TS, n = 10 Wd&TS. **c**, Presence of lung metastasis is assessed by histology in TS vs Wd&TS. Plot of percentage of metastatic vs not metastatic mice. n = 6 TS, n = 8 Wd&TS. Statistics: Chi-square test (**left**). H&E staining of lung metastasis derived from back skin primary tumours (**right**). **d**, Representative tiling (**up**) and magnification (**down**) of some selected zones (down), stained with H&E. AK = Actinic keratosis. **e-h**, Characterization of tumours developed in Distal or Ctrl zones. Effraction of the basal membrane zone (BMZ) informative for tumour invasiveness. Statistics: Mann-Whitney t-test. n = 4 Ctrl, n = 27 Distal tumours (**e**); percentage of maintained epidermal differentiation over the total tumour area. n = 4 Ctrl, n = 30 Distal tumours (**f**). Percentage (**g**) and representative pictures (**h**) of Lrig1 GL cells within the tumour mass. n = 5 Ctrl, n = 6 Distal tumours. **i**, Representative macroscopic images of the back skin from pre-wounded or control mice. Yellow dashed circles

delimit a zone of ~1 cm ray around the wound (Distal) that displays memory, while outside is control zone (Ctrl) without wound memory. Scale bar 50 mm. P-value (P): **** < 0.0001, *** 0.0001 to 0.001, ** 0.001 to 0.01, * 0.01 to 0.05, ns ≥ 0.05. Data are mean ± SD, if not differently indicated. Scale bars 300 μm (**c**, **d**, **h**).

The level of H2AK119ub, whose reduction was functional in distal memory establishment, is lower in SCCs that develop with the contribution of wound-educated Lrig1 GL cells in comparison to tumours that developed in not wounded skin (Figure 10.4a) and negatively correlates with the overexpression of the priming marker Glut1 (Figure 10.4b). Moreover, the treatment with PRC1i, which we demonstrated to recapitulate at transcriptional and chromatin level several features of wound priming (Figure 8.2), accelerates DNA damage accumulation and tumour onset in hairless mice (Figure 10.4c-d), thus recapitulating the physiological anticorrelation between DNA damage and H2AK119ub loss observed in the context of UVB-treated skin (Figure 10.2a). Overall, long term *wound priming* promotes skin tumorigenesis following its spatial gradient distribution, in accordance with the wound-induced epigenetic field effect scenario.

Finally, we evaluated the relevance of our findings in the human SCC context, comparing cutaneous SCCs of different causal origins. We focused on Epidermolysis Bullosa derived SCCs (EB-SCCs) and SCCs from psoriatic skin (Pso-SCCs), since these patients have higher risk of tumorigenesis, possibly through a mechanism that involves respectively wound and inflammatory memory[60,61]. As control we employed SCCs derived from simple UV exposure during life (UV-SCCs). Consistently with our murine observations, Pso-SCCs and EB-SCCs, have a decreased H2AK119ub when compared to UV-SCCs that is associated once again to an enhanced Glut1 expression (Figure 10.4e,f), pointing out a memory-tumorigenesis link in humans.

All together, we showed that *wound priming* is maintained, even in the event of a chronic cancerous stimulus, through an open chromatin state lead by H2AK119ub reduction and distributed in a wide area around the antecedent injury. This epigenetic field effect has long-term detrimental consequences on epidermal fitness, enhancing the incidence of squamous cell carcinomas.

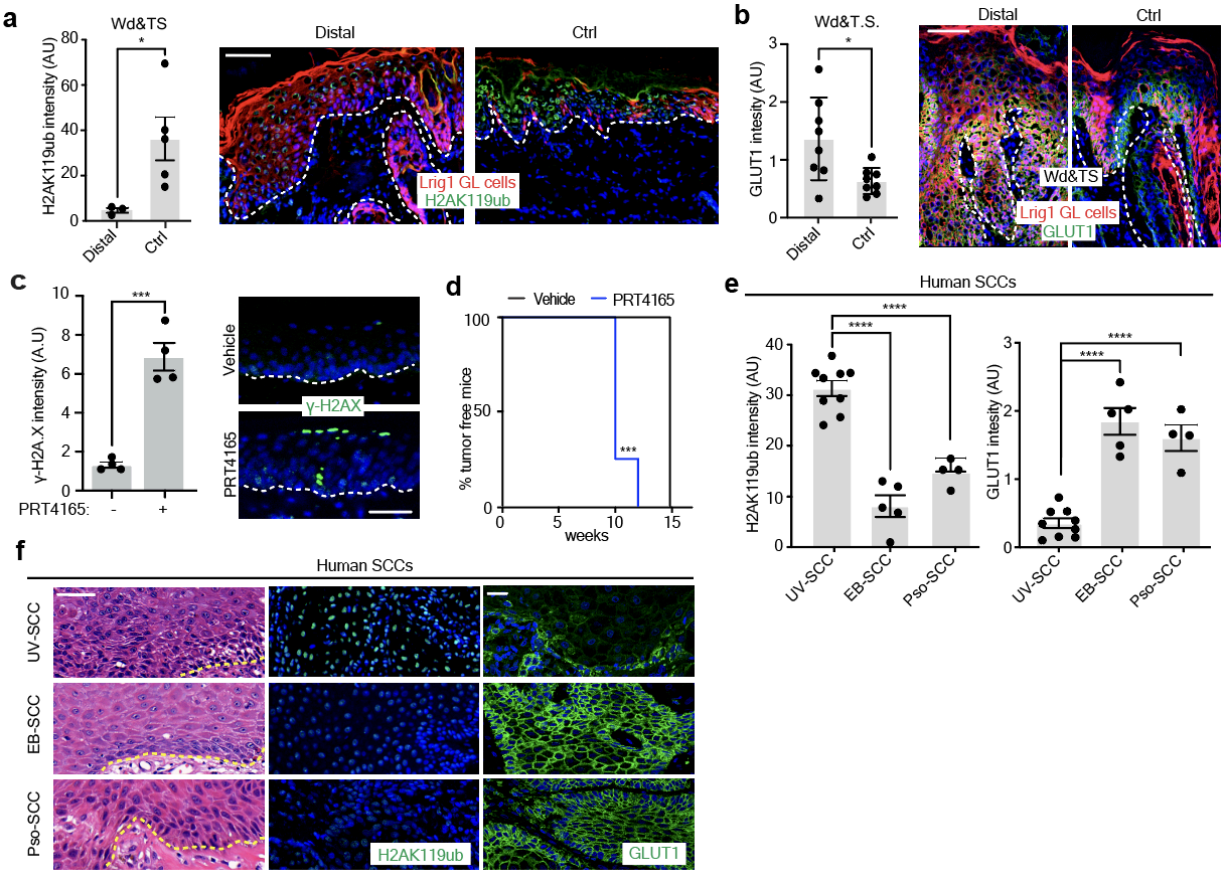

Figure 10.4. Glut1 overexpression and H2AK119Ub reduction are characteristics of wound-derived SCCs in humans. a, H2AK119ub levels in Wd&TS skin sections from Distal or Ctrl area. Quantification (left) and pictures (right) are shown. n = 3 Ctrl, 5 Distal tumours. **b**, GLUT1 expression in skin section from Distal or Ctrl area of Wd&TS samples. Representative pictures and quantification are shown. n = 8 Wd&TS. **c**, Quantification (left) and representative pictures (right) of H2A.X (DNA damage marker) staining in hairless mice skin treated with PRT4165 or vehicle. n = 4 for vehicle- and PRT4165-treated mice. **d**, Tumour incidence on hairless mice treated with PRT4165. n = 7 vehicle-, n = 4 PRT4165-treated mice. Statistic: Mantel-Cox test. **e**, **f**, H2AK119ub and Glut1 staining on human samples: Epidermolysis Bullosa derived SCCs (EB-SCCs), and SCCs from psoriatic skin (Pso-SCCs) and SCCs derived from simple UV exposure during life (UV-SCCs) as control. Quantification (**e**) and representative pictures (**f**) are shown. P-value (P): **** < 0.0001, *** 0.0001 to 0.001, ** 0.001 to 0.01, * 0.01 to 0.05, ns ≥ 0.05. Data are mean ± SD, if not differently indicated. Scale bars 50 µm (**a**, **b**, **c**, **f**).

CHAPTER 6

Discussion

6.1 Trained memory versus priming in epithelial cells

Cell adaptation allows cells to modify their behavior in response to environmental stimuli. Innate immune cells adapt to a stressful event, keep an epigenetic memory of it and respond faster to a second assault through different adaptation programs such as *trained immunity* and *priming*[22,62,63]. The spectrum of epithelial cell responses and their adaptation mechanisms to a stressful event has just started to be understood. However, emerging evidence highlights the existence of such a variety of adaptations in epithelial cells, following both inflammation and tissue damage. *Trained wound-memory* has been reported: HFSCs while repairing an injury, acquire transcriptionally dormant epigenetic memory that can be quickly reactivated upon a subsequent stimulus[25]. Lineage tracing of multiple epithelial lineages combined with scRNA-seq over two consecutive skin injuries allowed us to understand the heterogeneity of adaptive programs other than trained memory. We demonstrated that both $Lgr5^+$ and $Lrig1^+$ HFSCs acquire wound memory in their respective niche, with different transcriptional programs. However, primed cells are generated only within the Lrig1 progeny during the healing and are maintained in the newly established homeostasis. Strikingly, the transcriptional profile of Lrig1 GL memory cells, intermediate between repairing and homeostatic cells, is a classical feature of *priming* which has not been seen before in an epithelial context.

6.2 Wide distribution of wound priming in undamaged areas

Epithelial SCs receive cues from their local microenvironment as well as from infiltrating immune cells, circulating factors and mechanical forces that direct inflammatory responses and wound repair[64]. Since these secondary effectors are known to have spatially wide effect, the spatial extent of memory is a crucial aspect that has only recently begun to be deciphered. In the case of inflammatory memory caused by the treatment of skin with chemicals, epidermal memory seems

locally restricted to the inflamed areas[24]. On the other end, a localized tissue damage is able to elicit an unexpected spatially wide response in epidermal cells, that we named *distal memory*, with a tissue-scale impact on the skin[65]. Importantly, the spatial extent of wound memory has not previously been assessed due to the absence of an identifiable cell state. In particular, wound-primed progenitors derived from Lrig1 SCs, with the memory cell state that we described above, are present up to ~ 7 mm away from the injury margins[65]. Since the skin is the largest organ in mammals this spatially large adaptation involves tissue at sub-organ scale. However, in other smaller epithelia it is likely that this memory might impact the whole organ.

6.3 Transcriptional de-repression and cell state of wound-primed progenitors

Several transcription factors are functional determinants in inflammatory memory[23] however the epigenetic regulators have not been identified. Here we demonstrate that wound distal priming of Lrig1 GL cells relies on a chromatin opening led by the reduction of a transcriptional repressive histone mark. In particular, we observed a clear correlation between the spatial distribution of decreased levels of H2AK119ub in the INFU after wound and the wide location of the *wound priming* for up to ~ 7 mm from the injury. Since PRC1 inhibition leads to acquisition of some enhanced repair skills and to the transcriptional de-repression of several gene sets typical of *wound priming* in Lrig1 but not in the Lgr5 progeny, we concluded that the reduction of H2AK119ub functionally contributes to priming only in a specific cell identity context. This, together with the observation that the upper HF is characterised by a low level of H2AK119ub even in homeostatic conditions, conferred to the Lrig1$^+$ SCs a new repair-specific role. Thus, it is easy to speculate that specific cells in other epithelia might also have this unique innate potential.

mTOR and HIF1α-mediated glycolysis has been identified as the metabolic basis for both epidermal response to wound healing[66] and *trained immunity* in monocytes [67]. Interestingly, the cell state of the identified wound-primed cells in the infundibulum is characterised by similar features and enhanced migratory abilities. Since we recapitulated this cell state through PRC1 inhibition, we established a direct causal link between the identified epigenetic, transcriptional and metabolic state. Because of all the above-mentioned similarities between the adaptation programs of epithelial and

innate immune cells, it is likely that the reduction of H2AK119ub that we identify in epithelial cell priming might be functional in the immune system context.

6.4 Long-term priming lays the foundation for field cancerization

In immune cells, over time, these adaptations shape an individual identity, increasing the fitness of organisms against pathogens. Besides the positive effect, adaptations can be maladaptive and predispose to irreversible pathologies[22,29]. Thus, the study of the durability and the reversibility of memory in immune e non-immune cells is crucial to understand the physiological to pathological transition. While short-lasting memories have been reported for many immune subtypes, epithelial SCs, due to their longevity, display in general long-lasting memories. In skin, SCs with trained immunity-like adaptation have been observed until 180 days after inflammation[24], while primed SCs last even longer, 40 weeks after skin injury[65]. Similar timing has been described in pancreas, where memory epithelial cells retain chromatin and transcriptional activation till 18 weeks after inflammation[54], and intestine, where memory lasts for 6 weeks, at least[68]. Those long-lasting memories are beneficial in terms of protection to subsequent inflammation or damage[24,54,65,68]. However, prolonged chronic exposure to those stimuli reverts the benign effects of memory into detrimental. Priming is crucial to protect pancreas from damage but push the malignant transformation in presence of oncogenic KRAS[54]; in intestine trained immunity-like mechanisms offers protection from subsequent gut infections while mediating an increased inflammation in the context of colitis[68]; in skin, we demonstrated that, although cell priming increases tissue repairing abilities, it increases the incidence of SCCs formation in UV-exposed epidermis, establishing an epigenetic field cancerization[65].

Carcinogenic alterations that lead to field cancerization can be both genetic and epigenetic[33,35]. While is often difficult to understand which comes first, our data highlight a sequential order in which epigenetic alterations such as a reduction of H2AK119ub, and its chromatin consequence, a chromatin opening of specific loci sets, are the initiators of field cancerization prior to genetic alterations. The epigenetic field change that characterises the new homeostasis changes the tissue features overtime, predisposing to tumour onset. Indeed, beside the positive effect of wound memory on tissue repair fitness, we demonstrate that skin tumorigenesis is favoured by the presence

of a previous completely resolved injury and that Lrig1 GL progeny has a major contribution within the tumour mass. Strikingly, the correlation between the spatial distribution of primed cells and the tumour onset corroborates the link between wound distal memory and epigenetic field cancerization. Mechanistically, our data support the hypothesis that the reduction of H2AK119ub, a functional feature of *wound priming*, directly promotes tumorigenesis. On this line, wound memory associated with tumours have reduced H2AK119ub levels in comparison to control tumours, not only in mice but also in humans. Our results together with recent findings in diversified cellular contexts[69,70], supported the general conclusion that loss of a key histone repressive mark promotes tumorigenesis. This raises a general concern with respect to the therapeutic intervention on repressive chromatin factors that could be beneficial in regenerative medicine but detrimental in oncology.

CHAPTER 7

Materials and Methods

7.1 Mouse procedures

7.1.1 Mouse strains. Maintenance, care and experimental procedures have been approved by the Italian Ministry of Health, in accordance with Italian legislation, and the institutional review board of the Hokkaido University Graduate School of Medicine. Rosa26-fl/STOP/fl-tdTomato, Lgr5-EGFP-ires-CreERT2, Gata6-EGFP-ires-CreERT2 and Lrig1-EGFP-ires-CreERT2 have been previously described[11,13,14,71]. For tumorigenesis, SKH-1 hairless mice have been purchased from Charles-River Laboratories. Hairless mice were maintained in specific pathogen free conditions; the other mice were kept in conventional conditions with 12hr light dark cycles from 8 am to 8 pm. The study is compliant with all relevant ethical regulations regarding animal research.

7.1.2 Lineage tracing of hair follicle lineages. Lgr5-EGFP-ires-CreERT2, Gata6-EGFP-ires-CreERT2 or Lrig1-EGFP-ires-CreERT2 were crossed with Rosa26-fl/STOP/fl-tdTomato strain. Genetic labelling was induced in epidermis of 6-8 weeks old mice with a single topical administration of 75 µg of (Z)-4-Hydroxytamoxifen (Sigma-Aldrich) (15 mg/mL in acetone).

7.1.3 Full-thickness skin wound. 1 week post tamoxifen-treatment (0w), 7-9 weeks old mice were anesthetised with intramuscular injection of Ketamine/Xylazine (Rompun®) 30 µl/head or isoflurane inhalation. Full thickness wounds were made with a circular biopsy punch in tail (2 mm) or dorsal (5 mm) skin. For dorsal skin wounds mice were shaved with an electric clipper 24 h before the procedure.

7.2 Immunostaining and image processing

7.2.1 Epidermal and dermal whole-mount. Tail epidermal or dermal whole-mounts were prepared as previously described[14]. Briefly, the skin was incubated in PBS/EDTA (5mM) at 37 °C for

4 h and the epidermis was separated from the dermis using forceps. Epidermis and dermis were pre-fixed 1h in 4% paraformaldehyde (PFA, Sigma-Aldrich), rinsed three times with PBS for 5 min and conserved in PBS with 0.2% sodium azide at 4°C, till usage. For immunofluorescence staining, epidermis/dermis samples were permeabilized and blocked in PB buffer (0.5% skim milk, 0,25% fish gelatin and 1% of Triton X-100 in PBS) for 2 h at room temperature (RT) (for epidermis) or overnight at 4 °C (dermis). Subsequently, primary antibodies were diluted in PB buffer and incubated overnight at 4 °C. The following primary antibodies and dilutions were used: anti-Keratin 6A (rabbit, 1:200, Biolegend_905701), anti-Ubiquityl-Histone H2A (Lys119) (clone D27C4) (rabbit, 1:1000, CST_8240), anti-Ki67 (rabbit, 1:100, Abcam_16667), anti-E-cadherin (clone 24E10) (rabbit, 1:200, CST_3195), anti-mFABP5 (goat, 1:500, RD System_AF1476), anti-Glucose Transporter GLUT1 (SLC2A1) (EPR3915 clone) (rabbit, 1:200, Abcam_ab115730), Alexa-647 conjugated Phalloidin A (Thermo-Fisher). After 30 min of PBS wash, samples were incubated with secondary antibodies together with 4',6-diamidine-2-phenylindole dihydrochloride (DAPI) (Thermo-Fisher, 1ug/mL) 2 h at RT (epidermis) or overnight at 4 °C (dermis). Alexa Fluor-568-, 488-, or 647-conjugated secondary antibodies (Life Technologies) were used at 1:1000 dilution. Tissues were finally mounted using Mowiol 4-88 Reagent (Sigma-Aldrich) mounting solution.

7.2.2 MitoTracker staining. For quantification of mitochondrial activity, MitoTracker staining (MitoTracker® Deep Red FM_M22426, Thermo-Fisher) was performed in whole-mount epidermis according to datasheet instructions. Briefly, freshly isolated epidermis was incubated at 37 °C 10 min in 50 nM MitoTracker solution in low calcium DMEM (Thermo-Fisher) without serum. Samples were then washed 3 times with DMEM (20 min each) and fixed 40 min 4% PFA before mounting.

7.2.3 Immunostaining of skin sections. For frozen section, back skin or tail tumor samples were pre-fixed 20 min at RT in 4% PFA immediately after dissection, to preserve tdTomato signal. After fixation tissues were washed 30 min in PBS, embedded in OCT Compound (Bio Optica) and kept at -80 °C. Frozen tissue blocks were sectioned (5-7 µm) with a CM3050S Leica cryostat (Leica Mycrosystems). Tissues were washed three times in PBS for 5 min and incubated in PB buffer for 1 h at RT. Primary antibodies were incubated overnight at 4 °C. Sections were rinsed three times in PBS and incubated with secondary antibodies and DAPI (Thermo-Fisher, 1ug/mL) or TOPRO3

(Thermo-Fisher, 1ug/mL) in PB buffer for 1 h at RT. Sections were again washed three times with PBS. The following primary antibodies were used: anti-Ubiquityl-Histone H2A (Lys119) (clone D27C4) (rabbit, 1:1000, CST_8240), anti-Glucose Transporter GLUT1 (SLC2A1) (clone EPR3915) (rabbit, 1:200, abcam_ab115730). For paraffin embedding, freshly collected samples were closed in blocks and fixed 24 h in 10% NBF (Neutral Buffered Formalin, Sigma-Aldrich) and then transferred to 70% EtOH solution until the embedding. Samples were sectioned (5-10 µm) with a microtome (Leica Mycrosystems). After deparaffinization and hydration hematoxylin and eosin (H&E) staining or immunofluorescent staining were performed. For immunofluorescent staining, antigen unmasking was performed for 20 min at 98 °C in citrate buffer (pH 6). The sections were then blocked with PB buffer for 1 h at RT. Primary and secondary antibody incubations were performed overnight at 4°C, and 1h RT respectively, followed by 20 minutes of DAPI or TOPRO3 incubation. The following primary antibodies were used: anti-Ubiquityl-Histone H2A (Lys119) (clone D27C4) (rabbit, 1:1000, CST_8240), anti-Phospho-Histone H2A.X (Ser139) (rabbit, 1:400, CST_9718) known as γ-H2A.X and anti-SLC2A1 (GLUT1) (rabbit, 1:100, Sigma-Aldrich_ HPA031345). For secondary antibodies, Alexa Fluor-568-, 488-, or 647-conjugated secondary antibodies (Life Technologies) were used. Slides were mounted with ProLong Glass Antifade Mountant (Invitrogen).

7.2.4 Immunostaining of ex vivo cell cultures. Skin explants and exiting cells were fixed in 4% paraformaldehyde at RT for 10 min. Permeabilization and blocking were performed using the staining buffer (1%BSA, 5% Fetal Bovine Serum and 0.3% Triton X-100 in PBS) 1 h at RT. Primary antibodies were incubated overnight at 4 °C and secondary antibodies used at 1:1000 concentration 1 h at RT. DAPI nuclear staining was incubated in the dark for 5 min at RT. The following primary antibodies and dilutions were used: GM130 (clone 35) (mouse, 1:400, BD pharmingen). For secondary antibodies, Alexa Fluor-568-, 488-, or 647-conjugated secondary antibodies (Life Technologies) were used.

7.2.5 Images acquisition. Images were acquired with: Confocal: Leica TCS SP5 Tandem Scanner; Leica TCS SP8 Tandem Scanner; Stereoscope: Leica MZ16FA; Optical microscope: Olympus Bx41. Whole-mount and section staining were examined using a Leica TCS SP5/SP8 confocal microscopes equipped with 20x/40x or 60x immersion objectives (Zeiss). Z-stacks were acquired at 400 Hz with

an optimal stack distance and 1024×1024 dpi resolution. Z-stack projections were generated using the LAS AF software package (Leica Microsystems) as max intensity projections. For total wound bed images, the TCS SP5 resonance scanner was used. Four laser lines (405, 488, 561 and 633 nm) were used for near simultaneous excitation of DAPI or TOPRO3, Alexa448, tdTomato and Alexa647 fluorophores. H&E stainings were acquired using Olympus Bx41/ Leica DM6 microscope equipped with a 4x or 10x objective.

7.2.6 Image quantification using ImageJ. Digital images were processed and analysed using Fiji (https://imagej.nih.gov/ij/). Fluorophore intensity was measured as Integrated Density (IntD) in the selected ROI. The staining intensity (AU) was calculated as the ratio between the IntD of the antibody signal and the IntD of the DAPI or TOPRO3 signal in the same ROI. 3D surface plots of hair follicles were obtained using the Fiji function 3D surface plot. 5 hair follicle triples were overlapped for the analysis. Images are shown with the pseudo-colour Fire. For phalloidin staining segmentation, we used the MorphoLibJ plugin with the Morphological Segmentation function. The results were displayed as Catchment basins option.

7.3 In vitro and ex vivo assays

7.3.1 Isolation and *in vitro* culture of Lrig1 GL cells. Tail skin was dissected and incubated in trypsin EDTA (Thermo-Fisher, 0.25% in PBS) with the dermis side down overnight at 4 °C. The day after, the epidermis was peeled off from the dermis and chopped with 2 scalpels for 1 min. Isolated cells were plated over a feeder layer of mitomycin treated NIH/3T3 and cultured in keratinocytes media (low-calcium DMEM (Thermo-Fisher) supplemented with 10% FBS (Sigma-Aldrich), 100 U/ml penicillin-streptomycin (Thermo-Fisher), HCE cocktail consisting of hydrocortisone 0.5 µg/ml (Sigma-Aldrich), insulin 5 µg/ml (Thermo-Fisher), cholera enterotoxin 10^{-10} M (Sigma-Aldrich) and EGF 10 ng/ml (PeproTech) and cultured at 34 °C in a humidified atmosphere, with 8% CO_2.

For in vitro mini-bulk RNA-seq and ATAC-seq Sca-1^+ tdTomato$^+$ cells were sorted and cultured for 7 days at the indicated conditions. At day 7, cells were harvested, and tdTomato$^+$ were sorted to eliminate feeder cells and processed as indicated in mini-bulk RNA-seq and ATAC-seq paragraphs.

7.3.2 *In vitro* time lapse migration assay. For time lapse migration assay, isolated cells were plated in µ-Slide (Ibidi) with keratinocytes media. 24 h after plating dead cells were removed by PBS washes and attached cells were used for microscope acquisition. Plates were maintained in the incubator chamber of a confocal TCS SP5 microscope (Leica Microsystems) under controlled conditions (34 °C, 8% CO2). Images were collected in two different positions for each well and acquired every 15 minutes for 16 h. Cell displacement was tracked automatically using the TrackMate plugin in Fiji with LogDetector settings. Mean track displacement was calculated for each sample and plotted. For the normalised start position graph, we subtracted each point in the track with the coordinates of the starting point.

7.3.3 *Ex vivo* migration assay. The ex vivo migration assay was performed as previously described[24]. 2 mm punch biopsies were taken from freshly isolated tail skin. The skin was adhered to the bottom of a 24 well plate (Corning) and cultured in complete keratinocyte media under controlled conditions (34°C, 8% CO_2) for 4, 7, and 9 days, as indicated.

7.4 Flow cytometry

7.4.1 Fluorescence-activated cell sorting (FACS). To obtain single cell suspensions for FACS, roughly 5x5 mm of tail skin from 0w, 1w pw1, 2w pw1, 4w pw1, 8w pw1 and 1w pw2 were dissected and incubated in trypsin EDTA (Thermo-Fisher, 0.25% in PBS) with the dermis side down overnight at 4 °C. The day after, the epidermis was peeled off from the dermis with a scalpel and gently minced with 2 scalpels for 1 min. The resulting material was well resuspended with keratinocyte media and then filtered through a 70 µm cell strainer (VWR, Corning). The cell suspension was then centrifuged for 7 min at 4 °C 1500 rpm and washed twice with PBS. For single cell RNA-seq and mini-bulk RNA-seq, cells were resuspended in 500 µL of 1% BSA in PBS and 2 µL of SUPERase RNase Inhibitor (Thermo-Fisher, 20 U/µL) was added to each sample. td-Tomato positive cells were sorted with a 100 µm nozzle into 96 well PCR plates (Bio-Rad) containing the lysis buffer (0.5% Triton X-100 in H2O). For tdTomato$^+$ Glut1$^+$ (SLC2A1) and tdTomato$^+$ Sca-1$^+$ (Ly6a) cell sorting, cells were blocked with 3% FBS in PBS for 20 min and then incubated 30 min with 0.3 µg of anti-Glut1 antibody (clone EPR3915) (Alexa Fluor 647 conjugated, Abcam_ab195020) or 0.25 µg of anti-Sca-1 (clone E13-

161.7) (PE/Cyanine7 conjugated, Biolegend_122514) on ice. Antibody solution was removed, cells were washed three times with cold PBS and sorted in a new collection tube containing keratinocyte media with a 100 µm nozzle. To select viable cells TO-PRO-3 Iodide (Thermo-Fisher) was added at 1 µM concentration to the cell suspension before sorting. BD FACSAria II equipped with Diva software was used (BD Biosciences).

7.4.2 Glut1 quantification. Flow cytometry quantification of GLUT1 (SLC2A1) expression in Lrig1 GL tdTomato+ cells was performed on tail skin samples at different time points. Samples were processed as for sorting, with minor modifications. Briefly, after chopping, the cell suspensions were moved to a V bottom 96 well plate (Corning) for blocking and staining. 1 µg/mL DAPI was used to assess cell viability. GLUT1 antibody dilution and staining procedures were performed as described above and BD-FACSVerse (BD Bioscience) was used for acquisition. Single cell suspensions were first gated against DAPI to exclude dead cells, and then with forward and side scatters to isolate cells and singlets. Flow cytometry plots were generated using FlowJo™ (v10.8) after manual compensation.

7.4.3 Quantification of immune infiltrate. For immune infiltrate quantification, 6 mice were randomly paired together to obtain the 3 biological replicates. For time 0w, 5 mice were used. To obtain single cell suspensions from whole tail skin, roughly 5x5 mm of tail skin from 0w, 1w pw1, 8w pw1 and 1w pw2 were dissected from wound bed and distal memory areas (Distal) and processed as previously described in[72] with few modifications. Briefly, skin was chopped in ~ 1 mm^2 pieces and incubate o/n at 4 °C in a collagenase D-pronase mixture (Sigma-Aldrich). The day after, the samples were pipetted up and down for 5 min to disaggregate the tissue. The resulting material was well resuspended with media and then filtered through a 70 µm cell strainer (VWR, Corning). The cell suspensions were then centrifuged 7 min at 4 °C 1500 rpm, washed twice with PBS and blocked with 3% FBS in PBS for 20 min. The anti-mouse CD45 (VioGreen, Miltenyi Biotec_130-110- 803) antibody was incubated 10 min at RT at the concentration of 1,5 µg/ml. Single cells were gated according to their physical parameters.

7.5 Screening of epigenetic drugs

5 drugs targeting epigenetic factors have been selected on the basis of literature[73–77]. Briefly drugs were dissolved in acetone at the proper concentration and 50 µL of each drug was applied every other day for three times on 8w pw1 tail skin. 6 h after the last treatment Lrig1 GL mice were wounded as described above. 1 week after the second injury (1w pw2) samples were collected and the migration of Lrig1 GL cells towards the wound center was analysed. Drug list: A-196, SUV420H1 and SUV420H2 inhibitor (Sigma-Aldrich, 3 mg/mL), UNC0638, EHMT1/2 inhibitor (Sigma-Aldrich, 3 mg/mL), SB747651A, MSK1 inhibitor (Axon Medchem, 1.5 mg/mL), EX-527, Sirtuins inhibitor (Sigma-Aldrich, 3 mg/mL), PRT4165, Ring1a/1b inhibitor (PRC1) (Sigma-Aldrich, 3 mg/mL). To test the ability of PRT4165 to mimic memory the same approach reported above was used to treat 0w mice.

7.6 *In vivo* tumorigenesis

7.6.1 UV irradiation and tumorigenesis protocol. The UVB irradiation protocol was performed as previously described[78,79]. The UVB light source used was UVM-28EL (UVP Ultraviolet Product, Thermo-Fisher)**.** The irradiated energy was regularly measured with PCE-UV36 UVC radiation meter (PCE inst.). For acute UV irradiation, mice were treated with 200 mJ/cm2 for three times consecutively. The samples were collected 2 days after the last irradiation and analysed for epidermal thickness or hair follicle engagement. For *in vivo* tumorigenesis the DMBA-UVB two-stage-induced carcinogenesis protocol was used. Two days before the DMBA application, mice's back skin was shaved with an electric shaver. Mouse dorsal or tail skin was treated with 50 µL of 120 µg/mL of DMBA (Sigma-Aldrich) dissolved in acetone after the complete healing of wound or without wound as control. UVB irradiation (180mJ/cm2) was started 10 days after the DMBA application and continued for 3 times a week until the end of the experiments. All the mice were shaved once every 10 days. At the end points samples were collected, embedded in OCT or paraffin and analysed for histology. The tumours were classified as Squamous cell carcinoma (SCC) in situ or SCC according to the tumour architecture and the cytoplasmic morphology as previously described[78,79]. For tumorigenesis in SKH-1 hairless strain, mice were treated with 50µL of PRT4165 (3 mg/ml) (Sigma-

Aldrich) in acetone or with acetone alone every other day for 3 times, prior to UVB irradiation. All the mice were irradiated with 250 mJ/cm2, 3 times a week until the end point[80].

7.6.2 Tumour analysis. For quantification of tail eSCCs each tail was subdivided in 5 main regions (0 to 8mm from wound). The percentage of the scales that show eSCCs in each region were analysed (Fig.8a). For quantification of effraction of basement membrane zone as indication of tumour invasiveness (Extended Data Fig.13g, h), the length of deepest site of tumour from the normal adjacent basement membrane zone in H&E staining was evaluated by Fiji. As to grading SCC about differentiation, the ratio of well structure maintained epidermal layers and aberrant epidermal layers in H&E staining are calculated using Fiji.

7.7 Human squamous cell carcinoma samples (SCC)

Cutaneous SCC samples with AK (UV-SCC) regions were obtained from 9 patients. In addition, cutaneous SCC samples were collected from 3 Recessive Dystrophic Epidermolysis Bullosa (RDEB) (EB-SCC) (5 SCCs) and 4 psoriasis patients (Pso-SCC). The institutional review board of the Hokkaido University Graduate School of Medicine approved the study (ID: 13-043, 14-063, and 15-029). The study was carried out according to the Declaration of Helsinki Principles and the participants provided written informed consent. The RDEB patients harboured compound heterozygous mutations in COL7A1 (NM_000094.4) (patient 1: c.5443G>A (p.Gly1815Arg) and c.5819del (p.Pro1940Argfs*65), patient 2: c.5932C>T (p.Arg1978*) and c.8029G>A (p.Gly2677Ser), patient 3: c.7723G>A (p.Gly2575Arg) and c.8569G>T (p.Glu2857*)) and the expression of type VII collagen was reduced in their skin specimens[81,82].

7.8 Transcriptomics

7.8.1 Mini-bulk RNA-seq and analysis. The Mini-bulk RNA-seq of sorted epidermal cells has been performed on 150 cells. For mini-bulk RNA-seq at time point 0w, 1w pw1, 8w pw1, 1w pw2 the TdTomato$^+$ cells were isolated and sorted from a zone that comprise both wound bed and distal memory HFs. On the other hand, in vitro mini-bulk RNA-seq cells was performed on sorted (and cultured) TdTomato$^+$ Sca-1$^+$ isolated from distal memory region (Distal- 3 to 7 mm from wound bed)

or far control region (Ctrl- > 2 cm from injury). Briefly, after polyadenylated mRNA isolation, the Smart-Seq2 biotinylated Oligo(dT) was bound to Dynabeads MyOne Streptavidin T1 beads (Thermo-Fisher) and used to isolate mRNA from the cell lysate. Reverse transcription, amplification and library preparation were performed as for the single cell library preparation doubling the volumes.

After quality control (FastQCv0.11.2, https://www.bioinformatics.babraham.ac.uk/projects/fastqc), raw reads were processed with Trim Galore! v0.5.0 to perform quality and adapter trimming (parameters: --stringency 3 –q 20). Trimmed reads were next aligned to the mouse reference genome (UCSC mm10/GRCm38) using HiSat2 v2.2.01 with options -N 1 -L 20 -i S,1,0.5 -D 25 -R 5 --pen-noncansplice 20 --mp 1,0 --sp 3,0 and providing a list of known splice sites[83]. Gene expression levels were quantified with featureCounts v1.6.12 (options: -t exon -g gene_name) using the GENCODE (https://www.gencodegenes.org) release M20 annotation[84]. Gene expression counts of each cell population were next analysed using the edgeR3 R/Bioconductor package[85]. Lowly expressed/non-detected genes were filtered out (i.e.1 CPM in less than 3 samples) and normalization factors were calculated using the trimmed-mean of M-values (TMM) method. In order to account for unwanted sources of noise in the dataset, the normalized counts were processed using the SVA4 R/Bioconductor package[86]. The estimated surrogate variables were then included as covariates in the generalized linear model (GLM) used for differential expression testing (formula: ~time+sv1+…+svn). Following dispersion estimation, an ANOVA-like test was performed to identify the genes that were differentially expressed in any sample group across the time course, using 0w as the reference group in the model. Genes with |logFC|>1 in at least one time point and FDR<0.05 were considered as significantly differentially expressed. The same analyses were performed for each cell population. Memory gene list, defined as the gene with 1w pw1 |logFC| < 1w pw2 |logFC| are reported in Extended Data Table 1. GO analysis was performed using EnrichR tool (v 3.0) (https://maayanlab.cloud/Enrichr)[87].

7.8.2 scRNA-seq and analysis. For scRNA-seq at time point 0w, 1w pw1, 8w pw1, 1w pw2 the TdTomato^{+} cells were isolated and sorted from a zone that comprise both wound bed and distal memory HFs (Fig.3a-g, Fig.4b-e, and Extended Data Fig.5 and Extended Data Fig.7a-b). Concerning spatially resolved scRNA-seq at 8w pw1, the cells were instead isolated from wound bed (Wb), distal

memory (Distal- 3 to 7 mm from wound bed) or far control region (Ctrl- > 2 cm from injury) and sorted for TdTomato^{+} Sca-1^{+}, to enrich for the upper-HF memory cells (Fig.3i and Extended Data Fig.6a-j). Female mice only were used for this experiment. scRNA-seq was performed with a modified version of the Smart-Seq2 protocol[88] as in[89]. Briefly, individual cells are sorted into 96 well plates containing 2 µl of lysis buffer (0.5% Triton X-100 in H_2O), in presence of RNase inhibitor (Thermo-Fisher), dNTPs and Oligo(dT). Reverse transcription of the polyadenylated RNA has been performed with Maxima Rt Minus Reverse Transcriptase (Thermo-Fisher) and Template Switching Oligos. The resulting cDNA was amplified with 25 cycles of PCR and libraries will be prepared for sequencing with standard NexteraXT Illumina protocol (Illumina).

Reads were mapped to the *Mus musculus* transcriptome (ENSEMBL version 101) using Salmon v 0.13.1. Data processing: cells with less than 1000 genes expressed or with over 50 % of mitochondrial reads were filtered out, genes expressed in less than 5 cells were filtered out. Replicates were normalized using Seurat[90] and corrected for batch effects using Cluster Similarity Spectrum, Harmony or FastMNN. Optimal clustering was selected based on cumulative gene expression patterns of marker genes. RNA-seq data were analysed using Seurat packages (v 4.0.1) on R (v 4.0.3). Only protein-coding genes were considered for downstream analysis and read counts selected were batch corrected with the CSS method. All Seurat analyses were performed using default parameters. The specific changes are reported when present. Dimensionality reduction (PCA + UMAP) were calculated with Seurat functions RunPCA (npcs = 100) and RunUMAP (reduction = "css", dims = 1:8), using the top 10000 variable genes. Cell clustering was performed with function FindNeighbors (reduction = "css", dims = 1:8) and FindClusters (resolution = 2.1).
Cluster marker genes were identified by FindAllMarkers (only.pos = T, return.thresh = 0.05) function looking for upregulated genes in each cluster against the remaining cells and the top 50 by the "avg_logFC" rank was selected. Marker genes for each cluster are shown in Extended Data Table 2.

7.8.3 Differential expression analysis and feature extraction. The analysis of differentially expressed genes within the same cluster was performed using Seurat's FindMarkers() function. To plot the expression of genes or gene groups the FeaturePlot() function.

7.8.4 Seurat integration. Single cell data from Lgr5 GL cells, Lrig1 GL cells aged homeostasis or Lrig1 GL cells treated with vehicle or PRT4165 were projected onto the reference UMAP structure derived from Lrig1 GL young data, in order to localize the position of each cell in the hair follicle or interfollicular epidermis. The overlap was performed using SeuratIntegration Tools[91] with FindTransferAnchors and MapQuery functions.

7.8.5 Pseudotime analysis. Pseudotime analysis was carried out using Slingshot package (v. 1.8.0)[92] on the Seurat object, using the top 10000 variable genes. For the pseudotime A, B, C, D, E cluster 11 corresponding to junctional zone stem cells on the basis of the molecular markers, was selected as the starting point. Pseudotime F was instead found selecting cluster 5 (bulge) as starting position. To derive the differentially expressed genes (DEG) the TestPseudotime function was used with a threshold of FDR < 0.05. The genes were z-scored (and smoothed) and uploaded on Morpheus (https://software.broadinstitute.org/morpheus) to obtain the heatmaps. For pseudotime D specifically a deep analysis was performed. 0w and 1w pw1 cells were separated from 8w pw1 and 1w pw2 cells and ordered on pseudotime. Morpheus clustering was then performed (hierarchical clustering, row, complete) on 0w - 1w pw1 cells to compare the expression and the trend of the same genes in the two conditions.

7.8.6 GO enrichment analysis. Gene Ontology (GO) enrichment analysis was performed using EnrichR tool (v 3.0)[87] using GO Biological Process. Results were used to generate "DotHeatmap" to compare enrichment between different conditions and pseudotimes.

7.8.7 GSEA analysis. GSEA Analysis were performed using the GSEA function by ClusterProfiler package (v 3.18.1)[93] and using as Database reference: MSigDB (all categories of DB), GO (Biological Process, Molecular Function and Cell Component) and KEGG. DEG genes obtained from 0w vs 8w pw1 and 1w pw1 vs 1w pw2 comparisons were used as input.

7.9 ATAC-seq and analysis

Epidermal cells were isolated as described above. For 0w, 1w pw1, 8w pw1 and 1w pw2 cells were isolated specifically from distal memory region (Distal), from 3 to 7 mm from wound bed. For in vitro ATAC-seq cells from the far away control region (Ctrl- more than 2 cm away from wound bed) and from the distal memory zone (Distal- 3 to 7 mm from wound bed) were collected and cultured. ATAC-seq relative to pre-tumour lesions was performed on cells from the TS (tumour stimuli) treated distal memory zone (Distal- 3 to 7 mm from wound bed) or an unwounded TS treated epidermis (Ctrl) used as control. To enrich the upper-HF cells, Lrig1-GL TdTomato^{+} Sca-1^{+} cells were sorted as described above. ATAC-seq was performed as previously described in[94]. For each sample, epidermis was pooled from 2 mice. Briefly, 20-50,000 sorted cells were lysed in ATAC lysis buffer for 5 minutes and then transposed with TN5 transposase for 30 minutes at 37 °C. NexteraXT indexes (Illumina) were added with 12 cycles of PCR and samples were sequenced paired-end on a NextSeq 1000 System (Illumina).

Sequenced reads were processed with the ENCODE ATAC-seq pipeline (v1.9.0, https://github.com/ENCODE-DCC/ATAC-seq-pipeline) using the default parameters. Bowtie2[95] was used to align reads to the mouse reference genome UCSC mm10. After the discard of duplicated, multi-mapping and poor-quality alignments, the peak calling was performed with MAC2[96] generating the signal tracks as fold enrichment control.

Differentially opened regions between treatment and its control samples were identified using DiffBind v3.0.3[97] with parameters: normalize = DBA_NORM_NATIVE, library = DBA_LIBSIZE_DEFAULT, background = BKGR_TRUE, AnalysisMehod = EDGER. Peaks with Pvalue < 0.05 and |logFC| > 0.5 were considered differentially open. Target gene annotation of each ATAC peak was obtained with GREAT[98] using the Basal plus extension association rules and the whole mouse genome as background.

The enrichments of selected gene lists were performed by using Fisher's exact test in the BioConductor R package GeneOverlap (http://shenlab-sinai.github.io/shenlab-sinai/).

7.10 Quantification and statistical analysis

Statistical analysis was performed by using the GraphPad Prism 7 software (GraphPad Inc., San Diego, CA, USA). Data are presented as mean ± standard error or mean ± standard deviation. Statistical significance for all wound healing studies was determined with the two-tailed unpaired Student's t-test with a 95% confidence interval under the untested assumption of normality. Statistical significance tumour incidence was calculated using either a Mann-Whitney test or random permutation. No statistical method was applied to predetermine sample size and mice were assigned at random to groups. Images are representative of at least three independent experiments and mice from both sexes were used, if not differently indicated.

7.11 Data availability

scRNA-seq, mini bulk RNA-seq and ATAC-seq data that support the findings of this study have been deposited in the Gene Expression Omnibus (GEO) under accession code GSE197590.

CHAPTER 8

Bibliography

1. Kolarsick, P. A., Ann Kolarsick, M. & Goodwin, C. Anatomy and Physiology of the Skin. (2006).
2. Fuchs, E. & Raghavan, S. Getting under the skin of epidermal morphogenesis. *Nature Reviews Genetics 2002 3:3* **3**, 199–209 (2002).
3. James, W. D. (William D., Berger, T. G., Elston, D. M. & Odom, R. B. Andrews' diseases of the skin : clinical dermatology. 961 (2006).
4. Gonzales, K. A. U. & Fuchs, E. Skin and Its Regenerative Powers: An Alliance between Stem Cells and Their Niche. *Dev Cell* **43**, 387–401 (2017).
5. Legué, E. & Nicolas, J. F. Hair follicle renewal: organization of stem cells in the matrix and the role of stereotyped lineages and behaviors. *Development* **132**, 4143–4154 (2005).
6. Schepeler, T., Page, M. E. & Jensen, K. B. Heterogeneity and plasticity of epidermal stem cells. *Development* **141**, 2559–2567 (2014).
7. Baker, R. E. & Murray, P. J. Understanding hair follicle cycling: a systems approach. *Curr Opin Genet Dev* **22**, 607–612 (2012).
8. Donati, G. & Watt, F. M. Stem cell heterogeneity and plasticity in epithelia. *Cell Stem Cell* **16**, 465–476 (2015).
9. Alcolea, M. P. & Jones, P. H. Lineage Analysis of Epidermal Stem Cells. *Cold Spring Harb Perspect Med* **4**, (2014).
10. Rognoni, E. & Watt, F. M. Skin Cell Heterogeneity in Development, Wound Healing, and Cancer. *Trends Cell Biol* **28**, 709–722 (2018).
11. Jaks, V. *et al.* Lgr5 marks cycling, yet long-lived, hair follicle stem cells. *NATURE GENETICS VOLUME* **40**, (2008).
12. Jensen, U. B. *et al.* A distinct population of clonogenic and multipotent murine follicular keratinocytes residing in the upper isthmus. *J Cell Sci* **121**, 609 (2008).

13. Page, M. E., Lombard, P., Ng, F., Göttgens, B. & Jensen, K. B. The Epidermis Comprises Autonomous Compartments Maintained by Distinct Stem Cell Populations. *Cell Stem Cell* **13**, 471 (2013).

14. Donati, G. *et al.* Wounding induces dedifferentiation of epidermal Gata6 + cells and acquisition of stem cell properties. *Nat Cell Biol* **19**, 603–613 (2017).

15. Mascré, G. *et al.* Distinct contribution of stem and progenitor cells to epidermal maintenance. (2012) doi:10.1038/nature11393.

16. Dekoninck, S. & Blanpain, C. Stem cell dynamics, migration and plasticity during wound healing. *Nat Cell Biol* **21**, 18–24 (2019).

17. Mitoyan, L. *et al.* A stem cell population at the anorectal junction maintains homeostasis and participates in tissue regeneration. *Nat Commun* **12**, (2021).

18. Nasser, W. *et al.* Corneal-Committed Cells Restore the Stem Cell Pool and Tissue Boundary following Injury. *Cell Rep* **22**, 323–331 (2018).

19. Blanpain, C. & Fuchs, E. Stem cell plasticity. Plasticity of epithelial stem cells in tissue regeneration. *Science* **344**, (2014).

20. Ito, M. *et al.* Stem cells in the hair follicle bulge contribute to wound repair but not to homeostasis of the epidermis. *Nat Med* **11**, 1351–1354 (2005).

21. Wabik, A. & Jones, P. H. Switching roles: the functional plasticity of adult tissue stem cells. *EMBO J* **34**, 1164 (2015).

22. Divangahi, M. *et al.* Trained immunity, tolerance, priming and differentiation: distinct immunological processes. *Nat Immunol* **22**, 2–6 (2021).

23. Larsen, S. B. *et al.* Establishment, maintenance, and recall of inflammatory memory. *Cell Stem Cell* **28**, 1758-1774.e8 (2021).

24. Naik, S. *et al.* Inflammatory memory sensitizes skin epithelial stem cells to tissue damage. *Nature* **550**, 475–480 (2017).

25. Gonzales, K. A. U. *et al.* Stem cells expand potency and alter tissue fitness by accumulating diverse epigenetic memories. *Science* **374**, (2021).

26. Levra Levron, C. & Donati, G. Multiplicity of stem cell memories of inflammation and tissue repair in epithelia. *Trends Cell Biol* (2023) doi:10.1016/J.TCB.2023.10.008.

27. Niec, R. E., Rudensky, A. Y. & Fuchs, E. Inflammatory adaptation in barrier tissues. *Cell* **184**, 3361–3375 (2021).

28. Netea, M. G. *et al.* Defining trained immunity and its role in health and disease. *Nature Reviews Immunology 2020 20:6* **20**, 375–388 (2020).

29. Halper-Stromberg, A. & Jabri, B. Maladaptive consequences of inflammatory events shape individual immune identity. *Nat Immunol* **23**, 1675–1686 (2022).

30. Latil, M. *et al.* Cell-Type-Specific Chromatin States Differentially Prime Squamous Cell Carcinoma Tumor-Initiating Cells for Epithelial to Mesenchymal Transition. *Cell Stem Cell* **20**, 191-204.e5 (2017).

31. Lochhead, P. *et al.* Etiologic field effect: reappraisal of the field effect concept in cancer predisposition and progression. *Modern Pathology 2015 28:1* **28**, 14–29 (2014).

32. Solé-Boldo, L. *et al.* Differentiation-related epigenomic changes define clinically distinct keratinocyte cancer subclasses. *Mol Syst Biol* **18**, (2022).

33. Curtius, K., Wright, N. A. & Graham, T. A. An evolutionary perspective on field cancerization. *Nature Reviews Cancer 2017 18:1* **18**, 19–32 (2017).

34. Slaughter, D. P., Southwick, H. W. & Smejkal, W. Field cancerization in oral stratified squamous epithelium; clinical implications of multicentric origin - PubMed. *Clinical implications of multicentric origin. Cancer 6* 963–968 (1953).

35. Alcolea, M. P. *et al.* Differentiation imbalance in single oesophageal progenitor cells causes clonal immortalization and field change. *Nature Cell Biology 2014 16:6* **16**, 612–619 (2014).

36. Sinjab, A., Han, G., Wang, L. & Kadara, H. Field carcinogenesis in cancer evolution: what the cell is going on? *Cancer Res* **80**, 4888 (2020).

37. Nishiyama, N. *et al.* Genome-wide DNA methylation profiles in urothelial carcinomas and urothelia at the precancerous stage. *Cancer Sci* **101**, 231–240 (2010).

38. Baba, Y. *et al.* Epigenetic field cancerization in gastrointestinal cancers. *Cancer Lett* **375**, 360–366 (2016).

39. Park, S. *et al.* Tissue-scale coordination of cellular behaviour promotes epidermal wound repair in live mice. *Nat Cell Biol* **19**, 155–163 (2017).

40. Chen, C. C. *et al.* Organ-level quorum sensing directs regeneration in hair stem cell populations. *Cell* **161**, 277–290 (2015).

41. Aragona, M. *et al.* Defining stem cell dynamics and migration during wound healing in mouse skin epidermis. *Nat Commun* **8**, (2017).

42. Sepich, D. S. & Solnica-Krezel, L. Intracellular Golgi Complex organization reveals tissue specific polarity during zebrafish embryogenesis. *Developmental Dynamics* **245**, 678–691 (2016).

43. Joost, S. *et al.* Single-Cell Transcriptomics Reveals that Differentiation and Spatial Signatures Shape Epidermal and Hair Follicle Heterogeneity. *Cell Syst* **3**, 221-237.e9 (2016).

44. Dekoninck, S. *et al.* Defining the Design Principles of Skin Epidermis Postnatal Growth. *Cell* **181**, 604-620.e22 (2020).

45. Gomez, C. *et al.* The interfollicular epidermis of adult mouse tail comprises two distinct cell lineages that are differentially regulated by Wnt, Edaradd, and Lrig1. *Stem Cell Reports* **1**, 19–27 (2013).

46. Depianto, D. & Coulombe, P. A. Intermediate filaments and tissue repair. *Exp Cell Res* **301**, 68–76 (2004).

47. Choi, J. E. *et al.* A unique subset of glycolytic tumour-propagating cells drives squamous cell carcinoma. *Nat Metab* **3**, 182–195 (2021).

48. Cohen, I. *et al.* PRC1 Fine-tunes Gene Repression and Activation to Safeguard Skin Development and Stem Cell Specification. *Cell Stem Cell* **22**, 726-739.e7 (2018).

49. Endoh, M. *et al.* Histone H2A mono-ubiquitination is a crucial step to mediate PRC1-dependent repression of developmental genes to maintain ES cell identity. *PLoS Genet* **8**, (2012).

50. Ismail, I. H., McDonald, D., Strickfaden, H., Xu, Z. & Hendzel, M. J. A Small Molecule Inhibitor of Polycomb Repressive Complex 1 Inhibits Ubiquitin Signaling at DNA Double-strand Breaks. *J Biol Chem* **288**, 26944 (2013).

51. Pivetti, S. *et al.* Loss of PRC1 activity in different stem cell compartments activates a common transcriptional program with cell type-dependent outcomes. *Sci Adv* **5**, (2019).

52. MacCarthy-Morrogh, L. & Martin, P. The hallmarks of cancer are also the hallmarks of wound healing. *Sci Signal* **13**, (2020).

53. Falvo, D. J. *et al.* A lineage-specific epigenetic memory of inflammation potentiates Kras-driven pancreatic tumorigenesis. *bioRxiv* 2021.11.01.466807 (2021) doi:10.1101/2021.11.01.466807.

54. Poggetto, E. Del *et al.* Epithelial memory of inflammation limits tissue damage while promoting pancreatic tumorigenesis. *Science* **373**, (2021).

55. Nehal, K. S. & Bichakjian, C. K. Update on Keratinocyte Carcinomas. *N Engl J Med* **379**, 363–374 (2018).

56. Abel, E. L., Angel, J. M., Kiguchi, K. & DiGiovanni, J. Multi-stage chemical carcinogenesis in mouse skin: fundamentals and applications. *Nat Protoc* **4**, 1350–1362 (2009).

57. Röwert-Huber, J. *et al.* Actinic keratosis is an early in situ squamous cell carcinoma: a proposal for reclassification. *Br J Dermatol* **156 Suppl 3**, 8–12 (2007).

58. Fernandez-Capetillo, O. *et al.* DNA damage-induced G2–M checkpoint activation by histone H2AX and 53BP1. *Nature Cell Biology 2002 4:12* **4**, 993–997 (2002).

59. Huang, P. Y. & Balmain, A. Modeling cutaneous squamous carcinoma development in the mouse. *Cold Spring Harb Perspect Med* **4**, (2014).

60. Trafford, A. M., Parisi, R., Kontopantelis, E., Griffiths, C. E. M. & Ashcroft, D. M. Association of Psoriasis With the Risk of Developing or Dying of Cancer: A Systematic Review and Meta-analysis. *JAMA Dermatol* **155**, 1390–1403 (2019).

61. Watanabe, M., Natsuga, K., Shinkuma, S. & Shimizu, H. Epidermal aspects of type VII collagen: Implications for dystrophic epidermolysis bullosa and epidermolysis bullosa acquisita. *J Dermatol* **45**, 515–521 (2018).

62. Netea, M. G. *et al.* Defining trained immunity and its role in health and disease. *Nat Rev Immunol* **20**, 375–388 (2020).

63. Niec, R. E., Rudensky, A. Y. & Fuchs, E. Inflammatory adaptation in barrier tissues. *Cell* **184**, 3361–3375 (2021).

64. Naik, S. & Fuchs, E. Inflammatory memory and tissue adaptation in sickness and in health. *Nature* **607**, 249–255 (2022).

65. Levra Levron, C. *et al.* Tissue memory relies on stem cell priming in distal undamaged areas. *Nature Cell Biology 2023 25:5* **25**, 740–753 (2023).

66. Konieczny, P. *et al.* Interleukin-17 governs hypoxic adaptation of injured epithelium. *Science (1979)* (2022) doi:10.1126/SCIENCE.ABG9302.

67. Cheng, S. C. *et al.* mTOR- and HIF-1α-mediated aerobic glycolysis as metabolic basis for trained immunity. *Science* **345**, (2014).

68. Lim, A. I. *et al.* Prenatal maternal infection promotes tissue-specific immunity and inflammation in offspring. *Science* **373**, (2021).

69. Avgustinova, A. *et al.* Loss of G9a preserves mutation patterns but increases chromatin accessibility, genomic instability and aggressiveness in skin tumours. *Nat Cell Biol* **12**, 1400–1409 (2018).

70. Bakhoum, M. F. *et al.* Loss of polycomb repressive complex 1 activity and chromosomal instability drive uveal melanoma progression. *Nat Commun* **12**, (2021).

71. Madisen, L. *et al.* A robust and high-throughput Cre reporting and characterization system for the whole mouse brain. *Nat Neurosci* (2010) doi:10.1038/nn.2467.

72. Khan, M. & Gasser, S. Generating Primary Fibroblast Cultures from Mouse Ear and Tail Tissues. *J Vis Exp* **2016**, 53565 (2016).

73. Yokoyama, Y. *et al.* Loss of histone H4K20 trimethylation predicts poor prognosis in breast cancer and is associated with invasive activity. *Breast Cancer Res* **16**, (2014).

74. Cohen, I. *et al.* PRC1 preserves epidermal tissue integrity independently of PRC2. *Genes Dev* **33**, 55–60 (2019).

75. Huang, X. *et al.* Resveratrol Promotes Diabetic Wound Healing via SIRT1-FOXO1-c-Myc Signaling Pathway-Mediated Angiogenesis. *Front Pharmacol* **10**, (2019).

76. Knudsen, A. M., Boldt, H. B., Jakobsen, E. V. & Kristensen, B. W. The multi-target small-molecule inhibitor SB747651A shows in vitro and in vivo anticancer efficacy in glioblastomas. *Sci Rep* **11**, (2021).

77. Liu, X.-R. *et al.* UNC0638, a G9a inhibitor, suppresses epithelial-mesenchymal transition-mediated cellular migration and invasion in triple negative breast cancer. *Mol Med Rep* **17**, 2239 (2018).

78. Ando, S. *et al.* Bone marrow-derived cells are not the origin of the cancer stem cells in ultraviolet-induced skin cancer. *American Journal of Pathology* **174**, 595–601 (2009).

79. Yanagi, T. *et al.* Loss of dynamin-related protein 1 (Drp1) does not affect epidermal development or UVB-induced apoptosis but does accelerate UVB-induced carcinogenesis. *J Dermatol Sci* **99**, 109–118 (2020).

80. Melnikova, V. O., Pacifico, A., Chimenti, S., Peris, K. & Ananthaswamy, H. N. Fate of UVB-induced p53 mutations in SKH-hr1 mouse skin after discontinuation of irradiation: relationship to skin cancer development. *Oncogene* **24**, 7055–7063 (2005).

81. Matsumura, W. *et al.* Cultured Epidermal Autografts from Clinically Revertant Skin as a Potential Wound Treatment for Recessive Dystrophic Epidermolysis Bullosa. *J Invest Dermatol* **139**, 2115-2124.e11 (2019).

82. Natsuga, K. *et al.* Response of intractable skin ulcers in recessive dystrophic epidermolysis bullosa patients to an allogeneic cultured dermal substitute. *Acta Derm Venereol* **90**, 165–169 (2010).

83. Kim, D., Paggi, J. M., Park, C., Bennett, C. & Salzberg, S. L. Graph-based genome alignment and genotyping with HISAT2 and HISAT-genotype. *Nat Biotechnol* **37**, 907–915 (2019).

84. Liao, Y., Smyth, G. K. & Shi, W. featureCounts: an efficient general purpose program for assigning sequence reads to genomic features. *Bioinformatics* **30**, 923–930 (2014).

85. Robinson, M. D., Mccarthy, D. J. & Smyth, G. K. edgeR: a Bioconductor package for differential expression analysis of digital gene expression data. *BIOINFORMATICS APPLICATIONS NOTE* **26**, 139–140 (2010).

86. Leek, J. T. svaseq: removing batch effects and other unwanted noise from sequencing data. *Nucleic Acids Res* **42**, 161 (2014).

87. Chen, E. Y. *et al.* Enrichr: Interactive and collaborative HTML5 gene list enrichment analysis tool. *BMC Bioinformatics* **14**, 1–14 (2013).

88. Picelli, S. *et al.* Full-length RNA-seq from single cells using Smart-seq2. *Nature Protocols 2013 9:1* **9**, 171–181 (2014).

89. Proserpio, V., Duval, C., Falvo, V., Donati, G. & Oliviero, S. Single-Cell Sequencing for Everybody. *Methods Mol Biol* **2421**, 217–229 (2022).

90. Hao, Y. *et al.* Integrated analysis of multimodal single-cell data. *Cell* **184**, 3573-3587.e29 (2021).

91. Stuart, T. *et al.* Comprehensive Integration of Single-Cell Data. *Cell* **177**, 1888-1902.e21 (2019).

92. Street, K. *et al.* Slingshot: Cell lineage and pseudotime inference for single-cell transcriptomics. *BMC Genomics* **19**, 1–16 (2018).

93. Yu, G., Wang, L. G., Han, Y. & He, Q. Y. ClusterProfiler: An R package for comparing biological themes among gene clusters. *OMICS* **16**, 284–287 (2012).

94. Buenrostro, J., Wu, B., Chang, H. & Greenleaf, W. ATAC-seq: A Method for Assaying Chromatin Accessibility Genome-Wide. doi:10.1002/0471142727.mb2129s109.

95. Langmead, B. & Salzberg, S. L. Fast gapped-read alignment with Bowtie 2. *Nature Methods 2012 9:4* **9**, 357–359 (2012).

96. Zhang, Y. *et al.* Model-based analysis of ChIP-Seq (MACS). *Genome Biol* **9**, 1–9 (2008).

97. Wu, D. Y., Bittencourt, D., Stallcup, M. R. & Siegmund, K. D. Identifying differential transcription factor binding in ChIP-seq. *Front Genet* **6**, 169 (2015).

98. McLean, C. Y. *et al.* GREAT improves functional interpretation of cis-regulatory regions. *Nature Biotechnology 2010 28:5* **28**, 495–501 (2010).

Publications

1. **Levra Levron C***, Watanabe M*, Proserpio V*, Piacenti G, Lauria A, Kaltenbach S, Nohara T, Tamburrini A, Anselmi F, Duval C, Elettrico L, Conti L, Donna D, Baev D, Natsuga K, Hagai T, Oliviero S, Donati G, *Tissue memory relies on stem cell priming in distal undamaged areas.* **Nat Cell Biol** (2023). doi: 10.1038/s41556-023-01120-0.

2. **Levra Levron C**, Donati G, *Multiplicity of stem cell memories of inflammation and tissue repair in epithelia*, **Trends in Cell Biology** (2023). doi: 10.1016/j.tcb.2023.10.008.

3. Jacob T, Annusver K, Czarnewski P, Dalessandri T, Kastriti ME, **Levra Levron C**, Mikkola ML, Rendl M, Lichtenberger BM, Donati G, Björklund A, Kasper M, *Molecular and spatial landmarks of early mouse skin development*, **Developmental Cell** (2023). doi: 10.1016/j.devcel.2023.07.015

4. Lauria A, Meng G, Proserpio V, Rapelli S, Maldotti M, Polignano IL, Anselmi F, Incarnato D, Krepelova A, Donna D, **Levra Levron C**, Donati G, Molineris I, Neri F, Oliviero S. *DNMT3B supports meso-endoderm differentiation from mouse embryonic stem cells*. **Nat Commun**. (2023). doi: 10.1038/s41467-023-35938-x.

5. Pergolizzi B, Panuzzo C, Ali MS, Lo Iacono M, **Levra Levron C**, Ponzone L, Prelli M, Cilloni D, Calautti E, Bozzaro S, Bracco E. *Two conserved glycine residues in mammalian and Dictyostelium Rictor are required for mTORC2 activity and integrity*. **J Cell Sci** (2019). doi: 10.1242/jcs.236505. PMID: 31653780.